UNDERSTANDING HARD INTERACTION IN QCD AND THE SEARCH FOR THE GLUON SPIN CONTRIBUTION TO THE SPIN OF THE PROTON

A Dissertation Presented

by

AMARESH DATTA

Submitted to the Graduate School of the
University of Massachusetts Amherst in partial fulfillment
of the requirements for the degree of

DOCTOR OF PHILOSOPHY

May, 2012

Physics

UNDERSTANDING HARD INTERACTION IN QCD AND THE SEARCH FOR THE GLUON SPIN CONTRIBUTION TO THE SPIN OF THE PROTON

A Dissertation Presented

by

AMARESH DATTA

Approved as to style and content by:

David Kawall, Chair

John Donoghue, Member

Krishna Kumar, Member

Grant Wilson, Member

Donald Candela, Department Chair
Physics

To my grandfather, Late Anantalal Datta, the poor refugee from a broken country, who taught the value of education to his children.

ACKNOWLEDGMENTS

I would like to acknowledge here my advisor David Kawall for all the help and the support from him during the years I worked with him. His unwavering encouragements has been a beacon throughout the good and the bad times. Thank you Dave.

My very special thanks to Christine Aidala for the enormous amount of time and effort she spent discussing physics (and other things) with me and for her guiding hand that helped me finish the analyses through a lot of complications. Thank you Christine.

Jane Knapp, the angel of a graduate secretary in the Physics Department at UMass, Amherst, deserves the gratitude of generations of graduate students in the for the loving smile and the care with which she resolves the regular and the more complicated official issues for us. Thank you Jane.

ABSTRACT

UNDERSTANDING HARD INTERACTION IN QCD AND THE SEARCH FOR THE GLUON SPIN CONTRIBUTION TO THE SPIN OF THE PROTON

MAY, 2012

AMARESH DATTA

B.Sc., JADAVPUR UNIVERSITY

M.Sc., INDIAN INSTITUTE OF TECHNOLOGY, MUMBAI

Ph.D., UNIVERSITY OF MASSACHUSETTS AMHERST

Directed by: Professor David Kawall

In the following discourse unpolarized cross sections and double helicity asymmetries of single inclusive positive and negative charged hadrons at mid-rapidity from $p+p$ collisions at $\sqrt{s} = 62.4$ GeV are presented. Measurements for the transverse momentum range $1.0 < p_T < 4.5$ GeV/c are done with PHENIX detector at Relativistic Heavy-Ion Collider (RHIC) and are consistent with calculations based on perturbative quantum chromodynamics (pQCD) at next-to-leading order (NLO) in the strong coupling constant, α_s. Resummed pQCD calculations including terms with next-to-leading log (NLL) accuracy, yielding reduced theoretical uncertainties, also agree with the data. The double helicity asymmetry, sensitive at leading order to the gluon polarization in a momentum fraction range of $0.05 \lesssim x_{gluon} \lesssim 0.2$, is consistent with recent global parameterizations disfavoring large gluon polarization.

TABLE OF CONTENTS

LIST OF TABLES

Table **Page**

LIST OF FIGURES

Figure **Page**

CHAPTER 1

INTRODUCTION

The proton, which is a universal building block of all atoms, was named after the Greek word for 'first'. It was thought to be a fundamental particle in the early parts of the twentieth century. In 1933, measurements by Esterman, Frisch and Stern [69, 67] showed that the proton had a large anomalous magnetic moment $\sim 2.79\,\mu_N$, giving the first indications that protons are not fundamental point-like particles and that they might be composite particles. Physicists have since worked towards understanding the structure of the proton and we have come a long way [45] in the decades that followed. Although our knowledge of the nucleon structure today is considerable, it is still incomplete, in particular with regard to its spin structure, as we'll see in the following sections. With the measurements of cross sections and double helicity asymmetries of mid-rapidity production of inclusive charged hadrons in p+p collisions at $\sqrt{s} = 62.4$ GeV, we aim to get insights into QCD, the fundamental theory of strong force as a description of hard scattering processes, as well as the spin structure of the proton.

1.1 Proton Structure

1.1.1 Elastic Structure and Form Factors

Scattering experiments are performed to probe the structure of a particle. The more energetic the scattered particles are, the smaller is the length scale probed by them (according to de Broglie, length scale $\lambda \sim 1/p$ where p is the momentum). Scattering of the alpha particles (He nuclei) through thin (thickness $\sim$ micron) gold

foil by Ernest Rutherford in 1911 proved the substructure of atoms and the presence of the much smaller nuclei inside atoms. A few years later passage of the energetic alpha particles through hydrogen gas produced hydrogen nuclei and with the considerations of atomic weights, it was conjectured to be a common building block for all atoms (nuclei). Rutherford named it as the 'proton'.

Electrons (and muons) have been used over the decades for probing the structure of the proton through scattering experiments. In the non-relativistic limit, neglecting the proton recoil and summing over all possible helicity states of the scattered electrons, the results from the scattering experiments can be described by the Rutherford scattering cross section :

$$\left(\frac{d\sigma}{d\Omega}\right)_{Rutherford} = \frac{\alpha^2 m_e^2}{4p^4 \sin^4 \frac{\theta}{2}}, \tag{1.1}$$

where α is the fine structure constant, p is the momentum of the electron, m_e is the electron mass and θ is the scattering angle. It can be concluded that when the length scales probed are much larger than the proton charge radius, the protons behave as charged point particles. Considering relativistic scattered particles ($p \gg m_e$ and conserving the helicity state), $e+p$ scattering can be described by the Mott scattering cross section (still neglecting the proton recoil) :

$$\left(\frac{d\sigma}{d\Omega}\right)_{Mott} = \frac{\alpha^2}{4p^4 \sin^4 \frac{\theta}{2}} \left[m_e^2 + p^2 \cos^2 \frac{\theta}{2}\right], \tag{1.2}$$

where the $\cos^2 \frac{\theta}{2}$ term arises from averaging over the electron spins. Deviations of experimentally measured cross sections from the Mott scattering formula describes the charge distribution of the proton (Fig. 1.1). The deviations are expressed in terms of the form factor which is given by the Fourier transform of the charge distributions inside the proton $F(\vec{q}^2) = \int \rho(\vec{r}) e^{i\vec{q}\cdot\vec{r}} d^3\vec{r}$:

$$\frac{d\sigma}{d\Omega} = \left(\frac{d\sigma}{d\Omega}\right)_{Mott} \times F(\vec{q}^2), \tag{1.3}$$

where $\vec{q}$ is the momentum transfer to the proton. At higher energies the scattered electrons start probing the charge density of the proton. Considering the most general case of the relativistic scattering of electrons from protons, including the recoil of the target proton and the charge and the magnetic moment distributions inside the proton, the Rosenbluth formula for the elastic electron-proton scattering [89] gives :

$$\frac{d\sigma}{d\Omega} = \frac{\alpha^2}{4E^2 \sin^4 \frac{\theta}{2}} \frac{E'}{E} \left(\frac{G_E^2(q^2) + \tau G_M^2(q^2)}{1+\tau} \cos^2 \frac{\theta}{2} + 2\tau G_M^2 \sin^2 \frac{\theta}{2} \right) \tag{1.4}$$

where $\tau = -q^2/4M$ with q being the four-momentum transfer and M is the mass of the proton, E and E' are the incident and scattered electron energies (takes into account the proton recoil) and $G_E(q^2)$ and $G_M(q^2)$ are respectively the electric and magnetic form factors. The $\sin^2 \frac{\theta}{2}$ term arises due to spin-spin interaction between the electron and the proton. In the low energy limit $\tau \ll 1$, the form factors can be interpreted as :

$$G_E(q^2) \approx G_E(\vec{q}^2) = \int \rho(\vec{r}) e^{i\vec{q}\cdot\vec{r}} d^3\vec{r}, \tag{1.5}$$

$$G_M(q^2) \approx G_M(\vec{q}^2) = \int \mu(\vec{r}) e^{i\vec{q}\cdot\vec{r}} d^3\vec{r}. \tag{1.6}$$

The q^2-dependence of the form factors are given by :

$$G_E(q^2) = \frac{G_M(q^2)}{\mu_p} = \left(1 - \frac{q^2}{a^2}\right)^{-2}, \tag{1.7}$$

where $\mu_p = G_M(0)$ is the magnetic moment of the proton and $a^2 = 0.71$ GeV^2 is determined experimentally [97]. The electric form factor in the limit of low energy gives $G_E(0) = 1$, indicating the point-like behavior of proton. The charge distribution

of the proton is described by spherically symmetric exponential function of the radius $\rho(r) = \rho_0 e^{-r/r_0}$ with an rms radius of 0.87 fm [98]. Magnetic moment of the proton is measured to be 2.79 μ_N, where nuclear magneton is given by $\mu_N = e/2M$. Proton elastic form factors are probed by measuring either scattered electrons [54] or recoiling protons [88] from $e + p$ elastic scaterring experiments. The recent high precision measurements of the ratio of proton elastic form factors $\mu_p G_E/G_M$ have indicated that with increasing q^2, electric form factor G_E falls faster than magnetic form factor G_M of proton [87].

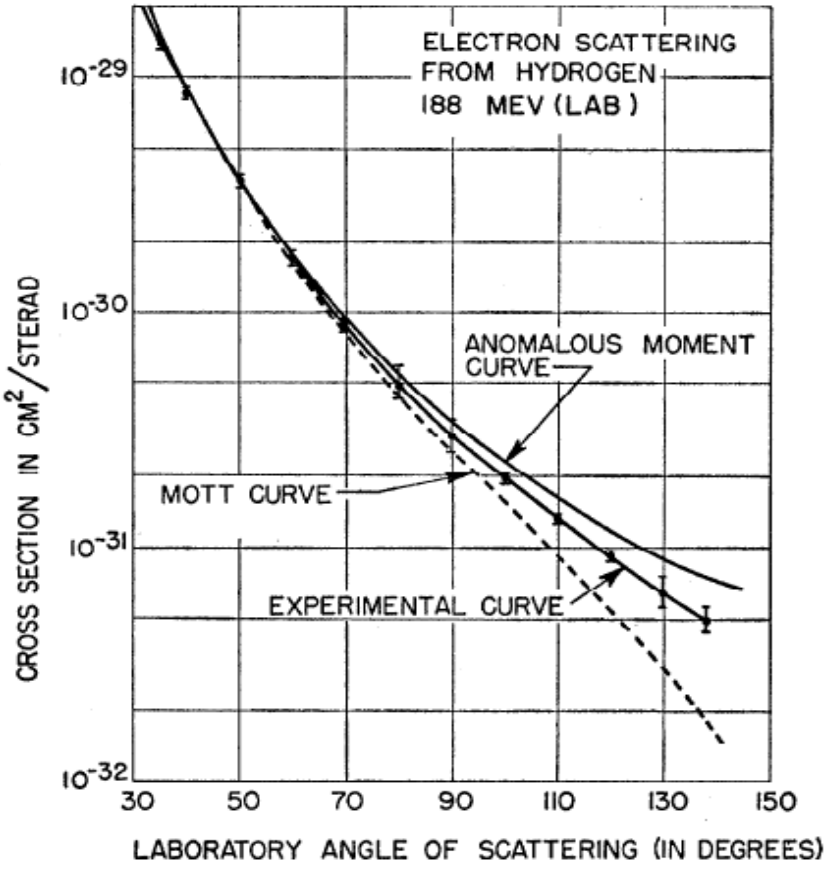

Figure 1.1: Measurements of the proton magnetic moment μ_p by the elastic scattering of electron beam from hydrogen gas [83].

1.1.2 Inelastic Structure Functions

The inelastic structure of nucleons (protons and neutrons) is probed in the Deeply Inelastic Scattering (DIS) of leptons (electrons and muons) from nucleons (Fig. 1.2). The unpolarized DIS cross section for the $e+p$ process can be written as (neglecting the lepton mass) :

$$\frac{d^2\sigma}{dE'd\Omega} = \frac{4\pi\alpha^2 E'^2}{Q^4}\left[W_2(\nu,Q^2)\cos^2\frac{\theta}{2} + 2W_1(\nu,Q^2)\sin^2\frac{\theta}{2}\right], \tag{1.8}$$

where α, θ, $E^{'}$ are the same as in Eq. 1.4, $Q^2 = -q^2 = (k-k^{'})^2$ with q being the four momentum transfer, ν is the energy transfer to the proton, given by $\nu = p\cdot q/M = E^{'} - E$ with the proton four-momentum p and $W_1(\nu,q^2)$ and $W_2(\nu,Q^2)$ are the inelastic structure functions analogous to the form factors in elastic cross sections and describing the internal substructure of the proton. Early experimental evidence showed that structure functions, unlike the form factors, do not decrease with increasing Q^2. Bjorken suggested in 1969 that at very high energy scattering with $Q^2 \to \infty, \nu \to \infty$ such that $\omega = 2M\nu/Q^2$ is constant and the structure functions become functions of the scaling variable ω only :

$$2MW_1(\nu,q^2) \;\to\; F_1(\omega) \tag{1.9}$$

$$\nu W_2(\nu,q^2) \;\to\; F_2(\omega). \tag{1.10}$$

This feature is called the 'scaling' of the structure functions with ω as the scaling variable. In the contemporary times, Feynman suggested in his parton model that at very high energy ($Q^2 \to \infty$), the protons behave as being composed of collinear point-like particles with the total proton momentum distributed among them. He termed these sub-particles as 'partons'. The scaling behavior found a natural explanation in the parton model of Feynman [68]. At high energy, leptons are scattered off point-like constituents called partons. In the infinite momentum frame, the scattering of the

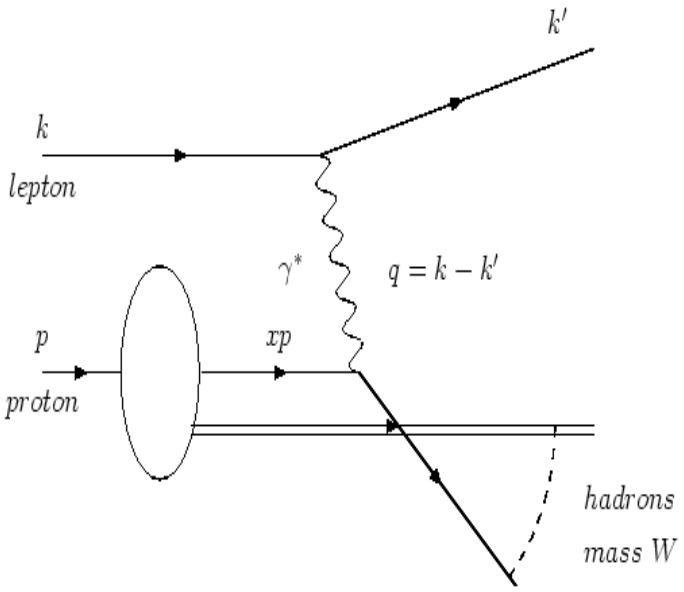

Figure 1.2: Diagrammatic view of Deep Inelastic Scattering.

lepton from one parton is independent of the other partons (electron probing small enough length scale) and therefore the structure functions become dependent only on the momentum fraction carried by the interacting parton. With this picture of the proton, the new scaling variable $x = 1/\omega$ was interpreted as the fraction of the proton momentum carried by the interacting parton.

The *ep* collider at HERA provided an enormous amount of data on the inelastic scattering cross section at various x values and over a wide range of Q^2 as can be seen in Fig. 1.3. The scaling violation at low x values indicated that proton is not composed only of 'free' quarks and the presence of gluons is implied. More on the polarized DIS experiments and polarized (polarized) structure functions are discussed in Sect. 1.4 and Sect. 1.4.1.

1.1.3 Quark Model and QCD

In the early 1960's, Murray Gell-Mann, George Zweig and Yuval Ne'eman proposed the classification of hadrons in terms of the $SU(3)$ symmetry suggesting that hadrons are composite particles and bound states of a group of fundamental particles

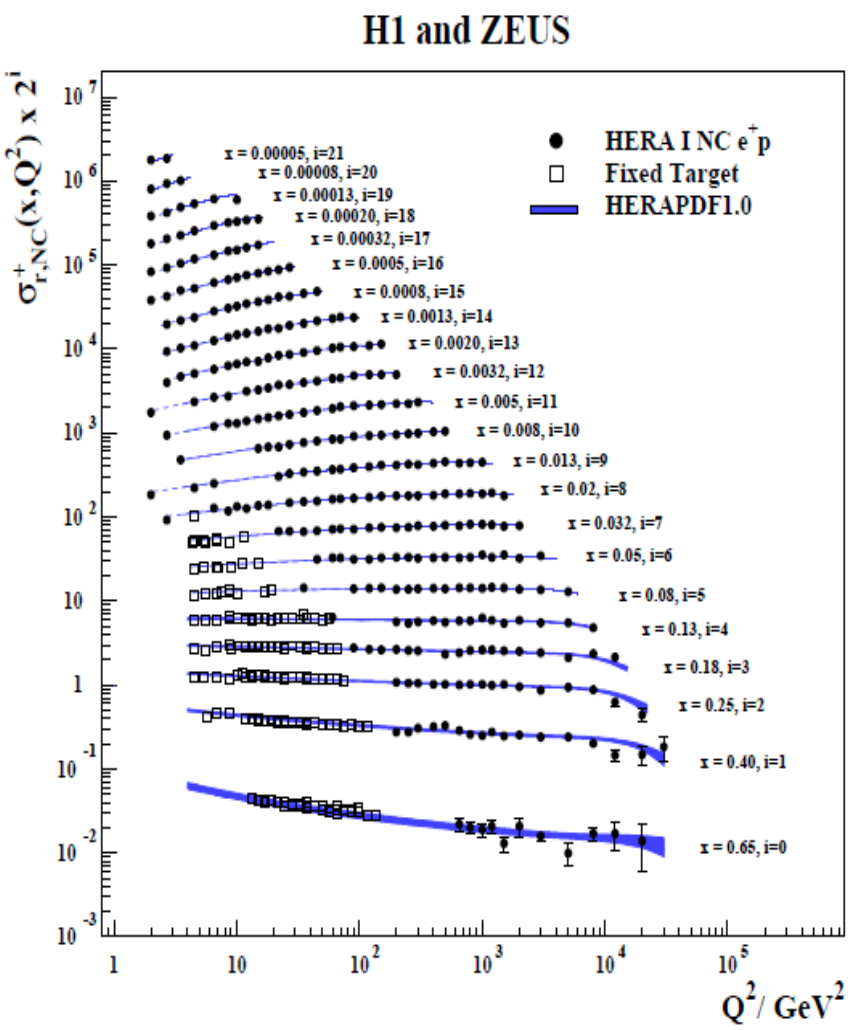

Figure 1.3: Structure function $F_2(x, Q^2)$ as a function of Q^2 and over a wide range of values of x from combined H1 and ZEUS data [3].

which Gell-Mann named 'quarks'. In their model, the suggested three such flavors of quarks (up, down and strange), in their bound states, made up baryons (quark triplets) and mesons (quark-anti-quark pairs). In the later parts of the 1960s, scattering experiments at SLAC [49] found evidence of such particles which were termed 'partons' (by Richard Feynman) at the time and were later identified with quarks. Up and strange quarks each have charge $+\frac{2}{3}e$ whereas down quarks have charge $-\frac{1}{3}e$ where e is magnitude of the charge of an electron. Present knowledge establish three

generations of quarks, each generation being a pair of quarks, one of which has charge $+\frac{2}{3}e$ and the other $-\frac{1}{3}e$. Three such quark pairs are up-down, strange-charm and top-bottom (also known as truth-beauty).

To account for the bound states of the quarks, the theory of Quantum Chromodynamics (QCD) was developed based on the works starting in the 1960s. QCD describes the interaction via the strong force that overcomes the electro-magnetic force to make the formation of the bound states of quarks and anti-quarks possible. QCD is analogous to the quantum theory of electromagnetic force (Quantum Electrodynamics or QED) in that QCD also is an interaction between charges (three different color-charges) mediated by massless bosons (called gluons). However, there is a fundamental difference as the mediating gluons can carry colors unlike photons (the mediating particle of QED) which are electrically neutral. The strong coupling constant α_s decreases logarithmically with the energy scale resulting in the 'asymptotic freedom' as well as 'confinement' of quarks and anti-quarks.

'Confinement' of the quarks and anti-quarks arise from the fact that at lower energy scales (for interactions at longer distances), the color force becomes increasingly stronger, requiring an infinite amount of energy to free a quark from its bound state. Practically, at longer distances, it becomes energetically favorable to produce quark anti-quark pairs (resulting in the fragmentation or hadronization process) than separating a quark from other quarks or anti-quarks. Therefore, quarks are always 'confined' to some form of bound state (triplets or paired with anti-quarks). Whereas, 'asymptotic freedom' ensures that at higher energy scales, probing interactions at smaller distance scales, the coupling constant (not really a 'constant' anymore!) gets smaller so that the quark and anti-quarks are 'nearly' free. In the calculation of a quantum-mechanical process cross sections, the superposition of an infinite number of possible intermediate states are considered. Probabilities of each possible intermediate state is proportional to the power/order of the coupling constant for the relevant

interaction. Since at lower energy scales $\alpha_s \sim 1$, probabilities of all intermediate states have comparable magnitudes, making it impossible to perform finite calculations. However, 'asymptotic freedom' ensures that at higher energy scales, (smaller distance scales, typically smaller than 1 fm), α_s is small enough so that the series of amplitudes of intermediate states can be truncated at certain orders of α_s, rendering such calculations finite. Such forms of QCD calculations are called 'perturbative' QCD (pQCD) analogous to the QED where the coupling constant is small enough ($\alpha_e \sim 1/137$) to make perturbative calculations possible.

1.1.4 PDF, Factorization and Universality

The parton model by Richard Feynman [68] suggested that interacting high momentum hadrons are a cohesion of partons (quarks and gluons) distributed over a range of momentum. The probability of finding a parton of flavor 'q' carrying a momentum fraction x of the total proton momentum, $f_q(x, Q^2)$ or simply $q(x, Q^2)$, is termed the 'parton distribution function' or PDF. A sample plot of unpolarized PDFs can be seen in Fig. 1.4. The structure functions $F_1(x, Q^2), F_2(x, Q^2)$ described in Eq. 1.8 can be viewed as the coherent superposition of partons according to their probabilities :

$$F_1(x) = \frac{1}{2}\sum_q e_q^2[q(x) + \overline{q}(x)] \tag{1.11}$$

$$F_2(x) = 2xF_1(x). \tag{1.12}$$

The collinear factorization theorem in pQCD [66, 55] envisions hadrons as a collection of collinear massless partons, each carrying a fraction of the hadron momentum. By this assumption, the partons inside the hadron have no transverse momentum with respect to the momentum of the initial state hadron and a final state hadron is also collinear with the scattered parton from which it is produced. The factorization

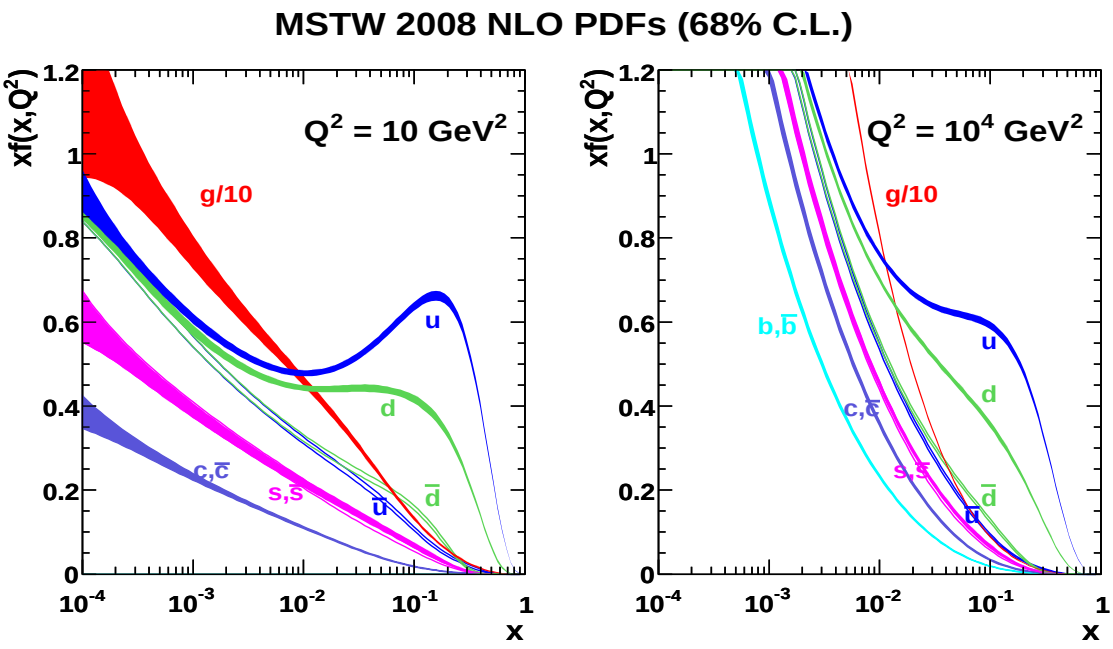

Figure 1.4: Unpolarized PDF of up, down, strange and charm quarks in the MSTW scheme [82] at two different energy scales.

introduces an energy scale μ which separates the soft (non-perturbative) and hard (perturbative) parts of the interaction process. The choice of this scale is arbitrary and typically μ is chosen to be the same as Q^2 or the fragmentation energy scale μ_f in case of final state hadrons. This scheme essentially enables one to write the process cross section as a convolution of soft, long-distance components such as the PDFs and fragmentation functions (FF) and hard, short-distance components as the partonic scattering cross section :

$$\begin{aligned}\sigma(pp \to hX) &= \sum_{ab\to cd} \int dx_a\ dx_b\ dz_c\ f_a(x_a,\mu^2) f_b(x_b,\mu^2) \\ &\quad \times D_c^h(z_c,\mu_f^2)\widehat{\sigma}(ab \to cd),\end{aligned} \tag{1.13}$$

where $f_a(x_a,\mu^2)$, $f_b(x_b,\mu^2)$ are the PDFs of parton favors 'a' and 'b', $D_c^h(z_c,\mu_f^2)$ is the fragmentation functions (FF) of production of hadron 'h' from parton 'c' and $\widehat{\sigma}$ is the cross section of the partonic process $ab \longrightarrow cd$.

The non-perturbative components such as the PDFs and FFs are universal in nature. These can be determined from convenient experiments and used for any describing any other experiments involving these components. Further discussions of factorization and its usefulness in describing experimental data can be found in Sect. 1.4.2.

1.2 Spin Structure of Proton

According to the present day knowledge, the proton is made of three valence quarks : two up quarks and a down quark and interacting gluons and 'sea' quarks (which are created and annihilated depending on the available energy). The total charge and the momentum of the proton is the sum of the charges and momenta of its constituent quarks. The early, non-relativistic quark models described proton spin also as the sum of the spins of its three constituent quarks. Later on, relativistic motion of quarks were taken into the considerations and in certain models (e.g Bag model [53]) total quark spin was suggested to be 75% of the proton spin, the remaining quarter coming from the quark angular momenta.

In the light of the emergent picture of the proton as a complex structure with valence quarks, sea quarks and gluons, the discrete sums were replaced with integrals of the spin distribution of the component partons. The polarized PDF is defined as the difference between the same and the opposite helicity states $\Delta q(x, Q^2) = \Delta f_q(x, Q^2) = f_q^{\uparrow}(x, Q^2) - f_q^{\downarrow}(x, Q^2)$. A sample parameterization of polarized PDF of up and down quarks can be seen in Fig. 1.5. The total spin contribution of a parton q is the integral $\int_0^1 dx f_q(x)$ at any energy scale Q^2.

The spin sum rule for the proton in the infinite momentum frame can be written as (Jaffe sum rule [73]) :

$$\frac{1}{2} = \frac{1}{2}\Delta\Sigma(Q^2) + \Delta G(Q^2) + L_q(Q^2) + L_g(Q^2), \tag{1.14}$$

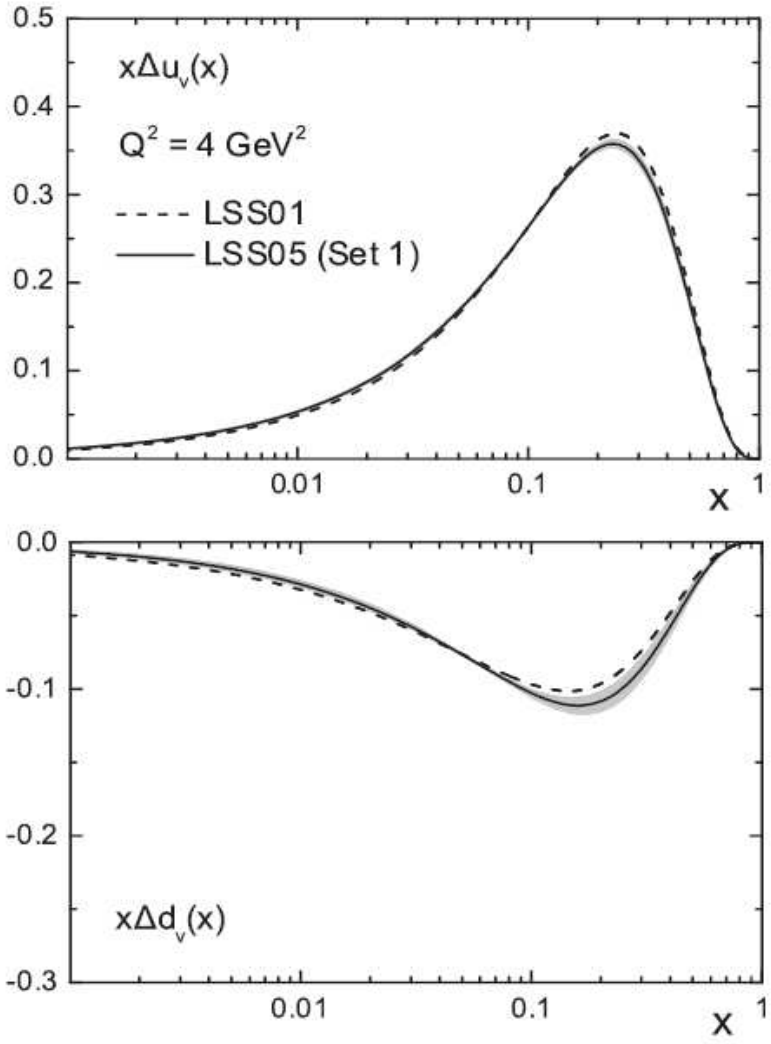

Figure 1.5: Polarized PDFs of up and down quarks (LSS parameterizations) [79].

where $\Delta\Sigma(Q^2)$ is the total spin of quarks and anti-quarks in proton, $\Delta G(Q^2)$ is the total gluon spin and $L_q(Q^2), L_g(Q^2)$ are the total angular momenta of quarks and gluons respectively at an energy scale Q^2.

The pDIS experiments collided polarized electrons or muons off polarized nucleon targets probing the quark spin distributions in the proton. The leptons interact with the quarks inside the proton via the electro-weak force in leading order (Fig. 1.2). For polarized DIS experiments, the scattering cross sections can be expressed as :

$$\frac{d^2\Delta\sigma}{d\Omega dE'} = \frac{4\alpha^2}{Q^2M^3}\frac{E'}{E}[M(E+E'\cos\theta)g_1(x,Q^2) - Q^2 g_2(x,Q^2)] \tag{1.15}$$

where Δ denotes the difference between same and opposite helicity states and $g_1(x,Q^2)$ and $g_2(x,Q^2)$ are the spin structure functions. The spin dependent structure function $g_1(x,Q^2)$ is given by :

$$\begin{aligned} g_1(x,Q^2) &= \frac{1}{2}\sum_q e_q^2[f_q^{\uparrow}(x,Q^2) - f_q^{\downarrow}(x,Q^2)] & (1.16)\\ &= \frac{1}{2}\sum_q e_q^2\ \Delta q(x,Q^2) & (1.17)\end{aligned}$$

Polarized DIS experiments measured asymmetries $A = (\sigma^{\uparrow\uparrow} - \sigma^{\uparrow\downarrow})/(\sigma^{\uparrow\uparrow} + \sigma^{\uparrow\downarrow})$ and extracted integrals of the spin structure function of proton $g_1^p(x,Q^2)$ [72], where

$$\int_0^1 dx g_1^p(x) = \frac{1}{2}\left[\frac{4}{9}\Delta u(Q^2) + \frac{1}{9}\Delta d(Q^2) + \frac{1}{9}\Delta s(Q^2)\right] \tag{1.18}$$

The weak axial-vector couplings could also be expressed as a combination of the quark spins. The isovector, color octet and singlet axial charges are :

$$\begin{aligned} g_A^{(3)} &= \Delta u - \Delta d & (1.19)\\ g_A^{(8)} &= \Delta u + \Delta d - 2\Delta s & (1.20)\\ g_A^{(0)} &= \Delta u + \Delta d + \Delta s & (1.21)\end{aligned}$$

From neutron β-decay experiments $g_A^{(3)} = 1.257 \pm 0.003$ and from hyperon β-decays $g_A^{(8)} = 0.60 \pm 0.05$ [45]. With the assumption of $\Delta s = 0$, it was suggested that $g_A^{(0)} = g_A^{(8)} \simeq 0.60$, or, in other words, the prediction was that the net quark spin $\Delta\Sigma = \Delta u + \Delta d$ was 60% of the proton spin. Based on similar arguments, the 'Ellis-Jaffe Sum Rule' predicted the integral value of spin-dependent structure function $\int_0^1 dx g_1^p(x)$ to be 0.187 [65].

1.3 Proton Spin Crisis

The Stanford Linear Accelerator (SLAC) conducted $e + p$ polarized deep inelastic scattering experiments in the 1970s and 1980s [46, 37]. Later on, the European Muon Collaboration (EMC) at CERN in the later part of the 1980s conducted polarized DIS experiments with polarized muons scattering off polarized targets. In the results published in 1989 [44] (combined with SLAC results), EMC claimed 'The spin-dependent structure function $g_1(x)$ for the proton has been determined and ... its integral over x found to be $0.126 \pm 0.010(\text{stat.}) \pm 0.015(\text{syst.})$, in disagreement with the Ellis-Jaffe sum rule'. This result concluded that the total quark spin constitutes a much smaller

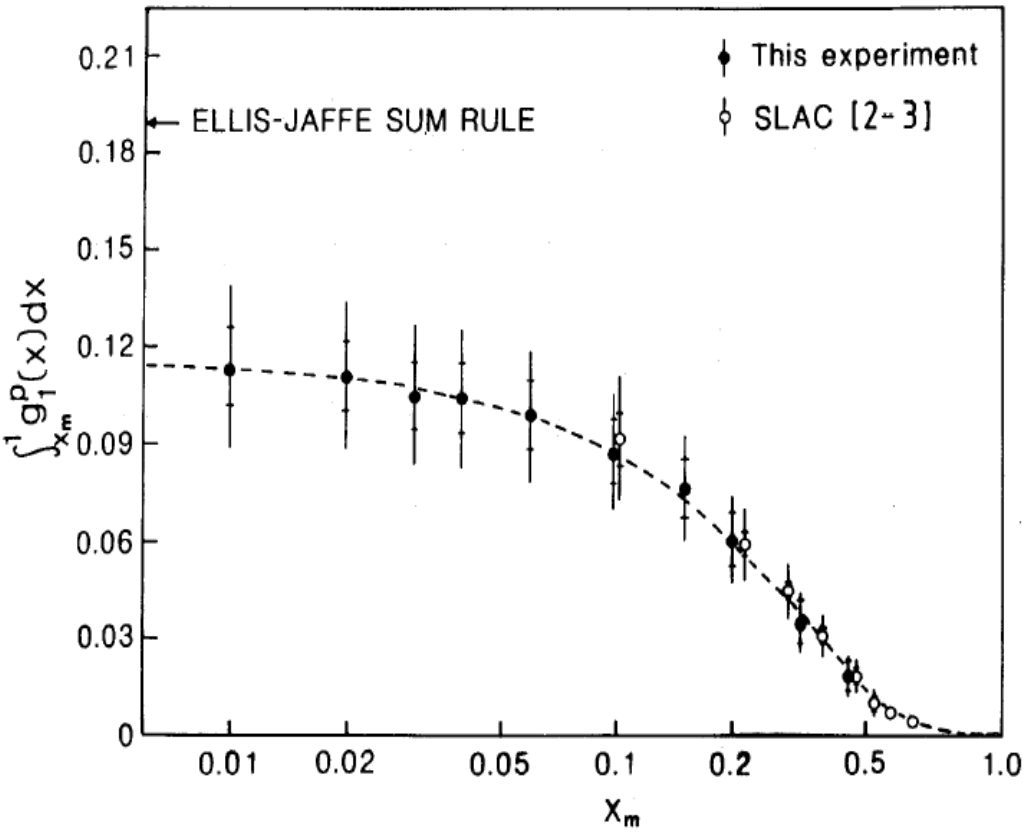

Figure 1.6: EMC result in 1989 for $\int_0^1 g_1^p(x)dx$ contradicting the Ellis-Jaffe Sum Rule.

fraction of proton spin than had been predicted ($\Delta\Sigma \simeq 0.60$) thus far. In fact no more

than 25% of the proton spin was from the constituent quark spin. The subsequent querry for the rest of the proton spin was termed as the *spin crisis*.

1.4 Continuing The Search

The results from the EMC [44] and SLAC experiments [46, 37] (also corroborated by high precision results from SLAC [5, 4] and the results in the low-x region from HERMES [32] in recent times) proved that three-quarters of the proton spin comes from sources other than the quark spin. Soon after, there were some theoretical predictions that the gluon spin might be quite large and positive. These predictions as well as the consideration that the gluon spin was accessible through experiments (whereas the orbital angular momenta of the quarks and the gluons were not) turned the attention of spin physics experiments toward gluons.

However, DIS experiments which were very successful in probing the quark structure of the protons by scattered leptons via the electroweak interactions (Fig. 1.2) were not ideal for studying the gluons. Gluons interact via the strong force and only when it produces a quark anti-quark pair (one of them interacts with the impinging lepton via electroweak force) in higher order interaction terms can DIS probe gluons. New ideas of accessing gluon spin emerged soon. In the polarized proton-proton collisions, gluons interacted with quarks or other gluons at leading order and the gluon spin distribution is accessible through measurements of the production asymmetries of different species of particles.

1.4.1 Polarized DIS and the Evolution Equation

Various polarized DIS experiments measured the spin-dependent structure function $g_1(x, Q^2)$ over different ranges of Q^2 and for different x values (Fig. 1.8).

At high Q^2 and intermediate x-range, the spin structure function $g_1(x, Q^2)$ is independent of Q^2 and is a function of the scaling variable x ($g(x, Q^2) \rightarrow g_1(x)$).

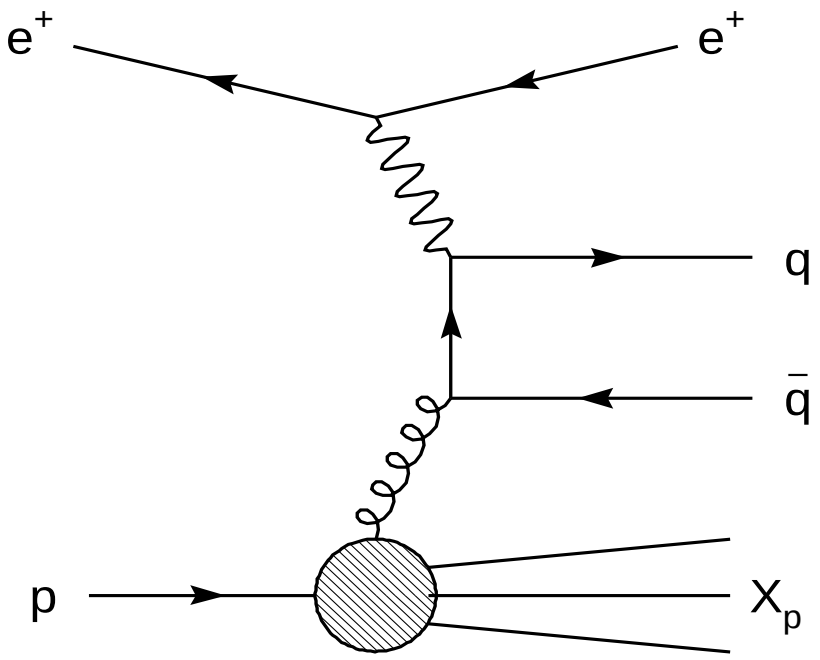

Figure 1.7: NLO diagram of DIS involving gluon from proton.

However, the data showed positive slopes at low x and negative slopes at very high x (more prominent in the unpolarized structure function data in Fig. 1.3). These 'scaling violations' were understood with the help of the DGLAP (Dokshitzer-Gribov-Lipatov-Altarelli-Parisi) (Q^2-)evolution equations [41].

$$\frac{d}{dt}\begin{pmatrix}\Delta\Sigma\\ \Delta g\end{pmatrix} = \frac{\alpha_s(t)}{2\pi}\begin{pmatrix}A_{qq} & 2fA_{qg}\\ A_{gq} & A_{gg}\end{pmatrix}\begin{pmatrix}\Delta\Sigma\\ \Delta g\end{pmatrix}, \tag{1.22}$$

where $t = ln(\frac{Q^2}{\mu^2})$ and f is the number of quark flavors. $\Delta g(x, Q^2)$ can be accessed from polarized DIS data by using initial parameterizations and applying DGLAP evolution to the relevant energy scale. However, polarized data came from fixed target experiments (HERA provided unpolarized data for an enormous range of Q^2 providing a huge lever arm for the Q^2 evolution equations) which was a handicap in

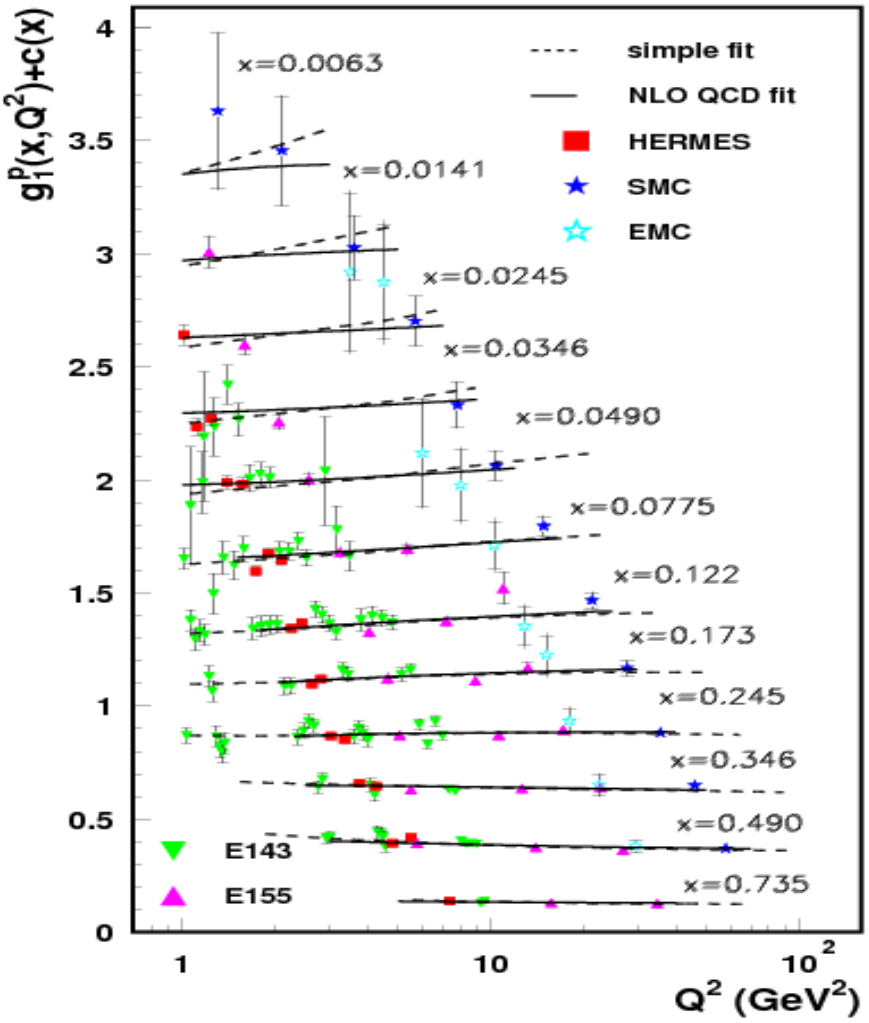

Figure 1.8: World data on g_1^p from polarized DIS experiments [92].

terms of achieving high energy scale and soon the polarized pp collisions opened up new possibilities of accessing the gluon spin distribution.

1.4.2 Hard Interaction in the Polarized Hadron Collisions

As described in Sect. 1.1.4, the collinear factorization principle in pQCD allows the (lepton-hadron or hadron-hadron) scattering process to be broken into two parts, soft or long-distance nonperturbative components, e.g. parton distribution functions (PDF) and fragmentation functions (FF), and hard or short-distance perturbative

components (partonic cross sections calculable in pQCD, for high enough Q^2). Fragmentation Functions (FF) are the probabilities of a scattered parton fragmenting into a particular hadron with fraction z of its momentum. They are universal and are measured in $e^+ + e^-$ annihilation or semi-inclusive DIS experiments. PDFs are parameterized and the parameters are extracted from fits to the experimental data. Unpolarized quark PDFs are quite well constrained from DIS and semi-inclusive DIS data.

For the relevant energy (center-of-mass energy $\sqrt{s} = 62.4$ GeV) and transverse momentum range ($0.5 \leq p_T \leq 4.5$ GeV/c) of the final state hadron for our analysis, consider a pp collision producing a hadron (e.g. pion) as shown in the cartoon below (Fig. 1.9). For this process, the factorization allows the cross section to be expressed

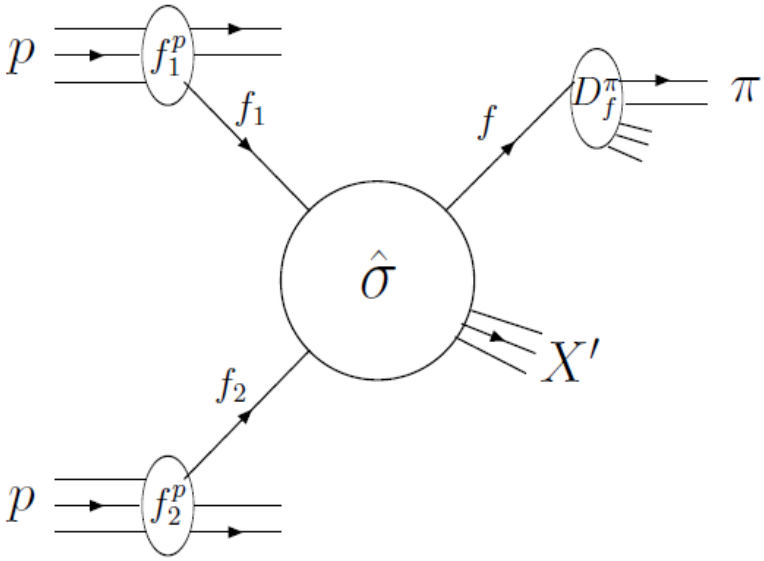

Figure 1.9: Cartoon of a proton-proton collision with a quark-gluon hard scattering producing a pion and other debris X.

in terms of the interacting parton PDFs (f_1, f_2), cross section of hard scattering ($\widehat{\sigma}$) of the partons and fragmentation function D^π of a final state pion carrying momentum fraction z. Colliding longitudinally polarized proton beams provides sensitivity to the

gluon helicity distribution function at leading order. The helicity-dependent difference in hadron h production, $p + p \rightarrow h + X$, is defined as :

$$\frac{d\Delta\sigma}{dp_T} \equiv \frac{1}{2}\left[\frac{d\sigma^{++}}{dp_T} - \frac{d\sigma^{+-}}{dp_T}\right]$$

where $++$ and $+-$ respectively refer to the same and the opposite helicity combinations of the colliding protons [50]. Instead of directly measuring the helicity dependent cross section difference $d\Delta\sigma/dp_T$, we extract the double longitudinal spin asymmetry A_{LL} defined as the ratio of the polarized to unpolarized cross sections :

$$A_{LL} = \frac{d\Delta\sigma/dp_T}{d\sigma/dp_T}. \tag{1.23}$$

Using factorization, one can relate the experimentally measured quantity A_{LL} to the theoretical expression. As an example, considering a mid-rapidity positive pion produced with transverse momentum $p_T \sim 2$ GeV/c from polarized $p + p$ collision at $\sqrt{s} = 62.4$ GeV, the most dominant process is scattering of an up-quark with a gluon producing another up-quark that fragments into a positive pion. The measured A_{LL} for such positive pions can be expressed as :

$$A_{LL} \sim \frac{\Delta u(x) \otimes \Delta g(x) \otimes \Delta\widehat{\sigma}^{ug\rightarrow uX} \otimes D_u^{\Pi^+}(z)}{u(x) \otimes g(x) \otimes \widehat{\sigma}^{ug\rightarrow uX} \otimes D_u^{\Pi^+}(z)} \tag{1.24}$$

$$\sim \frac{\Delta u(0.1)}{u(0.1)} \otimes \frac{\Delta g(0.1)}{g(0.1)} \otimes \widehat{a}_{LL}^{ug} \tag{1.25}$$

where Δ denotes the difference of the quantity for same and opposite helicity states, $\widehat{a}_{LL}^{ug}$ is termed as the 'analyzing power' for the specific subprocess ($ug \rightarrow ug$). For the relevant conditions (probing x 0.1), $\Delta u(0.1)/u(0.1) \sim 0.4$, $\widehat{a}_{LL}^{ug} \sim 0.6$ (from Fig. 1.4 and Fig. 1.10). For $\Delta g(0.1) \sim 0.01$ (typical value from fits of parameterization to data, as will be seen later in Sect. 7), one can expect to measure asymmetries $\sim 10^{-3}$.

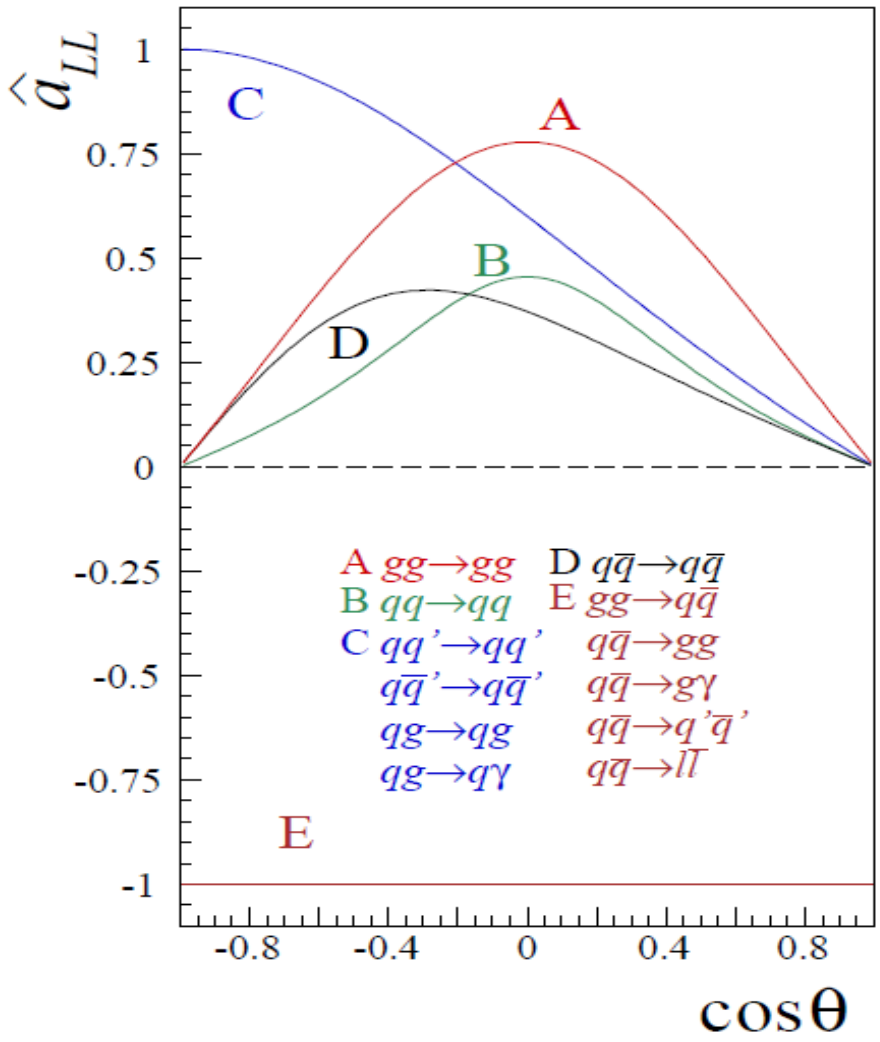

Figure 1.10: Analyzing power $\widehat{a}_{LL}$ for different partonic subprocesses [50].

Polarized and unpolarized quark PDF's are well constrained with a wide range of data from DIS and polarized DIS experiments and the gluon PDF $\Delta g(x, Q^2)$ is extracted from fitting experimentally measured asymmetry (A_{LL}) data. As shown in the previous subsection, the asymmetry result can be equated to a combination of PDFs and the analyzing power of partonic subprocesses which are calculable using pQCD. PHENIX experiment has published single and double spin asymmetries as well as production cross sections of various species (neutral pions [14], direct photons [27], etas [17], charged hadrons, jets [28, 19], W bosons [18]) for longitudinal

and transversely polarized proton-proton collisions at various center of mass energies (62.4, 200 and 500 GeV) to understand the spin-structure of the proton. For our analysis, we measure the unpolarized cross section and longitudinal double helicity asymmetry of mid-rapidity production of inclusive non-identified charged hadrons with the transverse momentum range $0.5 \leq p_T \leq 4.5$ GeV/c from $p+p$ collisions with the center of mass energy of 62.4 GeV.

1.4.3 Extracting Gluon Spin Information from Measurements

In the recent years, several groups have worked towards determining polarized PDFs of quarks and gluons using the available data from various experiments (polarized DIS and RHIC data). The strategy for such a global analysis [93] is as follows : ansatz of the functional forms of the PDFs with free parameters at an initial energy scale μ_0 are made and they are evolved to a scale μ_f relevant for a certain data point. Parton distributions at scale μ_f are used (in conjunction with fragmentation functions and partonic scattering cross sections) to calculate the theoretical predictions (of cross sections or asymmetries) and a χ^2 is assigned for the comparison to each of the data points. The free parameters in the ansatz are then varied until eventually a global minimum (for the set of data points) in the χ^2 space is reached.

In practice, the computation of the cross sections beyond the lowest order in the perturbation theory is not viable because of the extremely time-consuming nature of the computations. Computation for the polarized cross sections are even harder than their unpolarized counterparts since the unpolarized PDFs are known to much better accuracy and the polarized PDFs are not. However, in the late 1990's, a technique of performing the calculations in the Mellin-n moment space was introduced for both DIS data [71] and hadron collisions [77]. In this technique, for the polarized case, the polarized PDFs are expressed in terms of their Mellin moments defined as :

$$\Delta f_q^n(\mu) = \int_0^1 dx x^{n-1} \Delta f_q(x,\mu). \tag{1.26}$$

This renders the convolutions to simple products of the moments. The evolutions of PDFs are done in the Mellin-n space and the evolved PDFs in the x-space can be recovered by the inverse Mellin transform and finally the factorized polarized cross sections are calculated using the Mellin moments and other pre-determined components (e.g. calculated partonic cross sections).

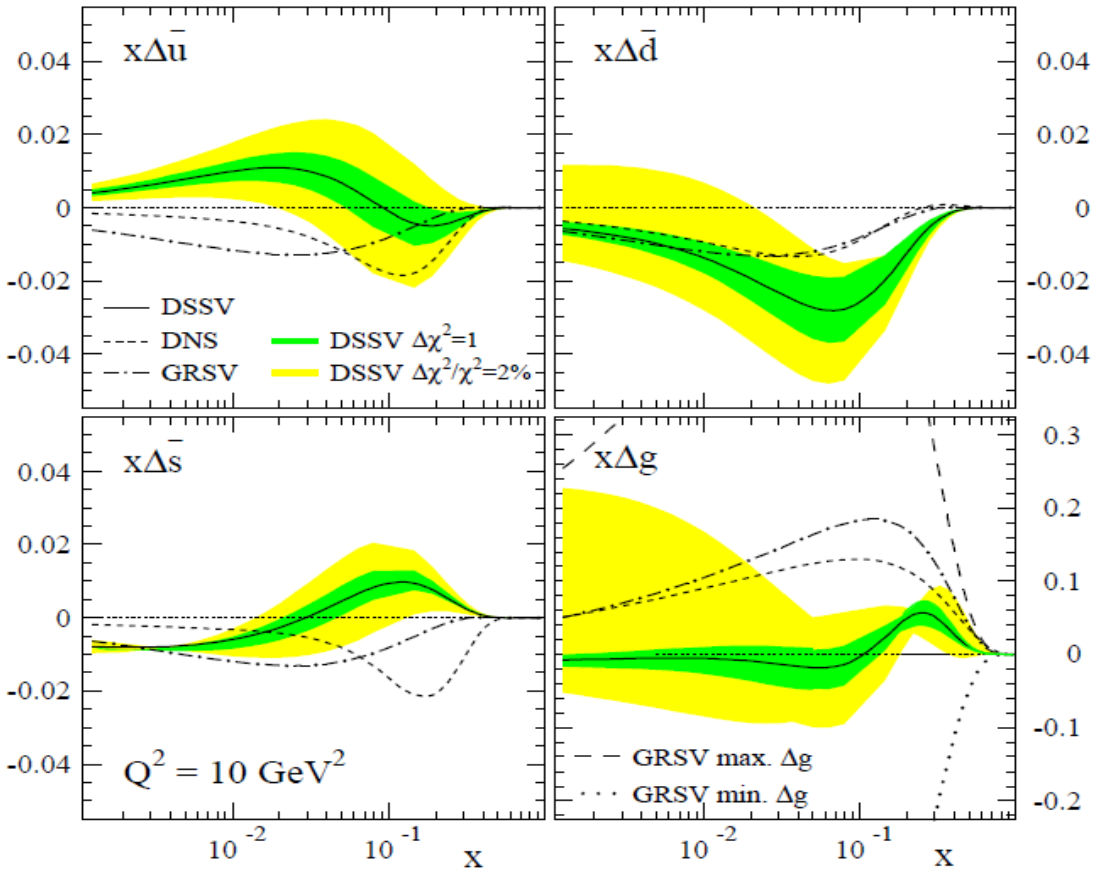

Figure 1.11: Sea quark and gluon distributions from DSSV compared to GRSV parameterizations. Shaded bands correspond to $\Delta\chi^2 = 1$ (online color green) and $\Delta\chi^2/\chi^2 = 2\%$ (online color yellow) [59].

Such techniques have made it possible to perform higher order (NLO, NLL) calculations while extracting the polarized PDFs from experimental data. One such global analysis utilizing both polarized DIS data (from COMPASS, HERMES, EMC, SMC, CLAS and various SLAC experiments) and RHIC data (PHENIX π^0 and STAR jet)

have been performed in 2008 to determine quark and gluon helicity distributions in polarized protons [59]. Later in the present work, we compare our measurements with pQCD calculations involving parameterizations of PDFs from various groups using (slightly) different functional forms extracted from global analysis of polarized data from various experimental sources. Glück-Reya-Stratmann-Vogelsang (GRSV) [70], Leader-Sidorov-Stamenov (LSS) [79] and Blümlein-Böttcher (BB) [47] have used pDIS data to parameterize PDFs whereas deFlorian-Sassot-Stratmann-Vogelsang (DSSV) [59] used polarized DIS as well as RHIC data to extract parameters of the functional forms of the PDFs. Sample plot in Fig. 1.11 shows the distribution of sea quarks and gluons as extracted from pDIS and RHIC data in DSSV parameterization.

1.5 Motivation for Our Measurements

The comparison of cross section predictions with data on single inclusive hadron production in the hadronic collisions, $p + p \to h + X$, is important for understanding the pQCD. For hadrons produced with transverse momenta $p_T \gg \Lambda_{QCD}$, the cross section factorizes into a convolution involving long-distance and short distance components. The long distance components, PDFs and FFs, can be extracted from other processes. This allows for a test of the short-distance part of the convolution which can be estimated using pQCD. In particular, differences between data and predictions can indicate the importance of neglected higher order terms in the expansion or power-suppressed contributions [61].

NLO pQCD and collinear factorization successfully describe cross section measurements at $\sqrt{s} = 200$ GeV of neutral pion production at mid-rapidity [14, 7] and forward rapidity [10], mid-rapidity jets [19, 28, 6] and direct photons [27] measured at RHIC by the PHENIX and STAR collaborations. However, at lower center-of-mass energies, in particular in the fixed-target experiments with $20 \lesssim \sqrt{s} \lesssim 40$ GeV, NLO

pQCD calculations significantly under predict hadron production, by factors of three or more [61]. The consistency between NLO estimations and the data at low $\sqrt{s}$ was improved [61, 62, 39] by including the resummation of large logarithmic corrections to the partonic cross section to all orders in the strong coupling α_s. The corrections are of the form $\alpha_s^k \ln^{2k}(1-\hat{x}_T^2)$ for the k-th order term in the perturbative expansion. Here $\hat{x}_T \equiv 2\hat{p}_T/\sqrt{\hat{s}}$, where $\hat{p}_T = p_T/z$ is the transverse momentum of the parton fragmenting into the observed hadron with a fraction z of the parton transverse momentum, and $\sqrt{\hat{s}} = \sqrt{x_1 x_2 s}$ is the partonic center-of-mass energy where $x1, x2$ are momentum fractions carried by two interacting partons. The corrections are especially relevant in the threshold regime $\hat{x}_T \to 1$ in which the initial partons have just enough energy to produce a high-transverse-momentum parton fragmenting into the observed hadron. In this regime gluon bremsstrahlung is suppressed, and these corrections are large [62]. However, the addition of the resummed NLL terms to an NLO calculation may not provide the best means of describing data in a given kinematic region, for example, if the (unknown) higher-order terms that are omitted from the calculation have comparable magnitude and opposite sign to the NLL terms. It is therefore important to test pQCD calculations against data in a region of intermediate $\sqrt{s}$, better defining the kinematic ranges over which pQCD calculations can be applied with confidence.

The data presented here from non-identified single inclusive charged hadron production so allow a test of NLO and NLL predictions. Alternatively, assuming the reliability of the short-distance aspects of the theory, the data may be used to refine our knowledge of the hadron fragmentation functions. These cross section measurements of non-identified charged hadrons (combinations of $\pi^{\pm}$, $K^{\pm}$, $p^{\pm}$) are also important as baselines for extracting nuclear modification factors in high p_T hadron production in heavy ion collisions at RHIC [29, 23].

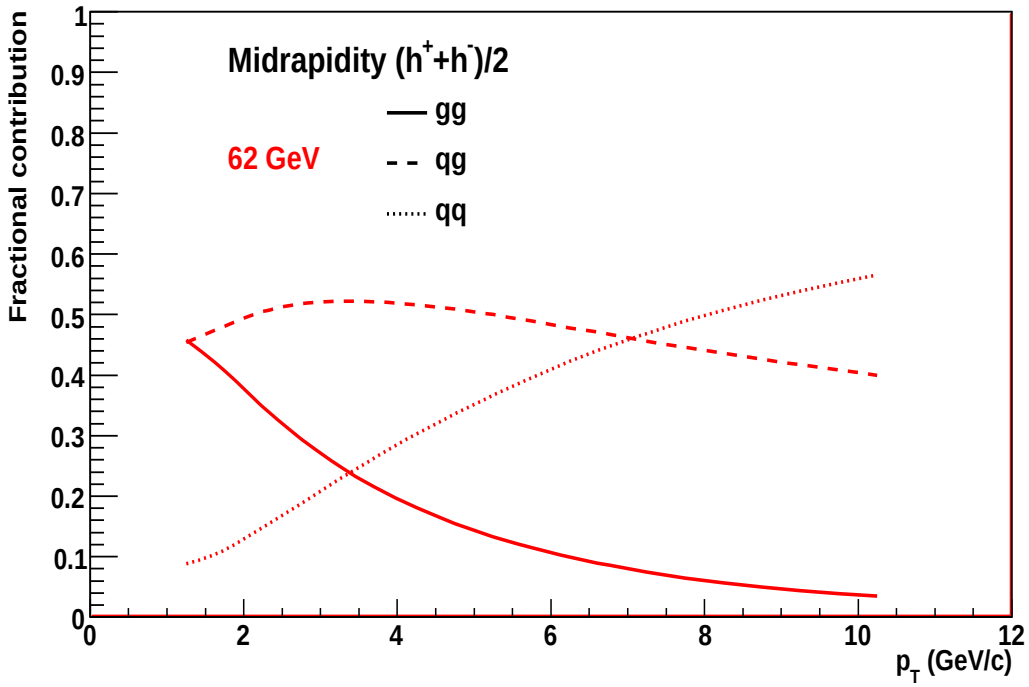

Figure 1.12: Partonic sub-process contributions at $\sqrt{s} = 62.4$ GeV.

As can be seen in Fig. 1.12, the production of the final state hadrons at mid-rapidity from $p + p$ at $\sqrt{s} = 62.4$ GeV, in the transverse momentum range $1.5 \leq p_T \leq 4.5$ GeV/c, is dominated by the quark-gluon scattering [95]. This makes the asymmetries reported here, $A_{LL}(p + p \rightarrow h^{\pm} + X)$, sensitive to the polarized gluon PDF $\Delta G(x)$ at leading order, and more sensitive to its sign than processes dominated by gluon-gluon scattering. For example, preferential fragmentation of the up quark into positive pions and that of the down quark into negative pions, combined with the fact that the up quark helicity PDF is positive and the down quark helicity PDF is negative, would lead to an ordering of the asymmetries of pions (charged and neutral) directly sensitive to the sign of the gluon helicity PDF. Positive $\Delta g(x)$ would lead to $A_{LL}^{\pi^+} \geq A_{LL}^{\pi^0} \geq A_{LL}^{\pi^-}$ whereas a negative $\Delta g(x)$ would imply an opposite ordering. The measurements at the present energy ($\sqrt{s} = 62.4$ GeV) are also sensitive to the gluon helicity distribution in the higher end of the x-range probed than the results

from other available energies ($\sqrt{s} = 200, 500$ GeV) at RHIC as $x_T = 2p_T/\sqrt{s}$ (as can be seen from Figures 1.13 and 1.14). These results can be combined with data from polarized collider and fixed target experiments in a global analysis to reduce uncertainties on the gluon helicity distribution [59, 60].

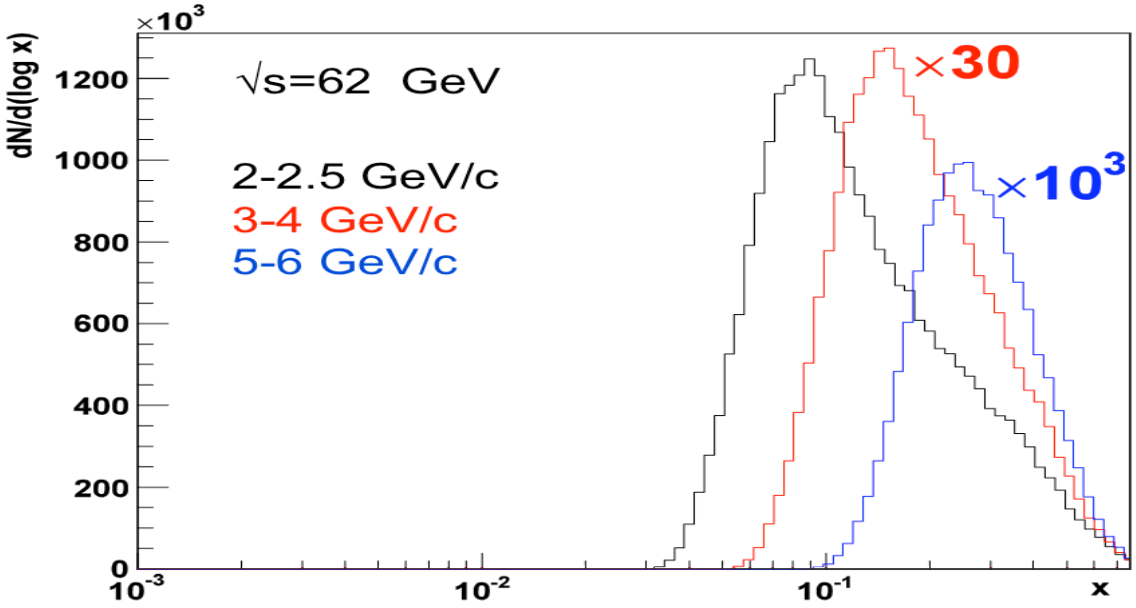

Figure 1.13: Bjorken x range probed for $\sqrt{s} = 62.4$ GeV.

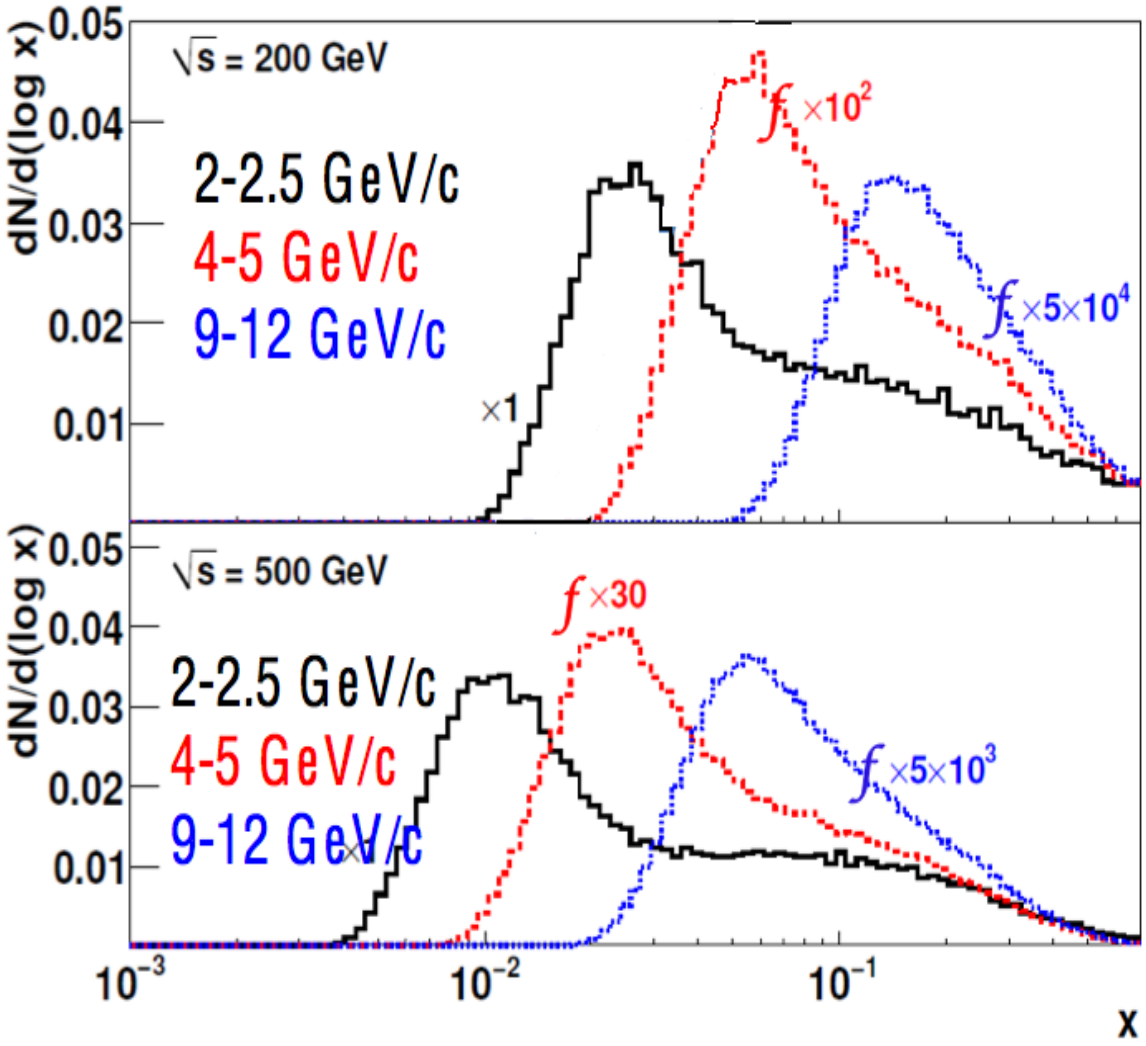

Figure 1.14: Bjorken x range probed for other RHIC energies.

CHAPTER 2

ACCELERATOR AND DETECTORS

The Relativistic Heavy-Ion Collider (RHIC) at Brookhaven National Laboratory (BNL) is a unique facility to study proton spin structure by colliding two polarized proton beams or study the state of matter in heavy ion ($d + Au$, $Cu + Cu$, $Au + Au$) collisions. Most prominent of the collaborations at RHIC are : BRAHMS, PHENIX, PHOBOS and STAR. PHOBOS was decommissioned in 2005 and BRAHMS completed data taking in June, 2006.

2.1 Polarized Protons at RHIC

The Relativistic Heavy-Ion Collider (RHIC) at Brookhaven National Laboratory (BNL) on Long Island, New York, is the accelerator facility built for the study of the state of matter at very high temperature through collisions of heavy ions ($d + Au$, $Cu + Cu$, $Au + Au$) and for the study of the spin structure of the proton using the collisions of polarized $p + p$. RHIC is the only polarized $p + p$ collider in the world, providing a unique opportunity for studying the proton spin structure. Each of the two storage rings at the accelerator is 3.8 km in circumference and there are six interaction points (IPs) for beam collisions (Fig. 2.1). There have been four different experiments at four of these IP's in the recent times : BRAHMES, PHENIX, PHOBOS and STAR. A detailed description of the RHIC as a polarized proton collider can be found in [34].

At RHIC, the design luminosity for the polarized $p+p$ is $2 \times 10^{32}\text{cm}^{-2}\text{s}^{-1}$ and the design polarization for the proton beams is 70%. A maximum of 120 proton bunches

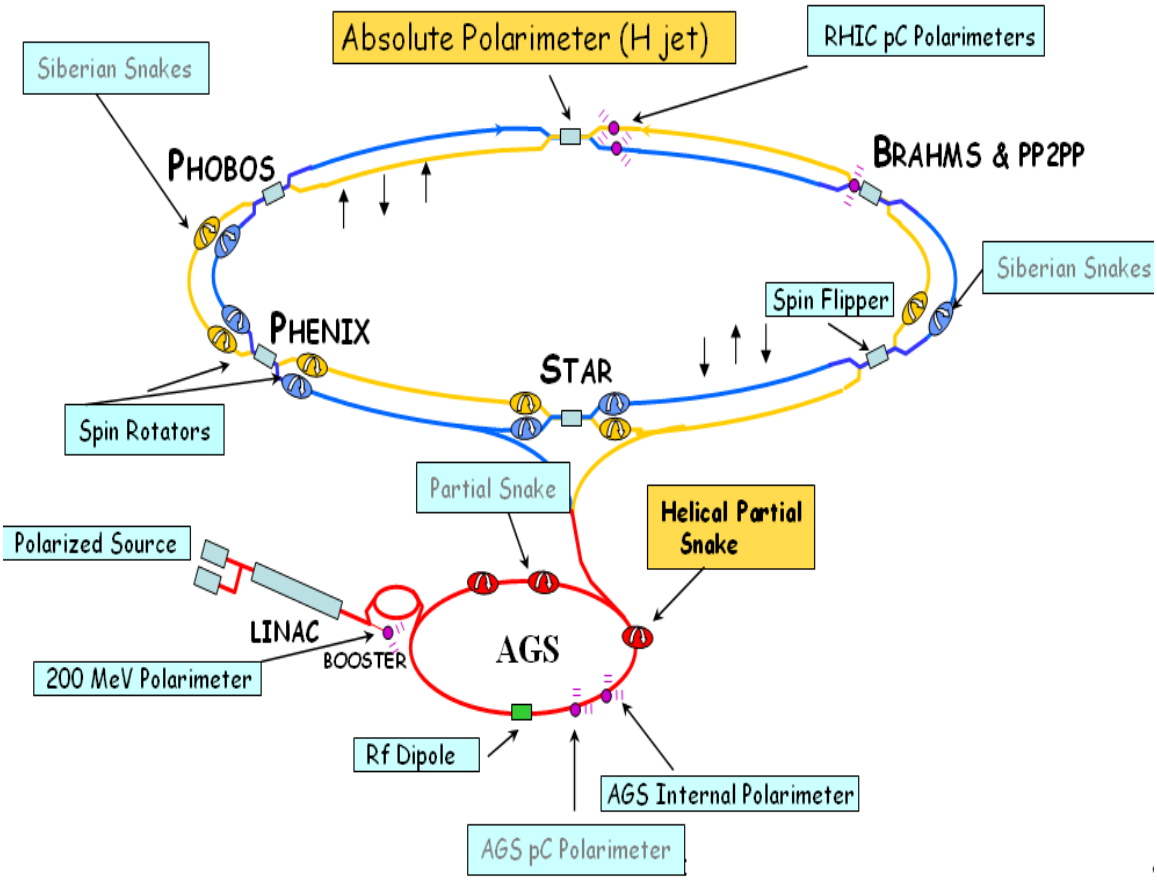

Figure 2.1: RHIC schematic.

can be injected into the storage rings, producing collisions of bunches at the IPs every 106 ns. To date, RHIC has produced polarized $p+p$ collisions at the center of mass energies ($\sqrt{s}$) of 62.4, 200 and 500 GeV. A chronological record of the performance of RHIC for the polarized $p+p$ collisions is presented in Table 2.1

2.1.1 Polarized Proton Source

At RHIC, polarized proton beams are produced by the Optically Pumped Polarized H^- Ion Source (OPPIS) technique which is based on spin transfer between the proton or atomic hydrogen atom at the energy of a few KeV and optically pumped alkali metal (rubidium) vapors. Polarized H^- ions produced in the OPPIS at 35 KeV and $\sim 80\%$ polarzation are passed through a RFQ and LINAC and accelerated to 250

Year	Beam energy GeV	Delivered luminosity b^{-1}	Average store polarization
2002	100.0	1.4 p	14 %
2003	100.0	5.5 p	34 %
2004	100.0	7.1 p	46 %
2005	100.0	29.5 p	47 %
2006	100.0	88.6 p	55 %
	31.2	1.05 p	50 %
2008	100.0	38.4 p	44 %
2009	250.0	110 p	34 %
	100.0	115 p	56 %
2011	250.0	166 p	48 %

Table 2.1: A list of performance of RHIC in polarized $p+p$ collisions over the years.

MeV with 50% efficiency. Next the beam is passed through to a booster ring where it is accelerated to ~ 2 GeV. Proton bunches from the booster are injected into the Alternating Gradient Synchroton (AGS) and accelerated to about 25 GeV. Maintaining the polarization throughout the acceleration in the AGS is a difficult proposition since the beams undergo various depolarizing effects e.g. matching of the betatron frequency with spin precession frequency and horizontal magnetic field present in the accelerator. To reduce the depolarizing effects, a device called the 'Siberian Snake' - described in the following Sect. 2.1.2 - is implemented. However, due to the lack of space, only partial (5%) snakes are used in the AGS. The addition of another 15% 'cold snake' [90] in 2005 significantly improved beam polarizations in the subsequent years.

2.1.2 Depolarizing Effects and the Siberian Snake

For a proton with charge e and momentum $\vec{p}$ moving through a magnetic field, the equations of motion of the proton and its spin vector in its instantaneous rest frame are described by the Lorentz equation and the Thomas-BMT equation respectively :

$$\frac{d\vec{p}}{dt} = -\frac{e}{m\gamma}\left\{\vec{B}_{\perp}\right\} \times \vec{p}, \tag{2.1}$$

$$\frac{d\vec{s}}{dt} = -\frac{e}{m\gamma}(1+\gamma G)\vec{B}_{\perp} + (1+G)\vec{B}_{\parallel} \times \vec{s}, \tag{2.2}$$

where $\vec{B}_{\perp}$ and $\vec{B}_{\parallel}$ are the components of the magnetic field in perpendicular and parallel to the momentum respectively, γ is the relativistic boost E/m and G is the anomalous magnetic moment of the proton. For high energy protons (large γ), the $\vec{B}_{\perp}$ term dominates. For highly energetic protons, therefore, the spin rotates γG times faster compared to the motion of the proton (orbital motion). This number is termed as 'spin tune' ν_{sp}.

If the beam encounters any perturbing effect matching the frequency of the spin precession, resonances occur, amplifying the depolarizing effect. Depolarization resonance effects on the accelerating proton beams are usually from two sources : intrinsic effects and imperfections of magnetic fields. Intrinsic depolarizing effects occur when the betatron oscillation frequency matches the spin precession tune ν_{sp}. The second type of depolarization comes into effect when the rotating polarized beam is affected by an imperfection in the (focusing) magnetic field each revolution and the frequency of the imperfection in the field matches the spin tune. In such cases, the spin is in the same phase each time the protons pass through the depolarizing field. The matching of frequencies of depolarizing effects with that of the beam rotation on the resonance effects are demonstrated in the cartoon Fig. 2.2.

'Siberian Snakes' were the ingenious devices developed (in Russia, as the name suggests) to counter the depolarizing effects in synchrotons. It is a device with a series of helical magnets field causing the spin vector to rotate each time the bunches pass through the snake. A snake rotating the spin vector by 180° is a 'full snake' (Fig. 2.3). A complete rotation of the spin vector through the snake during a revolution flips the spin direction every rotation, reversing the depolarizing perturbations in each rotation and thus preserves the beam polarizations. As mentioned before, partial snakes are used in AGS for lack of enough space. The RHIC storage rings, however, are fitted with 100% snakes.

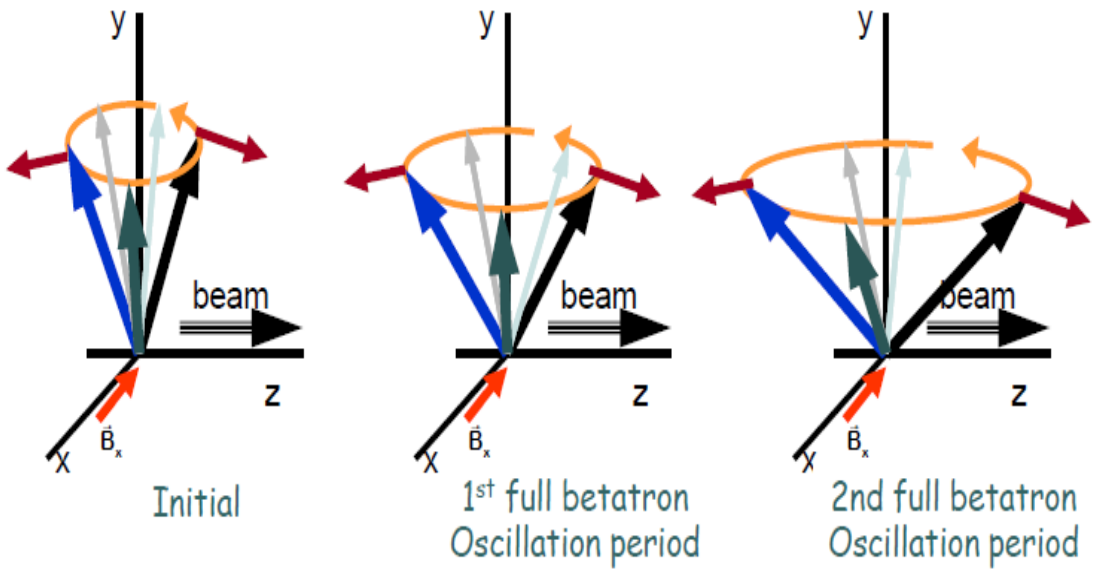

Figure 2.2: Cartoon showing amplified depolarizing effect with successive rotations of the beam for resonance.

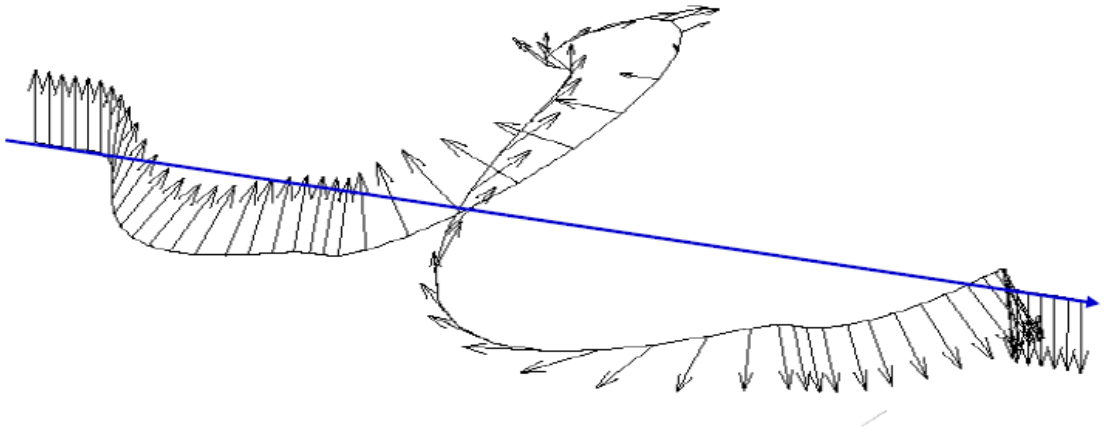

Figure 2.3: Diagram of the magnetic field of a full siberian snake rotating the spin direction by 180°.

2.1.3 Accelerator

Polarized proton bunches at 25 GeV from AGS are injected into the accelerator/storage rings where they are further accelerated to the required collision energy (e.g. $31.2, 100, 250$ GeV). A group of proton bunches (120 at most) in each ring is termed as a 'fill' and are tagged with a number. Each fill is kept rotating in the storage

ring (and colliding at the IPs) for typically $7-8$ hours. At RHIC, the proton bunches in a ring are given a set pattern of successive spin configurations in any particular fill. In consecutive fills, the patterns of colliding spin configurations are changed. Four different spin configurations, as described in Fig. 2.4, are used in successive fills. This variation is done in order to reduce false asymmetries possibly correlated with the even and odd bunches.

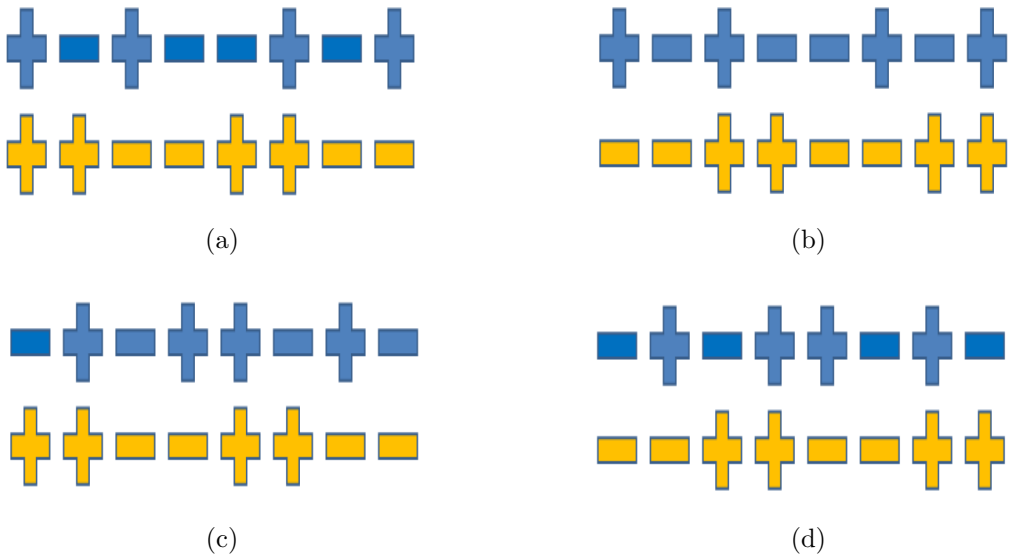

Figure 2.4: Four separate spin patterns of colliding proton bunches used in consecutive fills at RHIC during 2006. Upper rows show spin of proton bunches in the 'blue' ring at RHIC and the lower rows show spin of proton bunches in the 'yellow' ring.

2.1.4 Polarimeters

Several polarimeters at RHIC are used at different stages of the accelerator system in order to check for the depolarizing effects. The measured polarization values are used for various asymmetry measurements as well as to study and improve polarization of the proton beams. RHIC uses two different types of polarimeters (a) proton-carbon (pC) polarimeters that use elastic scattering of polarized protons from thin (thickness = 25 nm) carbon targets and (b) hydrogen-jet polarimeters. Polariza-

tion of the beams are determined by measuring the left-right asymmetries of scattered particles :

$$\begin{aligned} P_{beam} &= \frac{1}{A_N}\left(\frac{N_{right}-N_{left}}{N_{right}+N_{left}}\right), \\ &= \frac{\epsilon}{A_N}, \end{aligned} \tag{2.3}$$

where ϵ is the raw asymmetry and the analyzing power A_N is given by :

$$A_N = \frac{1}{P_{beam}}\left(\frac{N_\uparrow - N_\downarrow}{N_\uparrow + N_\downarrow}\right), \tag{2.4}$$

the subscripts denoting the two possible spin configurations of the polarized beam. The analyzing power is measured from other experiments (in the case of the pC polarimeter) and the from the scattering of the recoil of the target (in case of the H-jet polarimeters).

In the first technique mentioned, the recoil carbons are detected using silicon sensors. At the relevant energy scale, interference occurs between the electromagnetic (QED) and hard (QCD) scattering amplitudes and these method of polarimetry are therefore termed as the Coulomb-Nuclear Interference (CNI) techniques. Each of the RHIC rings and AGS uses a pC polarimeter each for polarization measurements. Polarization measurements by pC polarimeters are very fast ($\sim$ million events every second), however, the analyzing power A_N^{pC} used for these measurements was obtained from the E950 experiment [35] at AGS and it had a large ($\sim 30\%$) uncertainty. The pC polarimeter techniques and measurements are described in detail in [84].

The fast measurements at the pC polarimeters are calibrated by the second type of polarimeters. About 96% polarized hydrogen gas jets are ionized and passed through the beam pipe. The elastic scattering of protons are used to measure recoil protons by silicon strip sensors. In this case however, the analyzing power is measured by using the precisely (within 2%) known values of the target polarization and the asymmetry

of the target scattering ($A_N = \epsilon_{target}/P_{target}$). The same analyzing power is used with the measured beam scattering asymmetry to calculate beam polarization. The measurements by H-Jet polarimeters are slow and it takes several hours to gather enough data points for the required accuracy. More details of this techniques and the H-jet measurements can be found in [85].

2.1.5 Spin Rotator

In the RHIC storage ring, the polarized protons have the spin vector in the vertical direction as it is the stable configuration at RHIC (siberian snakes help reduce depolarization effects with a vertical spin direction). At interaction points however, the experiments require different spin directions (vertical, radial or longitudinal) for various asymmetry measurements. A set of four helical dipole magnets (one each on both sides of the nominal interaction region for each RHIC ring) are used at the IP's for PHENIX and STAR experiments for the purpose of rotating the spin direction of the colliding proton bunches to the desired direction and bringing it back to the stable vertical direction before putting the bunches back in the RHIC rings. Detailed description of the spin rotators can be found in this comprehensive review [34].

2.2 PHENIX Detectors

The PHENIX experiment [22] was designed keeping in view photon, electron and muon measurements with high rate data collection and high resolution of energy/mass measurement and particle identification. In particle physics experiments, the scattering angle with respect to the beam direction is an important quantity and often certain types of interactions of interest produce particles in certain zones of this angle. Pseudo-rapidity ($\eta = \frac{1}{2}\ln(\frac{|\vec{p}|+p_L}{|\vec{p}|-p_L}) = -\ln(\tan\frac{\theta}{2})$), a function of the angle, is used to parameterize experimental results or describe detector designs. The PHENIX detector system consists of two central arm spectrometers at mid-rapidity and two

spectrometers at forward rapidity regions for tracking and identifying muons specifically.

Each of the central arm spectrometers has an acceptance covering a pseudo-rapidity range of $|\eta| \leq 0.35$ and $\delta\phi = 90^\circ$ in azimuth. Central arm detectors are essentially for tracking and identifying charged particles and detection and energy measurements of photons. The tracking system consists of drift chambers (DC) and pad chambers (PC). The ring imaging Cherenkov detector (RICH) and time-of-flight (TOF) provide charged particle identification and the electromagnetic calorimeter (EMCal) provide energy measurements of photons and electrons. PHENIX detectors during the 2006 run at RHIC are shown in Fig. 2.5

2.2.1 Luminosity Detectors

PHENIX uses the two global detectors, a pair of beam beam counter (BBC) and a pair of zero degree calorimeter (ZDC) on both sides of the interaction region [22]. The BBC is used for (a) triggering, (b) determining the event vertex along beam direction and (c) for timing calibrating used in the Time of Flight calculations. Each side of the BBC is composed of 64 photomultiplier tubes (PMT). Each of the one-inch diameter mesh-dynode photomultiplier tubes is equipped with a 3 cm quartz in front of the PMT used as a Cherenkov radiator (Fig. 2.6). Each BBC array is placed 144 cm from the nominal interaction center and about 1 cm from the beam pipe. The BBC array has an inner diameter of ~ 10 cm and outer diameter ~ 30 cm. The BBCs cover a pseudo-rapidity range on $3.0 \leq |\eta| \leq 3.9$ and complete azimuthal coverage. BBC has a timing resolution of 52 ± 4 ps for a single PMT. A laser signal is simultaneously delivered to Time-of-Flight detector, Electro-Magnetic Calorimeter and each individual BBC elements to monitor and calibrate the timing information. A well monitored air flow system is used to cool the BBC system constantly. Timing information for each BBC is calculated as :

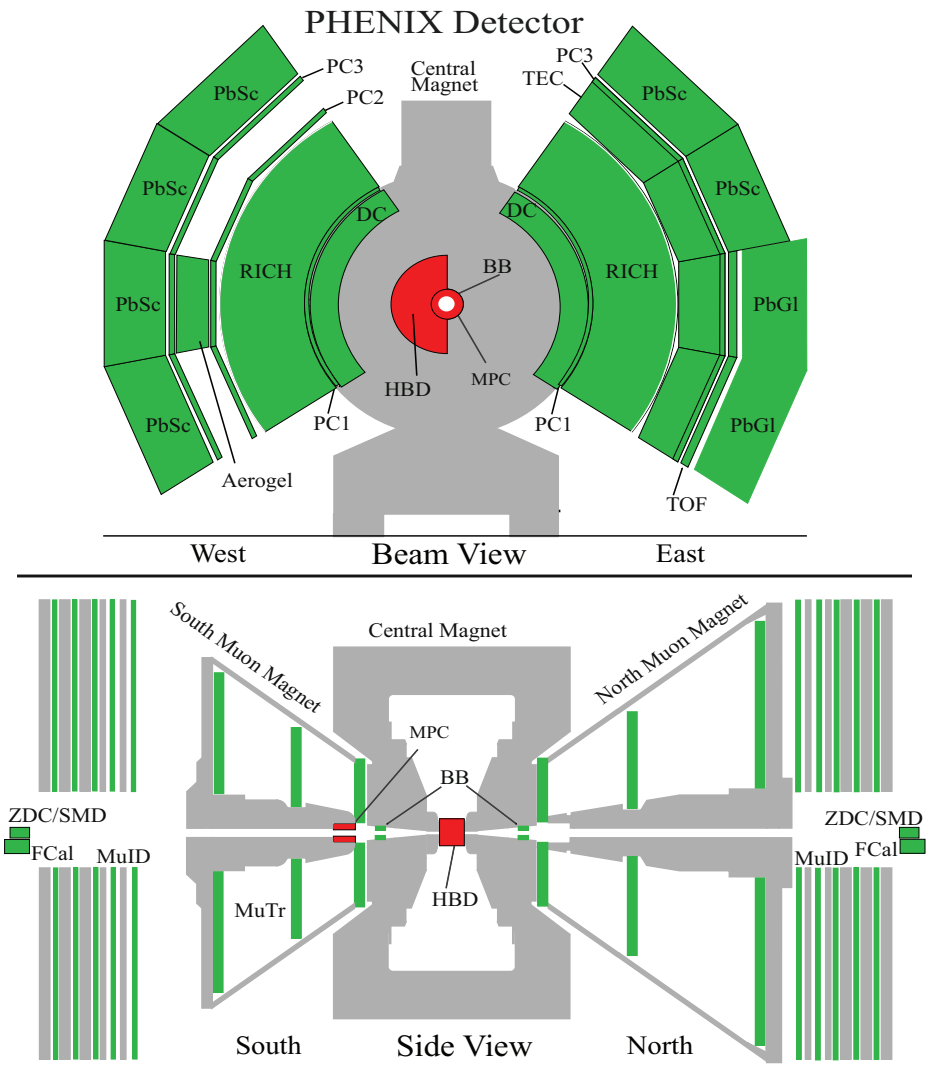

Figure 2.5: PHENIX detector during 2006 data taking period.

$$T_{corr} = T_{raw} - T_{offset} - C/\sqrt{Q}, \tag{2.5}$$

where T_{raw} is the uncorrected arrival time of the signal, T_{offset} is the time offset in each individual BBC element, Q is the measured charge of the signal and C is the coefficient of time walk (determined by minimizing $\delta t_i = T_{N/S} - t_i$ for all BBC elements).

For the dataset used for the present analysis, a BBC local level 1 trigger (minimum bias trigger) was defined as a coincidence of at least one PMT hit on both sides of

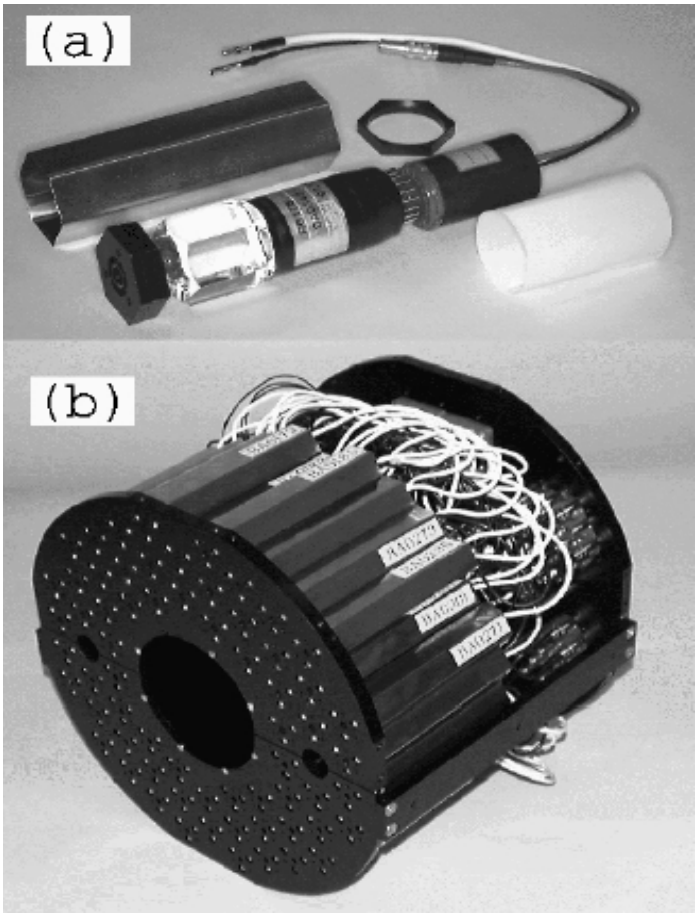

Figure 2.6: (a) Single Beam Beam Counter consisting of mesh-dynode photomultiplier tube on a 3 cm quartz radiator and (b) BBC array comprising 64 units. [38]

the BBC. The hit times of all PMTs on one side is averaged and the average hit time from the two sides are used to calculate the event vertex position z_{vtx} :

$$z_{vtx} = c\left(T_S - T_N\right)/2, \tag{2.6}$$

where c is the velocity of the particles and T_S, T_N are the average hit times in the two sides of the BBC. The time zero t_0 of the collision events used for time-of-flight calculations is given by $t_0 = \left(T_S + T_N\right)/2$. With the given BBC timing resolution, the spatial resolution of z_{vtx} measurement is $\sim$ 5 cm for online measurements and $\sim$ 2 cm for offline measurements. BBC's are used for luminosity counts for the cross

section measurements (counts are normalized by the process cross section seen by the BBC trigger, termed as 'BBC cross section') and for the determination of relative luminosities for asymmetry measurements (using the scaler data of BBC triggered event counts) at PHENIX.

One aspect of averaging hit times from all PMT's in each arm is that BBC is blind to the multiple collision events in a single bunch crossing. This creates a mis-calculated luminosity measurement. For the 2006 run, with the given beam intensities, the multiple collision rates were small $\sim 5\%$ and the effect on relative luminosity measurement is negligible. For later years of data, the effect may be significant for the desired precision of asymmetry measurements ($\sim 10^{-4}$).

ZDC's are hadronic calorimeters used for forward neutron tagging at PHENIX. The ZDC's are located at ± 18 m from the nominal interaction center and cover a cone of 2 mrad with a pseudo-rapidity range of $\eta \geq 6$. ZDC has a timing resolution of ~ 150 ps and resulting spatial resolution for the vertex determination using ZDC is ~ 30 cm. For cross section measurement, ZDC triggered data is used in conjunction with BBC triggered data to properly determine the luminosity normalization constant σ_{BBC} (BBC cross section). The comparison of BBC triggered data in coincidence with ZDC triggered data gives the z-dependence of the triggered events. For asymmetry measurements, ZDC triggered data is used for the comparison of BBC triggered data in order to determine the systematic uncertainty on the relative luminosity R.

2.2.2 PHENIX Magnets

The PHENIX magnet system [43] has three parts made of iron yokes and water-cooled copper coils, the Central Magnet (CM) and north and south Muon Magnets (MMN and MMS). The Central Magnet provides an axially symmetric field around the interaction vertex for the entire azimuth with $\int Bdl = 0.78$ T.m. This field causes the charged particles to bend in a plane perpendicular to the beam axis. The bending

angles, measured at Drift Chamber, provide measurements of particle momenta. For the 2006 run, the ++ configuration was used for the central magnet (Fig. 2.7).

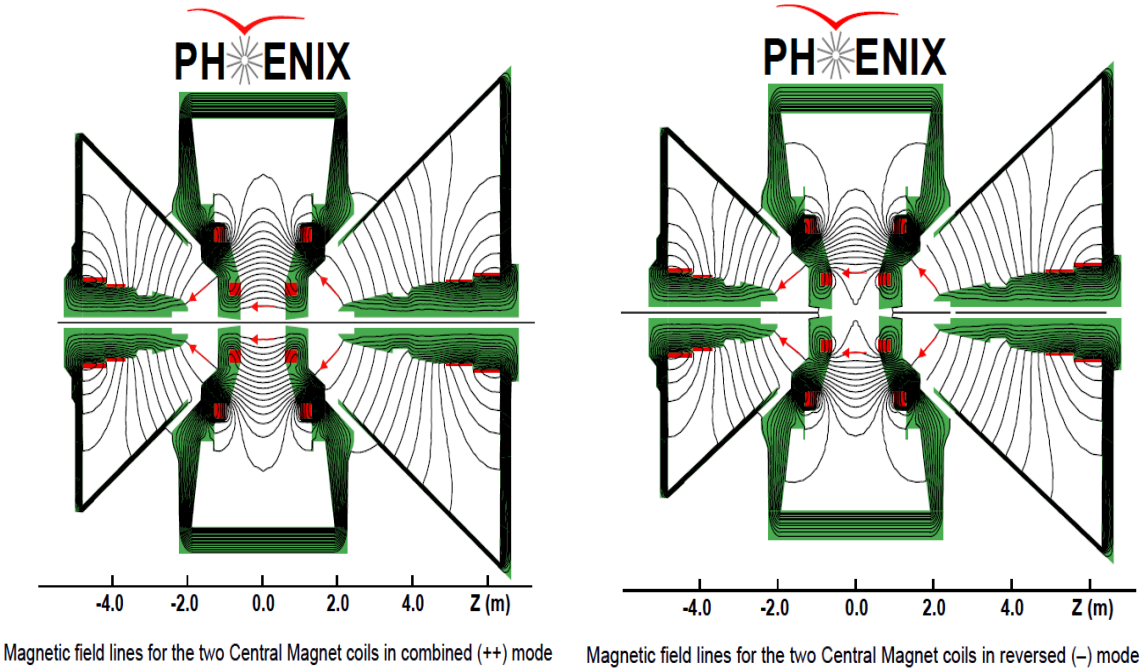

(a) ++ (b) +−

Figure 2.7: PHENIX magnets filed lines with (a) Central Magnet in ++ configuration and (b) Central Magnet in +− configuration.

2.2.3 Tracking Detectors

Outside the axial field of the PHENIX central magnet, each central arm has a DC and layers of PC that are used for tracking charged particles [22, 21]. The PHENIX DCs are cylindrically shaped and located in the region from 2 m to 2.4 m from the beam axis z and 2 m wide along z. Each drift chamber measures the charged particle tracks in the azimuthal $(r-\phi)$ direction and determine its transverse momentum p_T. The transverse momenta, along with the polar angle θ information from the $PC1$ hits, are used to calculate the total momentum p.

2.2.3.1 Drift Chambers

The DC system consists of two independent wire chambers filled with a gas mixture (49.7% Ar + 49.7% Ethane + 1%C_2H_5OH) located in the east and west arms. The volume of each detector is confined by a cyndrical titanium frame (Fig. 2.8). Each frame in a single arm is divided in the azimuthal direction into 20 equal sectors of 4.5° each. Each such sector consists of six modeules of wires stacked in radial direction : two sets of wires (X_1, X_2) parallel to the beam direction and two pairs of (U_1, V_1 and U_2, V_2) stereo wire at a 6° angle with respect to the X wires. Each module contains 4 anode planes and 4 cathode planes forming cells of $2-2.5$ cm drift lengths in the ϕ direction. X wires are used for the precise measurements of tracks in the $r-\phi$ plane and the U, V wires are used to measure the z coordinates of the tracks. The stereo angle is chosen by matching the z resolution of the pad chambers to minimize ambiguity of track matching with hits in the DC and PC.

Each of the X cells contain 12 anode wires and each of the U, V cells contain 4 anode wires. The wire configuration in each sector of the DC is shown in Fig. 2.9. The anode wires are separated by Potential wires (P) and surrounded by Gate (G) and Back (B) wires. The P wires form a strong electrical field. The G wires limit the track sample length to ~ 3 mm and help minimizing the time spread of the drifting electrons from a single track. The B wires are at low potential and they terminate most of the drift lines from its side, thereby reducing the left-right ambiguity. The drift chambers are designed to have (a) single wire resolution better than 150 μm in $r-\phi$, (b) single wire two track separation better than 1.5 mm, (c) single wire efficiency 99% and (d) a spatial resolution in the z direction better than 2 mm.

2.2.3.2 Pad Chambers

The pad chambers are multi-wire proportional chambers with a single plane of anode wires inside a gas volume bound by two cathode planes. One of the cathodes

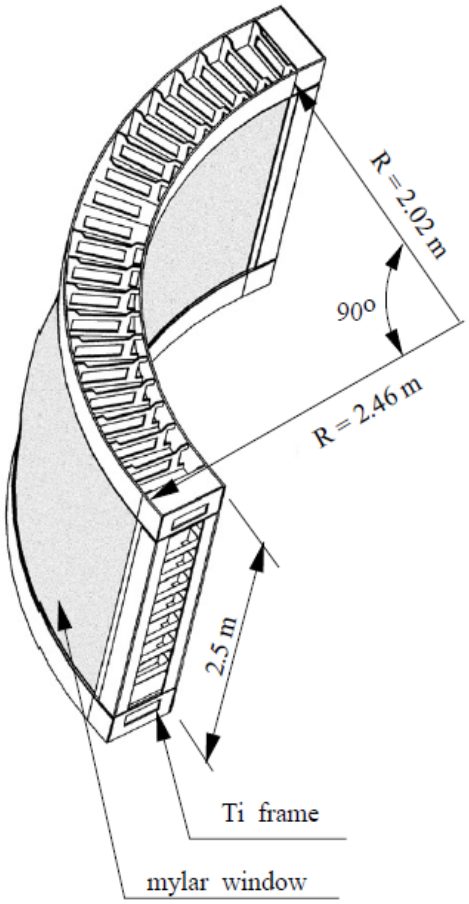

Figure 2.8: Titanium frame defining the DC volume [21].

is a solid plane and the other is segmented into pixels. A cell contains three pixels and an avalanche must be traced by all three pixels to have a valid hit in the cell (Fig. 2.10). An array of 9 connected pixels is named 'pad'. A cell area of 8.4×8.4 mm^2 results in a position resolution of 1.7 mm in the z direction. There are two layers of PC in the east arm and three in the west. To maintain the same angular resolution, further layers of pad chambers have larger cell sizes e.g. cells in PC3 have four times the area of cell in PC1 as PC3 is at twice the distance from beam axis as PC1. PC1 in each arm (East and West) is composed of 8 separate chambers each of size 0.5×2 m^2. Pad chamber hit information is used in conjunction with DC hits to reduce ambiguity in the track reconstruction. Outermost layers of PC are used for

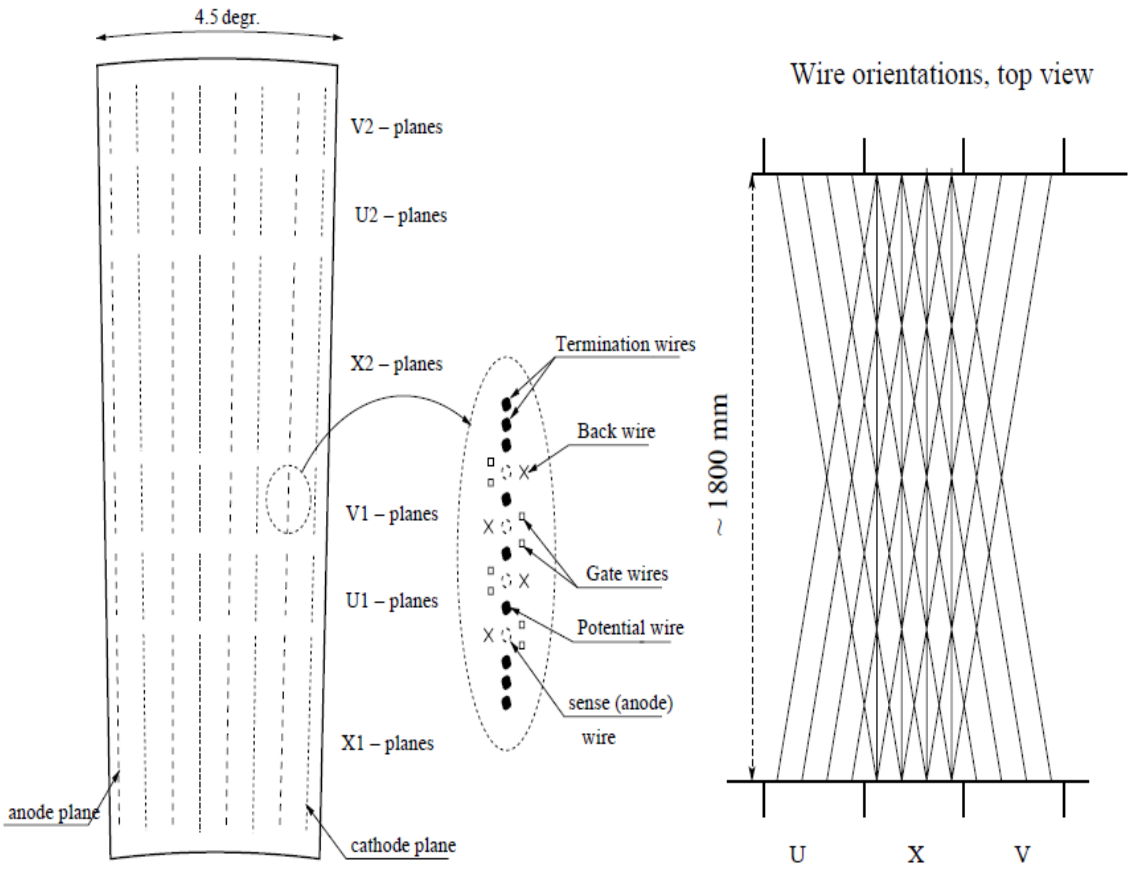

Figure 2.9: Wire configuration in the DC [21].

matching the projected tracks and the method is used to separate backgrounds from charged hadron tracks. More on the track reconstruction at PHENIX using DC and PC is discussed in Sect. 3.1 in the following chapter.

2.2.4 Cherenkov Detectors

Placed after the DC and PC, a ring imaging Cherenkov (or Cherenkov) detector (RICH) [33] is used for electron identification. The RICH uses CO_2 at atmospheric pressure as a radiator, with a momentum threshold of 17 MeV/c for $e^{\pm}$. It is primarily used for identifying $e^{\pm}$. Pion threshold for firing RICH is 4.65 GeV/c and in conjunction with the EMCal, it provides e/π separation.

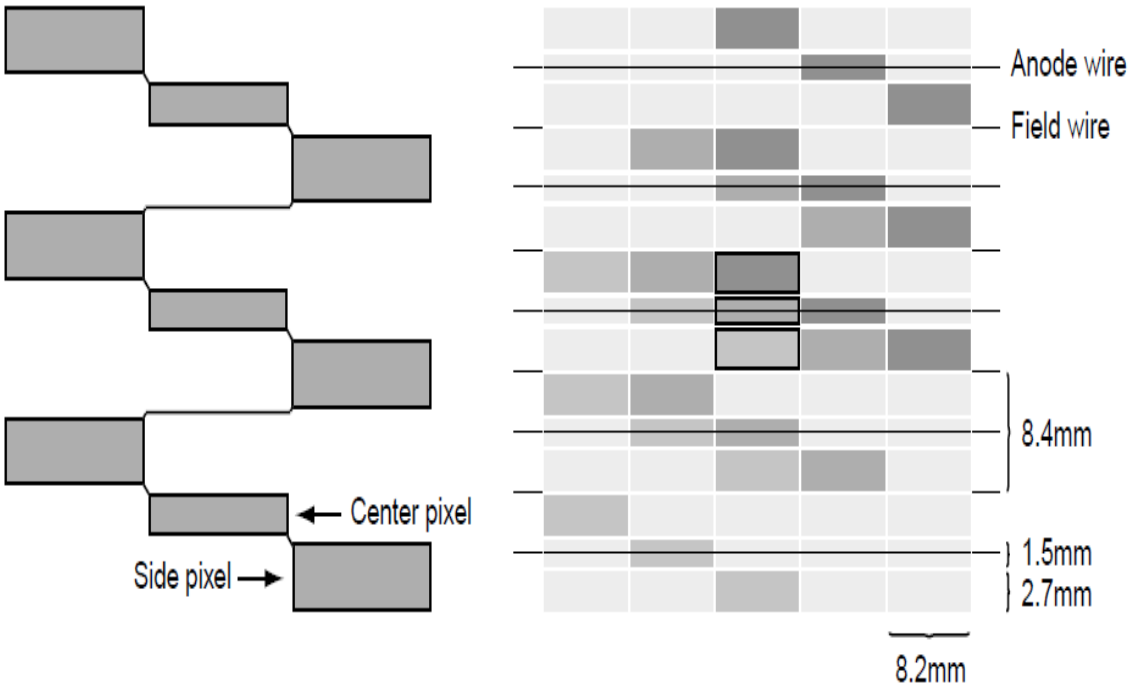

Figure 2.10: The pad and pixel configuration (left). A cell is defined by three pixels (right). [21]

The Hadron Blind Detector (HBD, commissioned for one Arm only for the 2006 run) is a windowless triple gas electron multiplier (GEM) Cherenkov detector [33]. It uses CF_4 as the radiator gas with the pion threshold ~ 4 GeV/c. The HBD is placed near the beam pipe ($50 - 60$ cm) in the magnetic field free region. It uses a reverse bias (voltage) to repel ionization from hadrons below the threshold ('hadron blind') and is sensitive to photo-electrons from Cherenkov light only.

2.2.5 Particle ID Detectors

TOF detector uses the time of flight of particles from the collision vertex to the detector in conjunction with the reconstructed track information to identify charged particles. The detector had a small acceptance in 2006 (almost one-fourth of the Central Arms). A description can be found in [33]. Time Expansion Chamber (TEC)

and Aerogel (small acceptance) are PID detectors that use energy loss ($-\frac{dE}{dx}$) of particles in the material to identify charged particles.

2.2.6 Electromagnetic Calorimeter

The outermost component of the central arm spectrometers is the electromagnetic calorimeter, located at $r \sim 5$ m. It provides energy and position measurements of $e^{\pm}$ and photons and also timing information. In the west arm, the calorimeter has four sectors of lead-scintillator (PbSc) sampling calorimeters and in the east arm, two sectors of PbSc along with two sectors of lead-glass (PbGl) Cherenkov calorimeters. Each sector covers $|\eta| \leq 0.35$ and $\delta\phi = 22.5°$. The PbSc sectors have energy resolution of $\sigma_E/E = 2.1\% \oplus 8.1\%/\sqrt{E}$ and timing resolution ~ 300 ps. The PbGl sectors have energy resolution of $\sigma_E/E = 0.8\% \oplus 5.9\%/\sqrt{E}$ and timing resolution ~ 200 ps. A more detailed description of the detector can found in [42].

2.2.7 Muon Arm Detectors

In the forward rapidity region the PHENIX Muon Arm [22] consists of Muon Trackers (MuTr) and Muon-Identifier (MuID) Detectors. They cover an azimuth of 180 degrees and the pseudo-rapidity coverage is $-2.25 < \eta < -1.15$ for the south arm and $1.15 < \eta < 2.44$ for the north arm.

2.2.8 Drift Chamber Quality Analysis

Minimum bias triggered data was used to perform quality analysis of the DC. For four quadrants of the detector (two sides of the nominal interaction center for each of the East and West arms), track counts are plotted as a function of the variable 'board' (signifying 20 sectors of the DC) defined as :

$$\text{board}_{East} = \frac{3.72402 - \phi + 0.008047 \times \cos\phi + 0.87851}{0.01963496} \quad (2.7)$$

$$\text{board}_{West} = \frac{0.573231 + \phi - 0.0046 \times \cos\phi + 0.05721}{0.01963496}. \quad (2.8)$$

Tracks are selected with similar requirements as for the final analysis (as discussed in detail in Sect. 3.1). Events with vertices within 30 cm of the nominal interaction center are selected. Best quality tracks are chosen with a matching window of 3σ in the PC3dϕ, PC3dz and variables for $p_T > 0.2$ GeV/c.

Tracks are plotted in the α-board (α being the bending angle of tracks in the DC) plane and dead or low-occupancy segments are determined as a function of bending angle in DC α and *board* and are rejected for final comparisons (Figures 2.11, 2.12). A run with the fewer problems and high performance is selected as a reference. The ratio (r) of the number of tracks to the number of minimum-bias events is determined for every run (segments of data taking period tagged with a number) and is compared to the reference run across the 80 boards (4 quadrants each with 20 sectors/boards). The ratio of the aforementioned quantity r for any run to that of the reference run across the 80 boards are fitted with a constant value (sample plots : Figures. 2.13 and 2.14). The presence of the spikes in the ratio (w.r.t reference run) vs. board plots indicate hot/faulty wires in DC. Presence of a few such bad wires can change the fit quality (chi-square) and such run is rejected for analysis eventually after the QA. The values of the constant parameter and the χ^2 are used to determine any run with abnormal performance and they are rejected for the final analysis.

During the 2006 RHIC run, a large segment of the drift chamber in the west arm was unavailable for data taking due to some dead/torn wires as can be seen in Fig. 2.12, resulting in a low performance ($< 50\%$) in the West arm and significant loss of statistics. The segments were mended for the runs in the subsequest years.

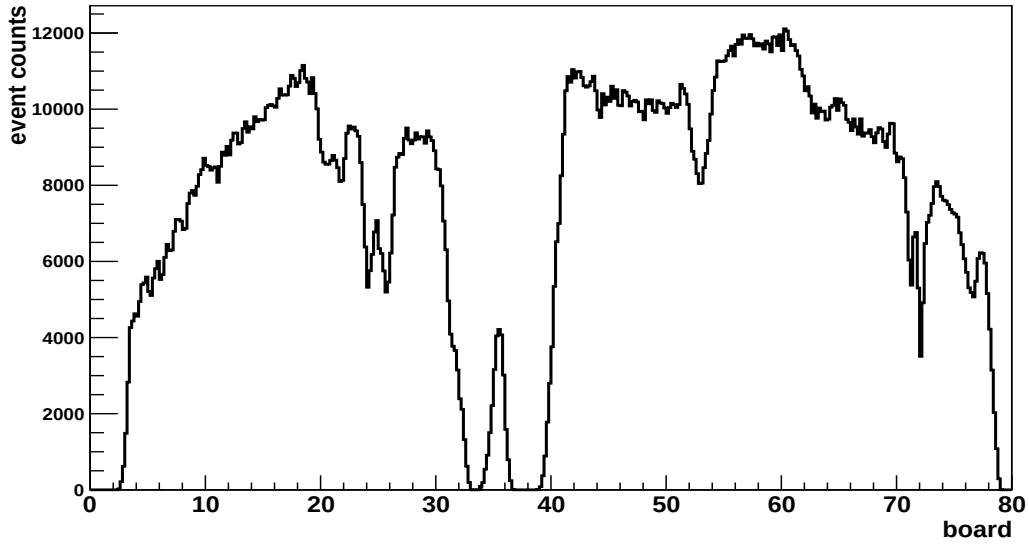

Figure 2.11: Selected tracks as a function of board for the one half of the detector in the East arm.

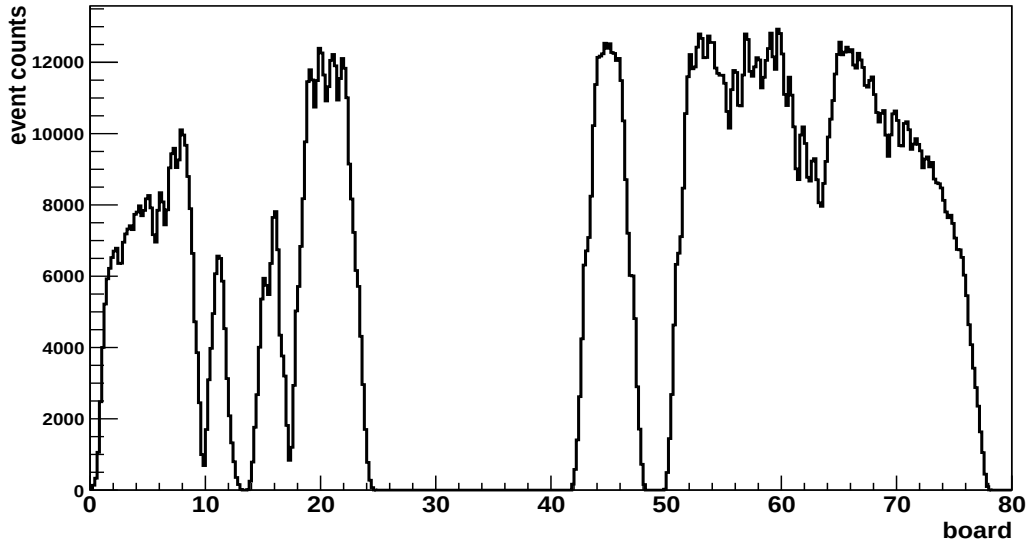

Figure 2.12: Selected tracks as a function of board for the one half of the detector in the West arm.

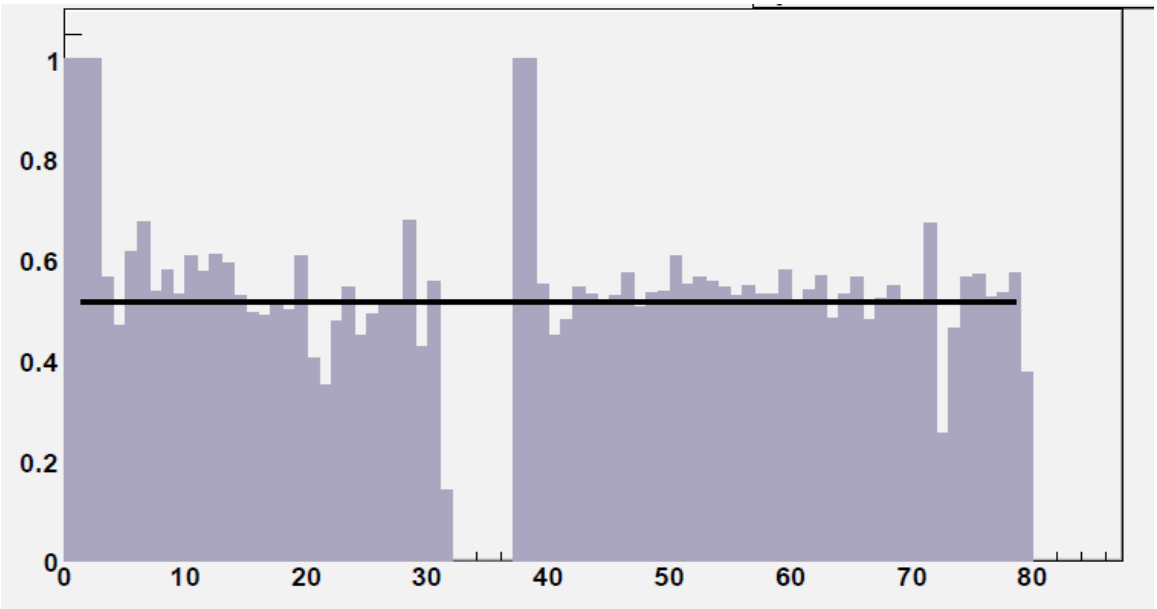

Figure 2.13: Ratio of normalized (by number of minimum bias events) tracks as a function of board for the one half of the detector in the East arm.

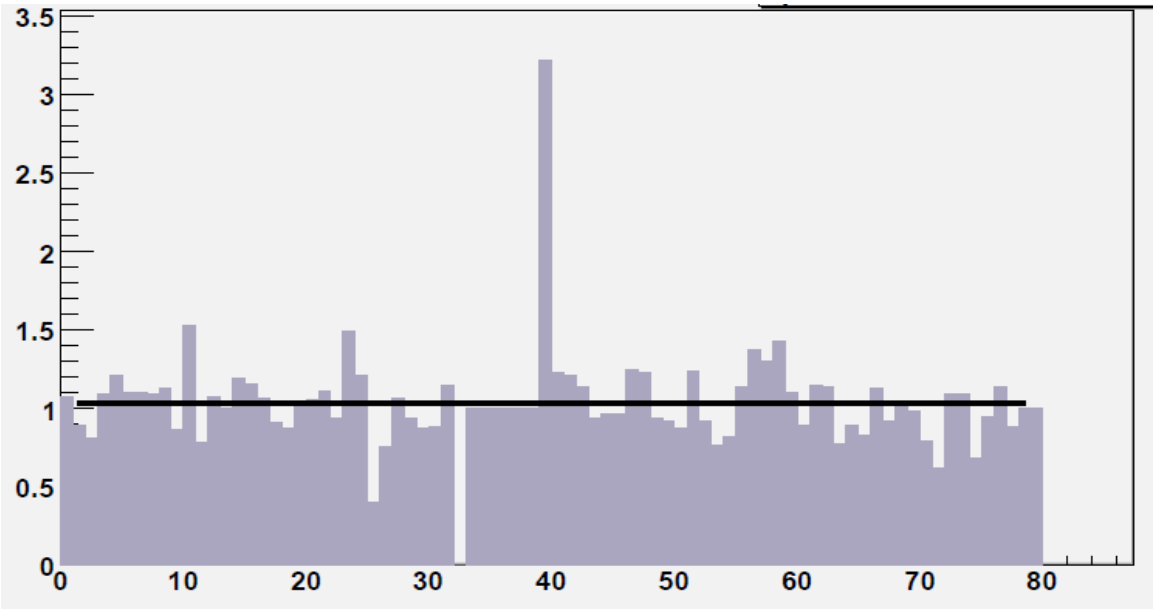

Figure 2.14: Ratio of normalized (by number of minimum bias events) tracks as a function of board for the one half of the detector in the West arm.

CHAPTER 3

DATA SELECTION, HADRON TRACK CRITERIA AND BACKGROUNDS

3.1 Data Set

We analyzed proton-proton collision data taken at RHIC during 2006. In 2006, RHIC operated with two different beam energies of 100 and 32.2 GeV (center of mass energies of 200 and 64.4 GeV). The ten days of 62.4 GeV data were only a small subset of the entire data from 2006. We analyzed data corresponding to an integrated luminosity of 15.6 nb^{-1} ($\sim$ 214 Million events, including both transverse and longitudinal polarization) for cross section measurement and 11.9 nb^{-1} ($\sim$ 163 Million events, longitudinally polarized) for asymmetry measurement. Analyzed events were triggered by requiring the coincidence of at least one photo-tube hit on both sides of the BBC (Minimum Bias trigger). This particular choice of trigger avoids the bias of detection (introduced by the detectors associated with the triggers) towards different hadron species. Event vertices were determined by using the differences of average hit times in the north and south end of the BBC. For these analyses, event vertices were chosen to be within 30 cm of the nominal interaction center to avoid collision of particles with the Central Magnet.

From a $p + p$ scattering event in the collision of a pair of proton bunches at the interaction region, particles spread in different directions. For the hard processes that we are interested in, we looked for the final state particles with high enough transverse momentum and going to the PHENIX Central Arm detectors. DC and PC1 in Central Arms, in conjunction with the event vertex information, are used

to reconstruct charged tracks. Track reconstruction is done separately in the bend plane ($r-\phi$ plane) (Fig. 3.1) and the non-bend plane ($r-z$ plane) (Fig. 3.2). In the $r-\phi$ plane, reconstruction is done using the 'Combinatorial Hough Transform' technique in which any pair of hits can be mapped to a point in a space defined by the azimuthal angle ϕ and track bending angle α. Assuming tracks are straight lines within DC (negligible residual magnetic field after DC), all hit pairs associated with a track should have the same (ϕ, α) and the mapping therefore will form a local maxima in the $\phi-\alpha$ phase space. Reconstruction in the bend plane determines the ϕ and α of the tracks. The momentum of the charged particle is then calculated using the bending angle α of the track measured in DC.

$$\alpha \simeq \frac{K_1}{p}, \tag{3.1}$$

where K_1 is the magnetic field integral ~ 101 mrad GeV/c. Using this initial estimate of the momentum, the final value is calculated from a pre-determined four dimensional grid $f(p, r, \theta_0, z_{vtx})$, where p is the initial estimate, r is the radius at which the field integral is calculated, θ_0 is the polar angle of the track at the vertex and z_{vtx} is the vertex position along the beam direction.

After the bend-plane, reconstruction is done in the non-bend plane. PC1 hit position and event vertex z_{vtx} determined by BBC were used to determine the direction of the track and DC wire hits are associated with the track within a ± 5 cm window. For more than one possible PC1 hit, the number of DC hits are maximized to determine the unique choice. The polar angle θ is determined from the reconstruction in the $r-z$ plane.

3.1.1 Beam-Shift Calibration

In the tracking algorithm, the momentum of a particle is estimated from the bending angle α (deviation of the track from an infinite momentum track from same vertex

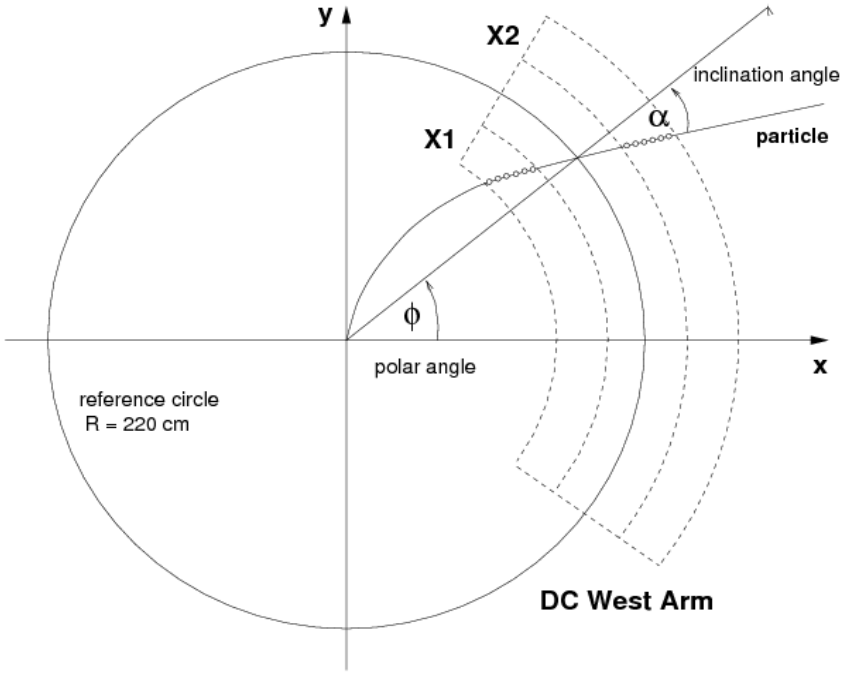

Figure 3.1: Track reconstruction in the bend (azimuthal) plane at PHENIX.

and hitting the same point at the reference radius in Drift Chamber) as described in Sect. 3.1. Measurement of the bending angle is sensitive to the precise calibration of the position of the DC and the beam. If there is a shift of the beam or the DC arms relative to the coordinate system, the measurement of angle α acquires an offset:

$$\delta\alpha = \frac{\delta X \times \sin\phi}{R_{DC}} + \frac{\delta Y \times \cos\phi}{R_{DC}}, \tag{3.2}$$

where ϕ is the azimuthal angle and R_{DC} is the reference radius in DC (220 cm from ideal beam axis). This offset in angle is translated as an offset in the measured momenta of the tracks. Using the time of flight (T) of particles to the east arm of the high resolution Time of Flight (TOF) detector in conjunction with the path length (L) and the momentum (p) from the reconstruction model, the squared mass (m^2) of the particles are calculated.

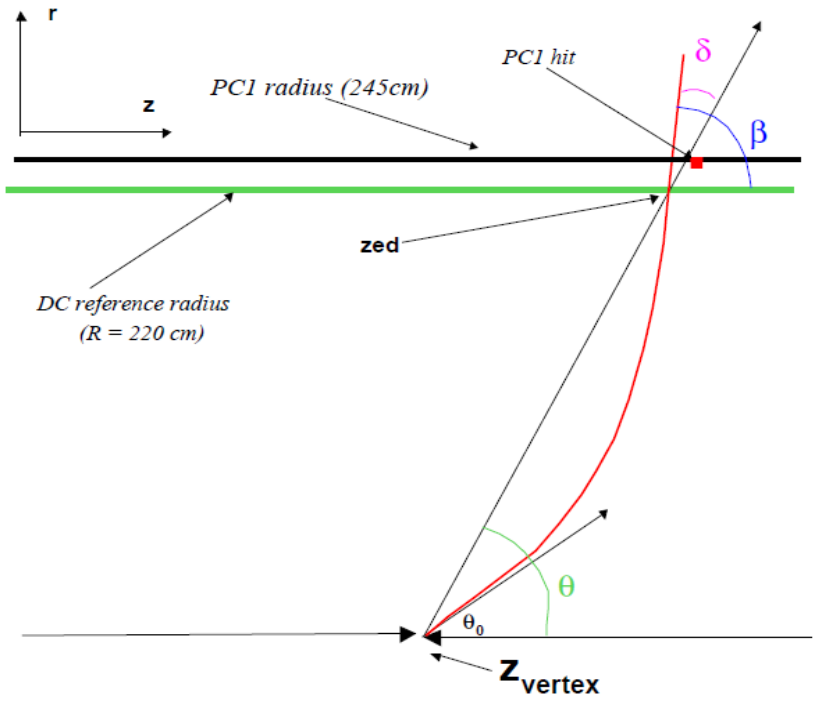

Figure 3.2: Track reconstruction in the non-bend plane at PHENIX.

$$m^2 = p^2 \left(\frac{cT}{L}^2 + 1 \right). \tag{3.3}$$

In the mass-squared distribution of protons, a splitting is observed between protons and antiprotons. This arises because the momentum shift due to the offset in the bending angle ($\delta\alpha$) affects different charged particles in different ways (increasing measured momentum of one charge while decreasing the measured momentum of the other). To extract the magnitude of the shifts (of beam or DC), parameters in Eq. 3.2 are varied to match the proton and anti-proton mass-square peaks. We estimated an x-offset of 0.1 cm in the East Arm, an x-offset of -0.28 cm in the West Arm and a y-offset of 0.2 cm. The proton (and/or antiproton) squared mass peak values are compared to the standard particle data group accepted value (0.88 GeV^2/c^2) to extract the 'momentum scale correction factor'. The scale factor was determined to be

1.01 with 1% uncertainty. All reconstructed momentum measurements were corrected for the beam offsets and were scaled appropriately to obtain final momentum values.

3.1.2 Selection Criteria

Along with the trigger choice and event vertex cut, several other conditions were applied to the reconstructed track variables to select final state hadrons generated from the $p + p$ collisions. After the reconstruction, tracks are projected on PC3 and the distribution of actual hits in the detector around the projected hits are matched. The deviations of actual hits from the projected positions in the $\phi - z$ plane are called matching variables. We impose selection cuts on the distribution of matching variables 'PC3dϕ' (sample plot in Fig. 3.3) and 'PC3dz' (sample plot in Fig. 3.4) in order to select the hadrons produced from the collision event ('signal'). Hadron track selection criteria used for the analysis are listed below. We require tracks with

- an offline cut of 30 cm on the measured vertex position on both sides of the interaction center to make sure that tracks do not collide with the central magnets and produce secondary debris from conversions.
- transverse momentum range $0.5 \leq p_T \leq 4.5$ GeV/c,
- $-75 \leq$ zed ≤ 75 cm, where 'zed' is the hit position along beam direction in DC reference radius 2.2 m.
- RICH veto (to eliminate electron tracks) as pions, the lightest hadron in the mix, fires RICH at $p_T = 4.7$ GeV/c and electrons fire RICH at $p_T \sim 17$ MeV/c, therefore a requirement that RICH does not fire ('veto') eliminates e^+, e^- background tracks.
- track 'quality' = 63 and 31, where 'quality' is a parameter from track reconstruction algorithm denoting roughly how many and how well different detector

hits (DC and PC) are aligned with a track. The values used are the two best possible quality values.

- simultaneous matching window of 2σ in 'PC3dϕ' (azimuth) and 'PC3dz' (beam direction) selecting the signal peak.

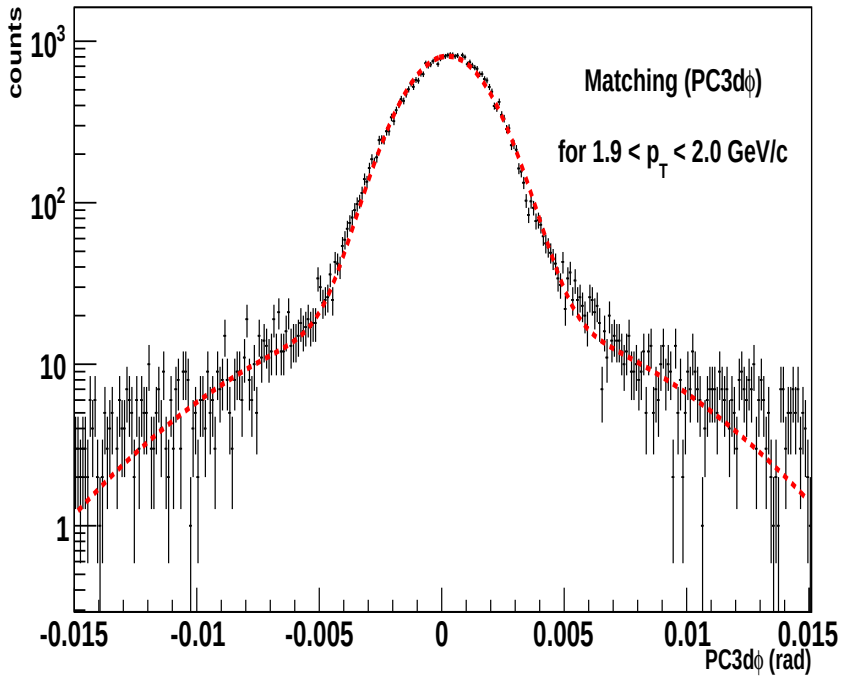

Figure 3.3: Sample matching distribution of 'PC3dϕ' in a p_T bin fitted with two Gaussian functions.

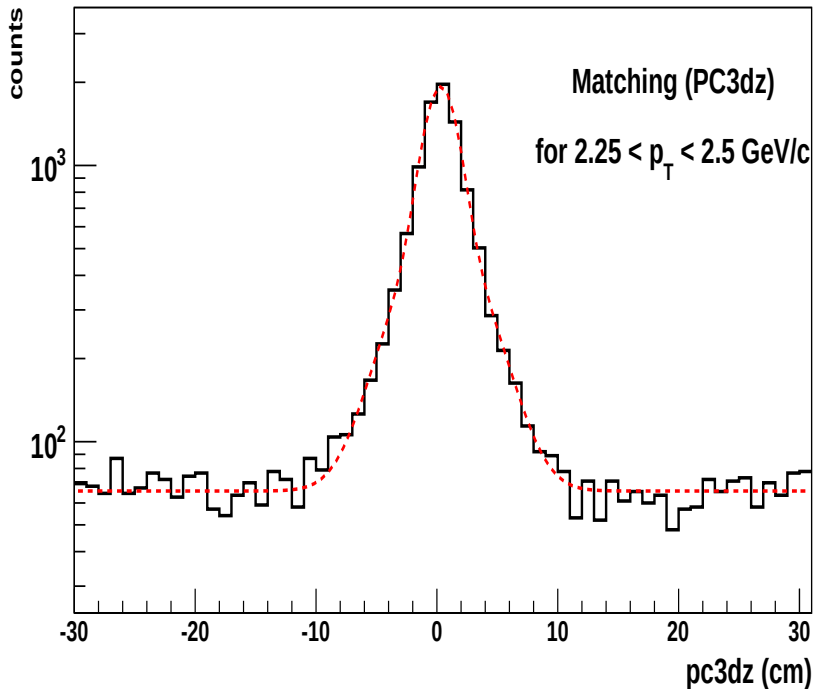

Figure 3.4: Sample matching distribution of 'PC3dz' in a p_T bin fitted with two Gaussian functions and a flat component.

3.2 Backgrounds

A substantial part of the possible backgrounds for the charged hadron tracks are the electron and positron tracks (both directly from the vertex as well as from conversion of photons) and they are eliminated very efficiently by the RICH veto as electrons (and positrons) trigger RICH with very high efficiency(effectively 100%) above $p_T > 17$ MeV/c whereas pion - the lightest hadrons in the mix - fires RICH at $p_T > 4.7$ GeV/c. Another important source of the backgrounds is the weak decays of the hadrons in flight.

Hadron decay backgrounds can be essentially categorized into two different groups:

- Backgrounds from the decays of short-lived particles : K^0_s, Λ (and heavier hyperons) etc.
- Backgrounds from the decays of long-lived particles : $\pi^{\pm}$, $K^{\pm}$, K^0_l etc.

3.2.0.1 Long-lived Particle Decay

The largest contribution to the backgrounds comes from this category. These particles have comparatively longer lifetimes ($c\tau \sim 1$ m) and they decay further from the vertex and close to DC (e.g. conversions at the DC entrance window). Decay products with significantly smaller mass than the parent get a relatively large momentum kick and are spread over a wider range in the matching variables than undecayed signal tracks. These are frequently mis-reconstructed as high-pT tracks. In ϕ, the bending of the decay products in the residual magnetic field produce a smeared double peaked distribution (positive particles on one side, negative on the other) and in 'z', the distribution is mostly flat. Major constituents of these backgrounds are muons (mostly from pion and kaon decays) and pions (mostly from kaon decays).

3.2.0.2 Short-lived Particle Decay

A second source of background is the feed-down backgrounds produced by weak decays of mostly Λ particles close to the event vertex with apparent momenta close to their true momenta and matching distributions peaked under the signal. These particles have smaller lifetimes ($c\tau \sim 1$ cm or less) and therefore decay very close to the vertex. Decay particles travel through most of the magnetic field. In 'z', they have $\sim 50\%$ wider distribution than primary particles, due to kicks from decay and are mostly peaked (under the signal) in ϕ. Major constituents for these backgrounds are the feeddown protons and antiprotons from decays of Λ and heavier hyperons.

3.2.0.3 Treatment of Backgrounds

One possible method of determining the contribution of backgrounds is to look into the distribution of matching variables. For the long-lived particle decay, we can estimate the fraction of background tracks using either 'PC3dϕ' or 'PC3dz'.

Using 'PC3dϕ', the ratio of tracks within selection window (within $\pm 2\sigma$) to those in the tail end (within 3σ-9σ) on one side (positive side for negative particles and negative side for positive particles) in the high $p_T > 6$ GeVc bin (where mis-reconstructed background tracks dominate the distribution) is calculated. This ratio is used to normalize the the analogous ratio in all the relevant p_T bins. Put in a concise form, it gives us $BG/S+BG$ within the selection window ($\pm 2\sigma$) in matching variables for signals :

$$\frac{BG}{S+BG} = \left(\frac{3\sigma \leq \text{tracks} \leq 9\sigma}{\text{tracks} < \pm 2\sigma}\right)_{p_T} \times \left(\frac{\text{tracks} < \pm 2\sigma}{3\sigma \leq \text{tracks} \leq 9\sigma}\right)_{\text{high}p_T} \tag{3.4}$$

Using 'PC3dz' we can extract the background fraction in any p_T bin by normalizing the background tracks within 5σ-15σ on both sides of the mean of the distribution

with the ratio of area under the $\pm 2\sigma$ zone to the total area of 5σ-15σ zone on both sides since the distribution is essentially flat. In a concise form:

$$\frac{BG}{S+BG} = \frac{2(5\sigma \leq \text{tracks} \leq 15\sigma)}{5(\text{tracks} < \pm 2\sigma)}. \tag{3.5}$$

The background fraction from both variables are found to be quite similar and the average of the two background fractions is used as the value for the analysis. The difference between the two sets of values is used as the systematic uncertainty on the background fraction. The measured background fractions are tabulated below (3.1). These backgrounds are subtracted from the total detected tracks.

Feed-down contributions to the detected protons and antiprotons from weak decays of Λ's and heavier hyperons are estimated using input Λ and $\overline{\Lambda}$ spectra from $p+p$ measurements at $\sqrt{s} = 63$ GeV at ISR [40, 64] and at $\sqrt{s} = 62.4$ GeV at PHENIX with the GEANT3 [51] based simulation of the PHENIX detector. The fractional contributions of the feed-down protons and antiprotons are independent of p_T above $p_T = 2$ GeV/c and are close to 7 and 15% respectively. Below $p_T = 2$ GeV/c the fractions increase with decreasing p_T and are roughly 25 and 60% for protons and anti-protons respectively at $p_T = 0.5$ GeV/c. Cross sections are corrected for the feed-down backgrounds. For double helicity asymmetry measurements, however, these background tracks fall under the signal peak in the distributions of matching variables and cannot be separated and no knowledge of the asymmetries of these backgrounds is available. For this reason, these category of backgrounds ($\sim 1-2\%$) are not subtracted or corrected for in the asymmetry measurement presented here.

3.3 Hadron Species Fractions

Non-identified charged hadrons from $p+p$ at $\sqrt{s} = 62.4$ GeV/c consist mostly of pions, kaons and protons and their anti-particles. For the purpose of applying several

p_T Bin	Background fraction (h^+)	Systematic error (h^+)	Background fraction (h^-)	Systematic error (h^-)
0.50-0.60	0.05	0.03	0.01	0.03
0.60-0.70	0.04	0.02	0.01	0.03
0.70-0.80	0.04	0.02	0.01	0.03
0.80-0.90	0.03	0.02	0.01	0.03
0.90-1.00	0.03	0.01	0.01	0.02
1.00-1.10	0.03	0.01	0.01	0.02
1.10-1.20	0.03	0.01	0.01	0.02
1.20-1.30	0.03	0.01	0.01	0.02
1.30-1.40	0.03	0.01	0.01	0.01
1.40-1.50	0.03	0.01	0.01	0.01
1.50-1.60	0.03	0.01	0.01	0.01
1.60-1.70	0.03	0.01	0.01	0.01
1.70-1.80	0.03	0.01	0.01	0.01
1.80-1.90	0.03	0.01	0.02	0.01
1.90-2.00	0.03	0.01	0.02	0.01
2.00-2.25	0.03	0.01	0.03	0.01
2.25-2.50	0.04	0.01	0.03	0.01
2.50-2.75	0.05	0.01	0.04	0.01
2.75-3.00	0.06	0.01	0.06	0.02
3.00-3.25	0.09	0.01	0.09	0.02
3.25-3.50	0.11	0.03	0.11	0.02
3.50-3.75	0.17	0.01	0.17	0.03
3.75-4.00	0.22	0.03	0.23	0.02
4.00-4.50	0.34	0.02	0.31	0.11

Table 3.1: Background fractions for positive and negative hadrons in different p_T bins.

species-dependent correction factors for our measurements, we need to understand the relative contribution of different species in the hadron mix. The production fractions were determined from identified hadron spectra from PHENIX [20] at $\sqrt{s} = 62.4$ GeV/c as well as earlier data from the ISR [40] at $\sqrt{s} = 52.8$ GeV/c and $\sqrt{s} = 63$ GeV/c. We fit each the particle fractions as a function of p_T with the function $(Ae^{Bp_T} + C)$ with the constraint that the sum of fractions of all particles(antiparticles) is 1 using mostly PHENIX data at low pT and ISR data at high pT. For particles, a compensating linear term (Dp_T) is added to the kaon fraction fit and subtracted

from the proton fit. For antiparticles, a similar compensating term is added to the negative pion fit and subtracted from the anti-proton fit. The species fractions and the functional fits are shown in Figures 3.5 and 3.6.

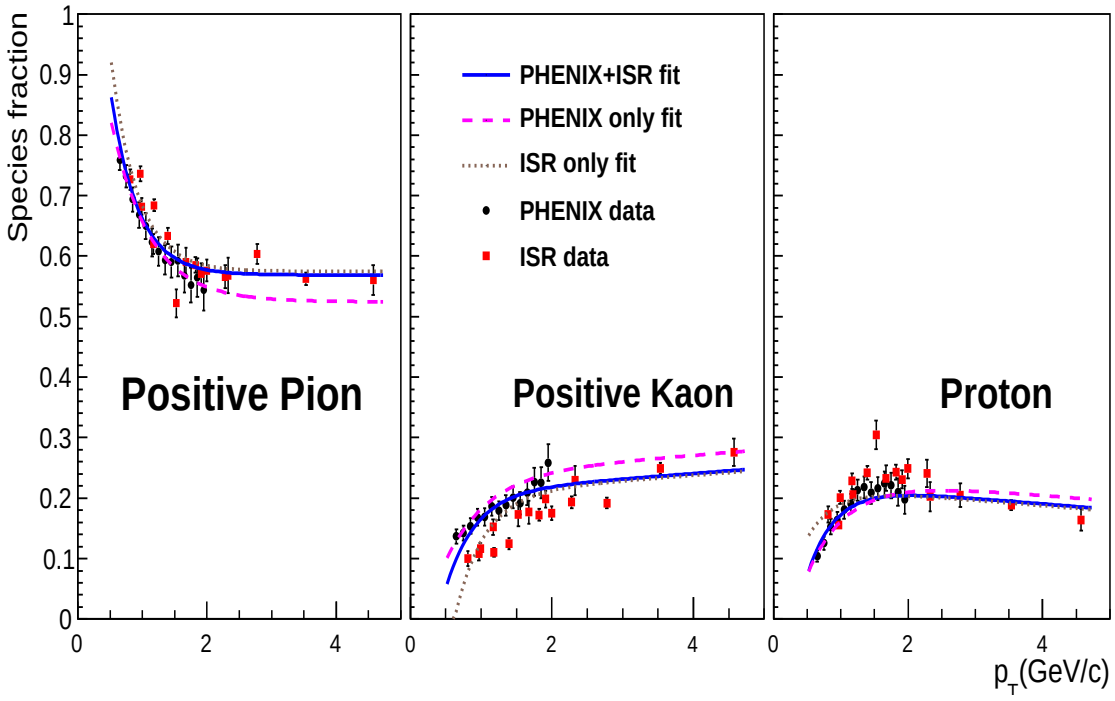

Figure 3.5: Relative fraction of each species for positive hadrons.

Data from PHENIX identified measurement provide data points at the lower end of the p_T range. The limitations of pion-kaon separation effectively restricts the upper end of the spectrum at ~ 2 GeV/c. ISR data provide data for the higher end of the p_T range. But comparison at the lower p_T range indicates a normalization difference between the two data sets. We, therefore use the difference of cross sections measured using species fractions from separate data sets as the systematic error on the measurement of cross sections arising from the determination of the production fraction of individual hadron species. The fit parameters (Table 3.2) are determined within a few percent. Relative fractions from fit values are used to apply the corrections.

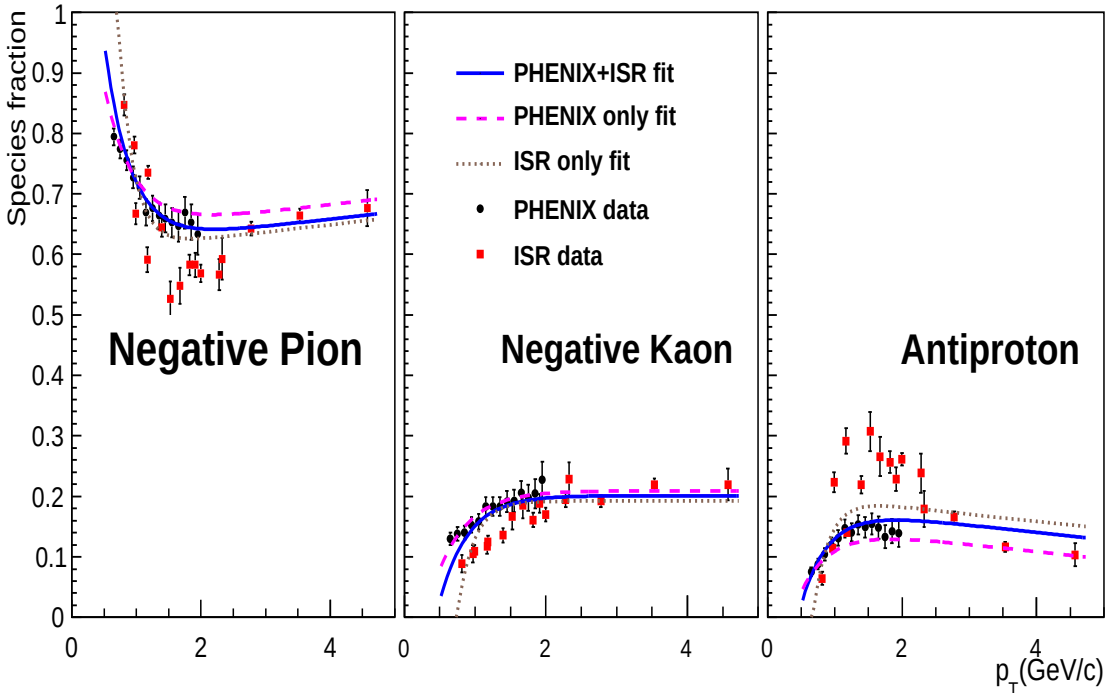

Figure 3.6: Relative fraction of each species for negative hadrons.

hadron	A	B	C	D
π^+	1.02	-2.39	0.57	-
K^+	-0.53	-2.39	0.20	0.009
p	-0.49	-2.39	0.23	-0.009
π^-	1.17	-2.49	0.61	0.012
K^-	-0.61	-2.49	0.20	-
p^-	-0.56	-2.49	0.18	-0.012

Table 3.2: Parameters of the fit $(Ae^{Bp_T} + C)$ to the relative fractions of different species in the hadron mixture. See text for details.

CHAPTER 4

CROSS SECTION MEASUREMENT

The cross sections of the non-identified inclusive charged hadron production presented here is the first such measurement for $p+p$ collisions at center of mass energy of 62.4 GeV. We describe here in detail the methodology of the measurements and compare perturbative QCD calculations to our results. The comparison is a test of our understanding of the physics behind the process and it substantiates the framework we have used to understand the asymmetry results. The cross section is measured using the following formula :

$$\frac{E}{c}\frac{d^3\sigma}{dp^3} = \frac{\sigma_{\rm BBC}}{N_{\rm BBC}}\frac{d^3N(p_T)}{d\phi p_T dp_T dy}C_{\rm eff}^{\rm acc}R_{\rm smear}C_{\rm trig}. \tag{4.1}$$

Here $\sigma_{\rm BBC}$ is the $p+p$ cross section seen by the BBC as measured in [15], $N_{\rm BBC}$ is the total number of BBC triggered events analyzed, p_T is the mean transverse momentum in each bin, N is the number of charged hadrons in the p_T bin, dy is the rapidity range, dp_T is the width of the p_T bin, $C_{\rm eff}^{\rm acc}$ is the combined correction factor for geometrical acceptance of the detectors and efficiency of selection criteria, $R_{\rm smear}$ is the correction factor for the smearing of track p_T owing to the momentum resolution of the detectors as well as multiple scattering of the hadron tracks and $C_{\rm trig}$ is the correction factor for BBC trigger bias.

4.0.1 Luminosity Normalization and Vernier Scan

The parameter σ_{BBC} is the part of the total process cross section available to the BBC trigger (minimum bias trigger). It is estimated using various beam parameter

information (intensity of colliding bunches, frequency of collisions) and measurements of transverse widths of the beams using the Vernier scan (Van der Meer scan) technique. For the data set discussed here, the measurements were done at PHENIX as part of the neutral pion cross section and asymmetry measurements and discussed in detail in [15]. The σ_{BBC} is defined as :

$$\sigma_{BBC} = \frac{R^{BBC}_{max}}{\mathcal{L}_{machine}\epsilon_{BBC}}, \tag{4.2}$$

where R^{BBC}_{max} is the BBC triggered event rate at the maximal overlap of two beams, ϵ is the efficiency of the BBC trigger (fraction of the collisions that falls within the vertex region $|z_{vtx}| < 30$ cm available to the trigger) and the delivered machine luminosity $\mathcal{L}_{machine}$ is defined as :

$$\mathcal{L}_{machine} = f\frac{N_B N_Y}{2\pi\sigma_x\sigma_y}, \tag{4.3}$$

where f is frequency of revolution ($\sim$ 78 kHz) of proton bunches, N_B, N_Y are the intensity of two beams and σ_x, σ_y are the rms widths of the transverse beam profiles (horizontal and vertical).

The beam intensities N_B and N_Y are determined using the wall current monitor (WCM) by measuring the current induced in an RLC circuit by the passing proton bunches. WCM performs very fast measurements (in nanoseconds) providing individual bunch profiles as a function of beam direction (z) and the measurements are sensitive to the presence debunched protons ('beam gas'). WCM measurements have $\sim 2\%$ systemetic uncertainty. Intensities are also determined by the Direct Current-Current Transformer (DCCT) by measuring currents induced in solenoids around the beam pipe by the fast moving proton bunches. DCCTs sample data for much longer time periods ($\sim$ 1 s) and provide the average value of the beam intensity. DCCT measurements are sensitive to the presence of the beam gas and have smaller ($\sim 0.2\%$) systematic uncertainty. The fast measurements by the WCMs are calibrated by the

more accurate DCCT measurements taken for a time period at the beginning of a fill when the protons are bunched and presencse of beam gas is at its minimum. Beam intensities are typically $\sim 10^{11}$/bunch and parts of the beam are lost with time due to collisions and scraping of the beam during the scans. Beam intensities are plotted as a function of time (and fitted with a linear function of time) to estimate the loss and are corrected for in the measurements of machine luminosity (Figures 4.1, 4.2). The effect of the intensity loss is, however, small for the relevant time period of the scan duration. For the $\sqrt{s} = 500$ GeV runs in the year 2009 at RHIC, proton numbers in a bunch ranged between $(0.6 - 1.1) \times 10^{11}$ with a few percent uncertainty. The machine luminosities (before the corrections as discussed later) ranged between $(3 - 5.5) \times 10^{29}$ $\mathrm{cm}^{-2}\mathrm{s}^{-1}$ with $1 - 2$ % uncertainty.

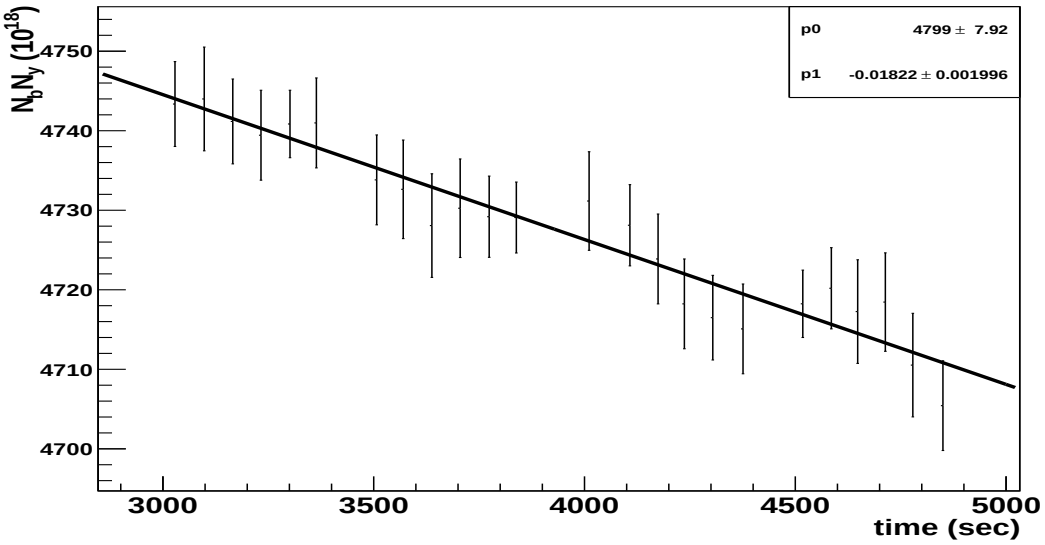

Figure 4.1: Beam intensity as a function of time during the Vernier scan for fill 10478 in 2009 RHIC run.

The transverse beam profiles are obtained by fitting the BBC triggered event rate (Fig. 4.3) with beam positions (Fig. 4.4) as one beam is moved in steps across the other (Vernier scan) and using the widths from the Gaussian fits. R_{max}^{BBC} is also obtained from the fits as the peak of the distributions when the beams maximally overlap. The

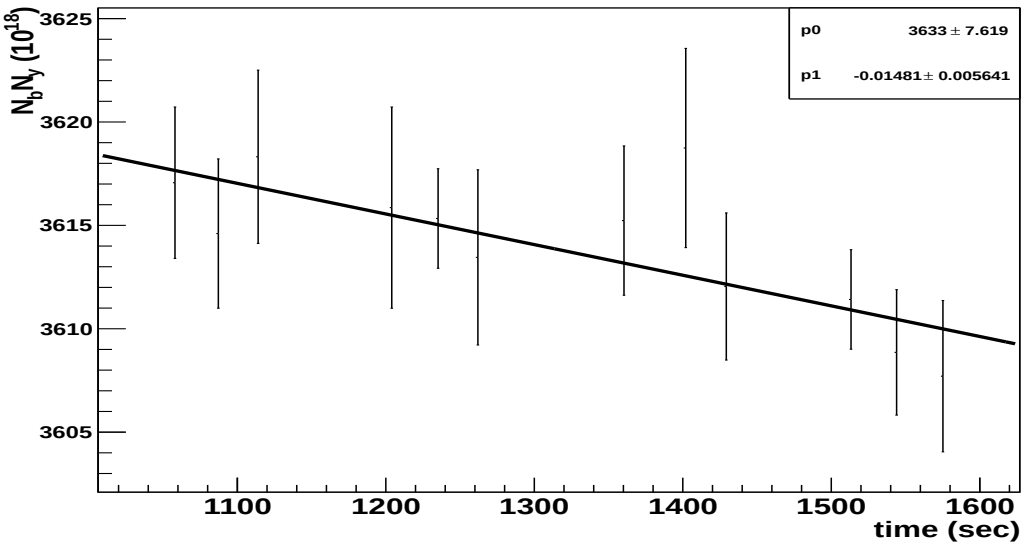

Figure 4.2: Beam intensity as a function of time during the Vernier scan for fill 10505 in 2009 RHIC run.

Vernier scans are done towards the end of the data taking period for a *fill* in the RHIC rings. One of the beams is moved in steps across the others first in the horizontal direction and then the vertical direction. Step sizes are chosen to be smaller than the expected width of the (typically) Gaussian profile of beams and are typically $\sim 100\ \mu$. At each of the steps the beams are held for $30 - 60$ seconds. Positions of the beams are measured using Beam Position Monitors (BPMs) at various locations along the RHIC rings. For the $\sqrt{s} = 500$ GeV runs in the year 2009 at RHIC, the beam widths ranged between 140 to 190 microns with an uncertainty of $2 - 5$ microns and the peak event rate (for maximum beam overlap) ranged between 4000 to 6800 Hz with an uncertainty of $100 - 300$ Hz.

Measured BPM steps are calibrated by the set step sizes by the collimating magnets. The ratios are plotted and fitted with a linear function $(Ax + B)$ for each of the scans (Fig. 4.5). The measured steps from BPM were found to be in good agreement with the set step sizes. The average slope (1.008) from all such fits is used to calibrate the measured step sizes.

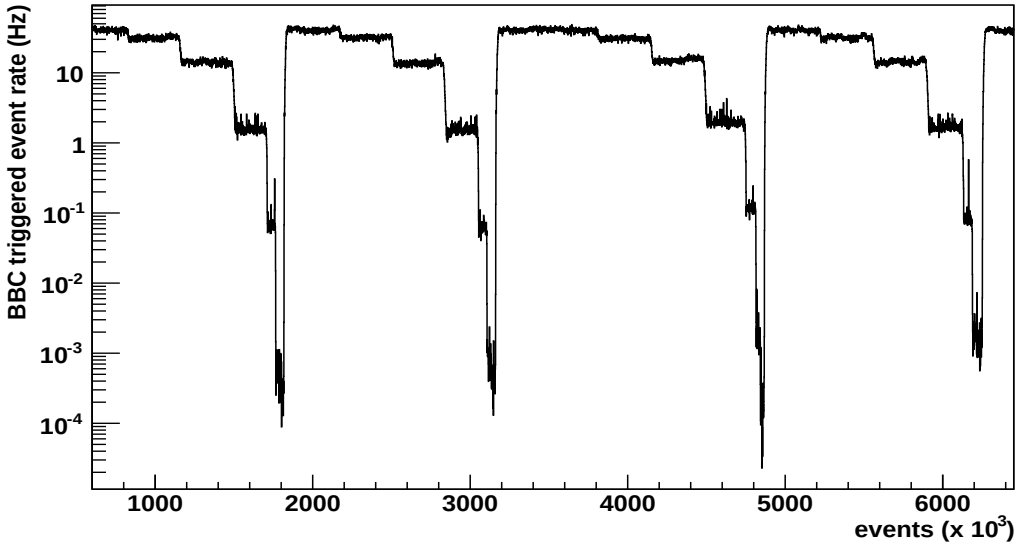

Figure 4.3: BBC triggered event rate from global level-1 scalers for fill 10478 in 2009 RHIC run.

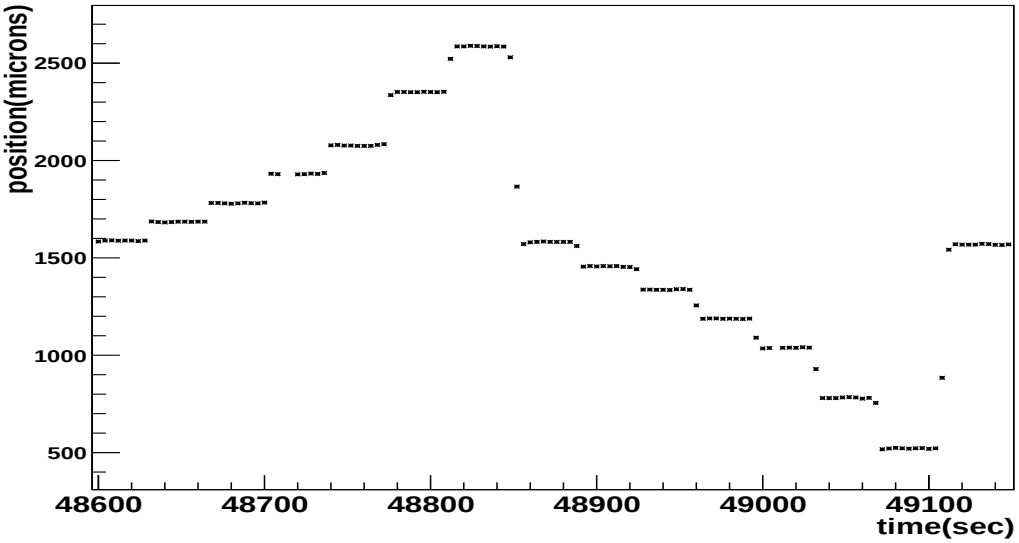

Figure 4.4: BPM position measurements for horizontal Vernier scan of fill 10478 in 2009 RHIC run.

Efficiency of the BBC trigger is determined by comparing the triggered data applying the restriction of a 30 cm cut on the vertex position to the data with same

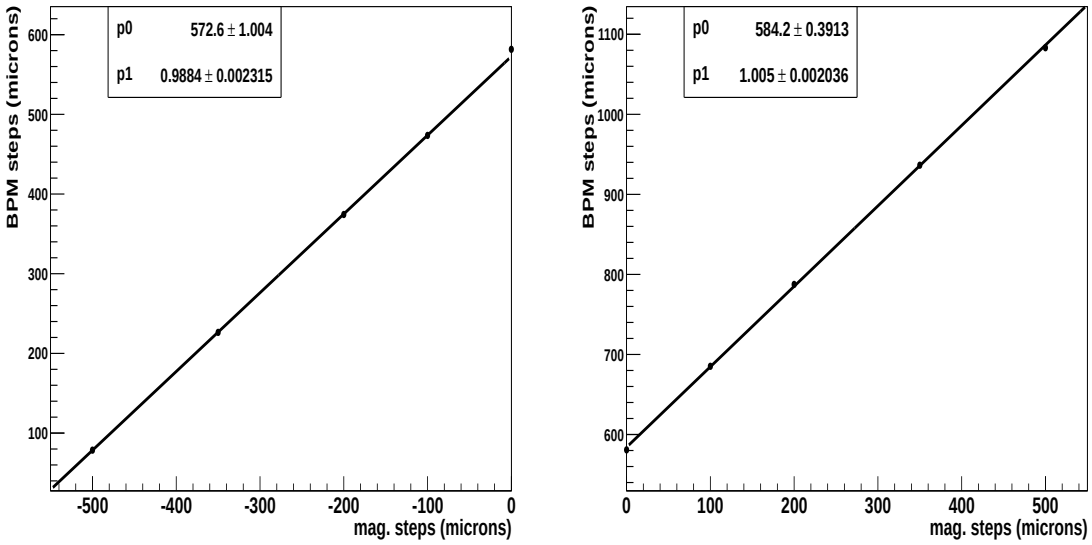

(a) (b)

Figure 4.5: Calibration of BM steps with steps set by changing magnetic fields for fill 10478 in RHIC 2009 run. Plot a) shows the ratio for horizontal steps in one side of the beam center and b) shows the ratio for the horizontal steps in the other side of the beam center.

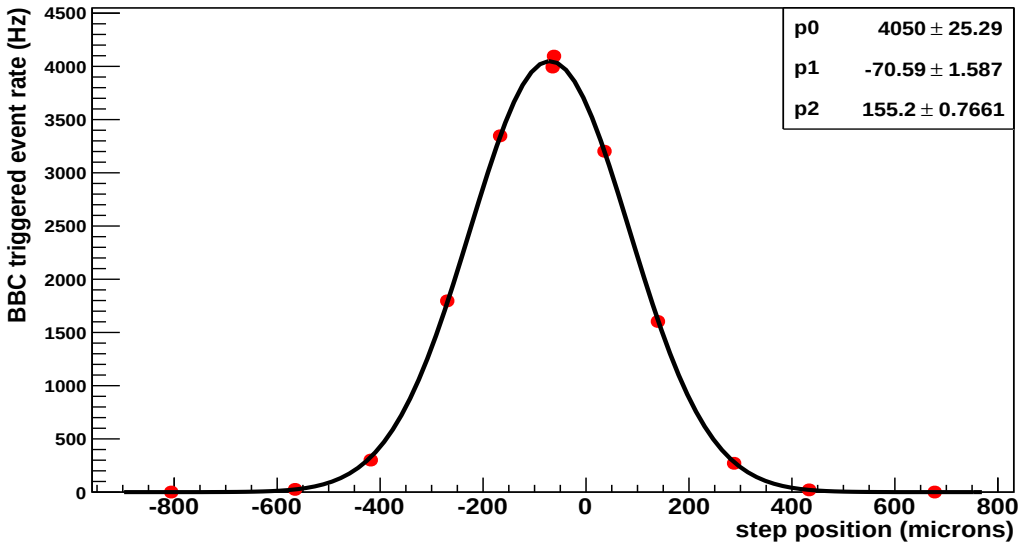

Figure 4.6: BBC triggered event rate vs. beam position (of a single bunch crossing) during the horizontal Vernier scan for fill 10478 in 2009 RHIC run.

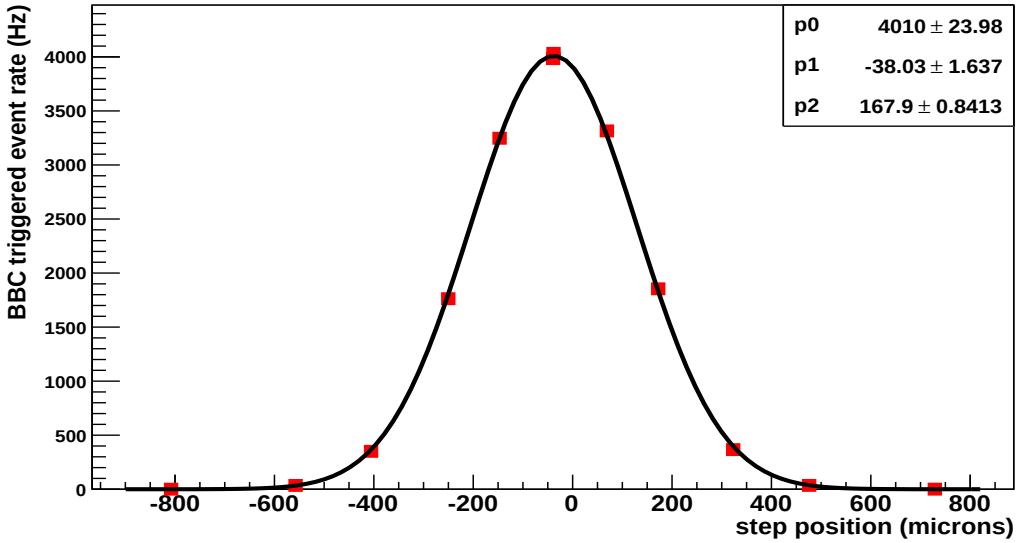

Figure 4.7: BBC triggered event rate vs. beam position (of a single bunch crossing) during the vertical Vernier scan for fill 10478 in 2009 RHIC run.

trigger with no vertex restriction. The fraction of the area under the curve for the imposed vertex range to the entire area under the curve in Fig. 4.8 provides a measurement of the BBC trigger efficiency ϵ_{BBC} in Eq. 4.2. However, BBC efficiency has a slight dependence on the position of the event vertex in the beam direction. ZDC is an independent device to measure luminosity and being far ($\sim$ 18 m) from the collision center and sensitive to different physics processes (diffractions as opposed to the hard scattering to which BBC is sensitive to), its efficiency is fairly independent of the vertex position along z. The BBC triggered data is compared to the ZDC triggered data and fitted with a parabolic function of z to determine the z-dependence of the BBC efficiency (Fig. 4.9). The extracted parameters of the function are used to correct the ϵ_{BBC} for the z-dependence. For the $\sqrt{s} = 500$ GeV runs in the year 2009 at RHIC, the values of ϵ_{BBC} for the 'BBCLL1($>$ 0 tubes)' trigger ranged between 0.52 to 0.57.

Magnets are used to focus the beams at the IP. This leads to a z-dependence of the transverse profiles of the beams as they get increasingly narrower while approaching

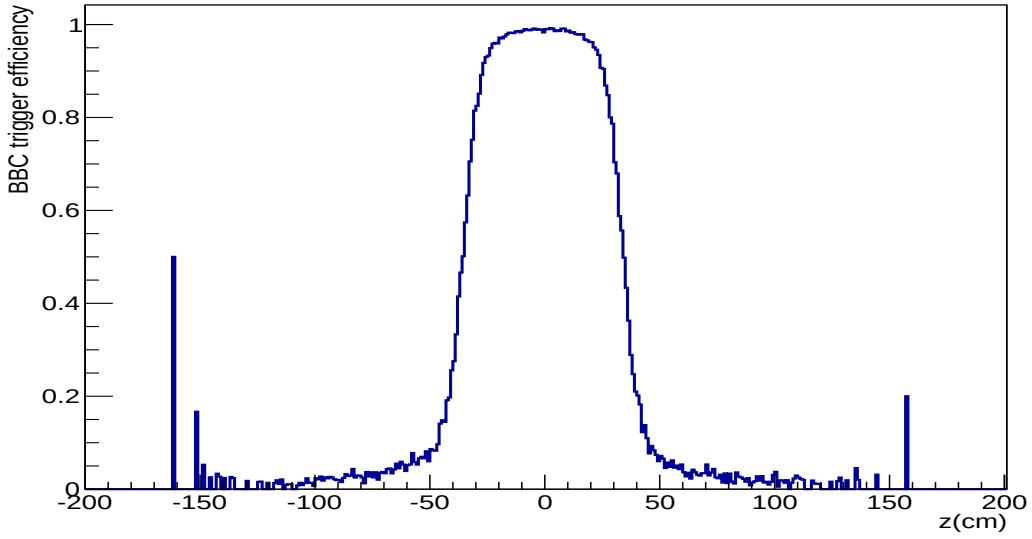

Figure 4.8: Ratio of 'BBCLL1(> 0 tubes)' trigger (online cut of 30 cm on vertex position) to BBC wide trigger (no vertex restriction) for fill 10478 in RHIC 2009 run.

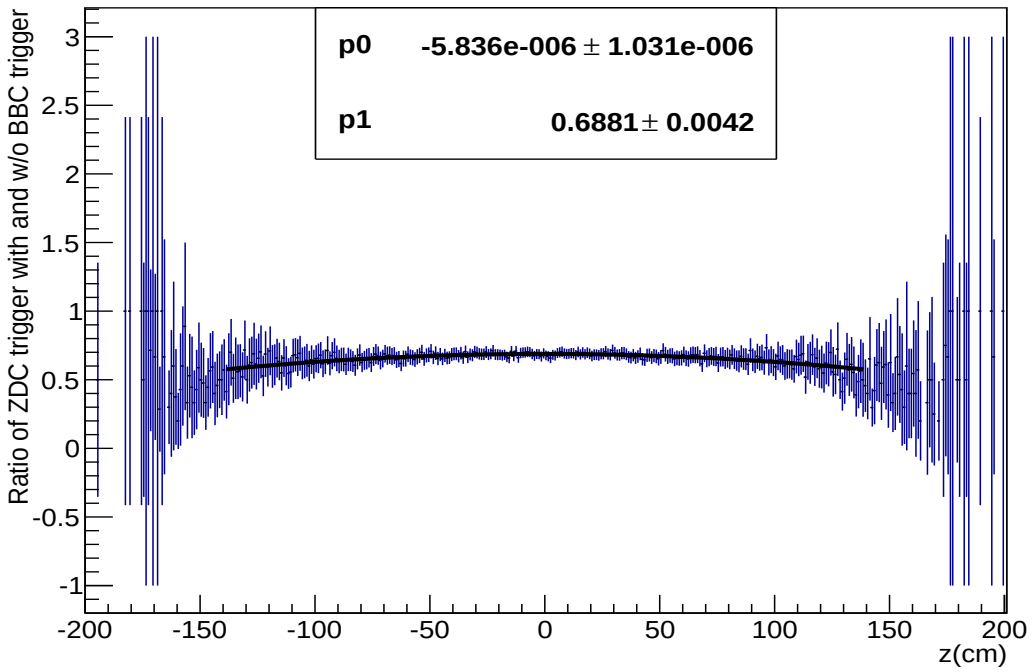

Figure 4.9: Ratio of ZDC triggered data with BBC wide trigger and without it for fill 10478 in RHIC 2009 run. Ratio is fitted to function $(Az^2 + B)$.

the IP and wider while moving away from it (till it reaches the stable width in the storage ring):

$$\sigma_{x,y}(z) = \sigma^0_{x,y}\sqrt{1 + \left(\frac{z}{\beta^*}\right)^2}, \tag{4.4}$$

where $\sigma^0_{x,y}$ is the beam width in horizontal (x) or vertical (y) direction at the collision center $z = 0$ and β^* is the focusing parameter. The resulting effect is named 'hourglass effect' after the transverse shape of the beams (look like tilted hourglass). This requires a correction for the beam transverse width terms in the luminosity calculation in Eq. 4.3. Coupled to the effect of the presence of a small (but non-zero) crossing angle between the beams, the vertex distribution of the events in the beam direction (z) assumes signature shapes. The effect on the vertex z-profile can be illustrated as shown in the cartoons in Fig. 4.10 and the resulting vertex profiles in the data can be seen in Fig. 4.12.

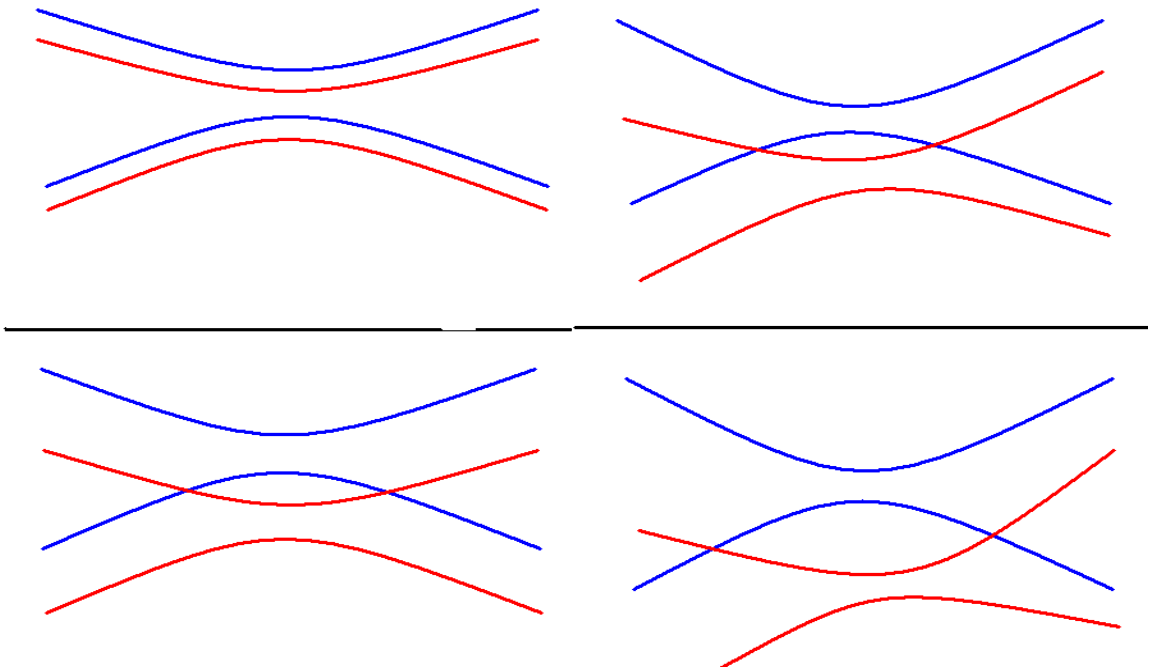

Figure 4.10: Figure shows the overlap area of two focused colliding beam for a) head-on collision and b) with a small crossing angle. Cartoon a) demonstrates the appearance of the double-peak structure of the vertex profile as one beam is moved in steps across the other and b) demonstrates the skewness between the two peaks as a result of the angle between them.

The corrections to the uniform width head-on collision scenario arising due to these effects are obtained by comparing the vertex z-profile of the data to a simulation with free parameters for the focusing strength β^* and crossing angle θ. Parameters are varied to minimize the χ^2 of the comparison of the simulated vertex profile to the data. The extracted parameters are used to apply corrections to the calculated machine luminosity. For the $\sqrt{s} = 500$ GeV runs in the year 2009 at RHIC, β^* was found to be 70 cm and crossing angle θ ranged between -0.5 to 0.11 mrad.

The sample plots of the measurements shown here are for the $\sqrt{s} = 500$ GeV $p+p$ data from the RHIC run in 2009. After applying all the appropriate corrections, the σ_{BBC} was determined to be 32.51 ± 3.01 sys ± 1.19 stat mb. The results were used

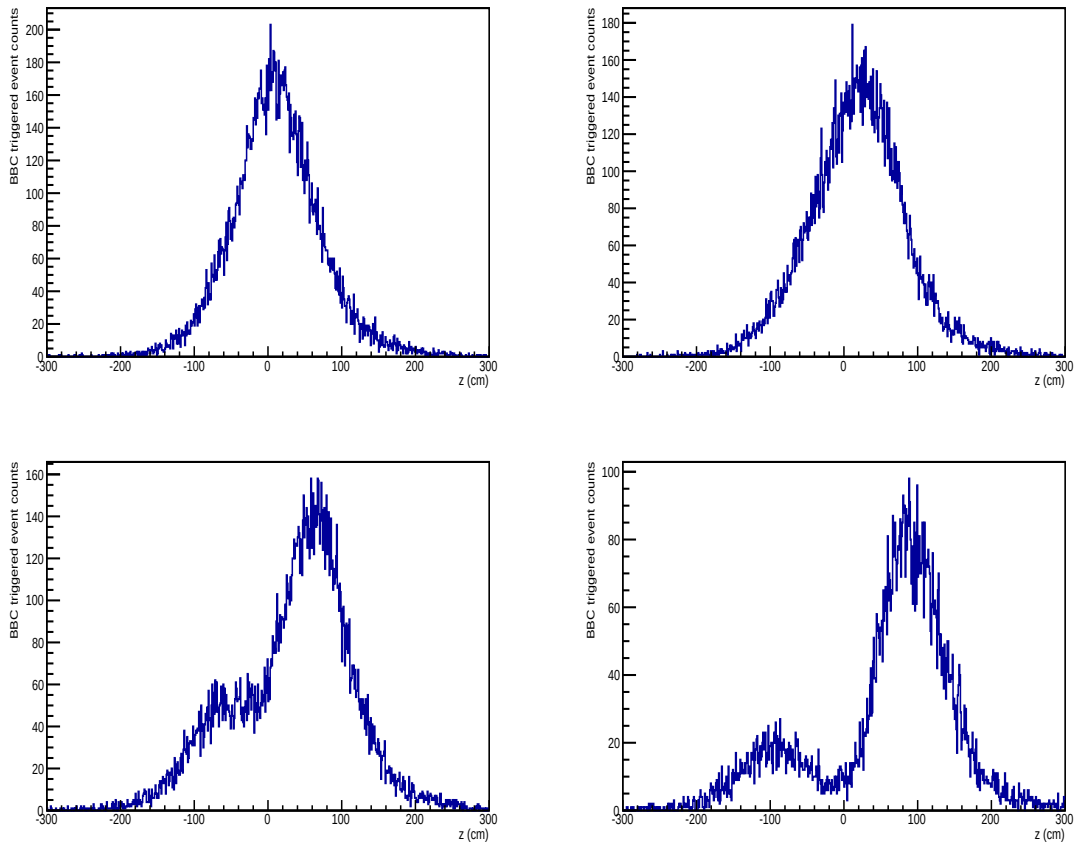

Figure 4.11: Vertex profile in beam direction for increasing step sizes (step $\sim$ 100 microns) during the horizontal scan of one of the beams by the other for fill 10478 in RHIC 2009 run. The further the beam centers are from each other, the more prominent the double structure becomes as only the tail regions of the tilted hourglass shape are overlapped. The skewness of the peaks also become more appreciable as with increasing steps as overlap on one side becomes comparatively larger than that on the other side.

to in the measurement of the W boson cross-section from the same data [18]. Using similar techniques the σ_{BBC} for the data ($p+p$ at $\sqrt{s} = 62.4$ GeV) relevant to the measurements described here were first measured and used for the neutral pion cross section measurements [15] and was determined to be 13.7 ± 1.5 sys mb.

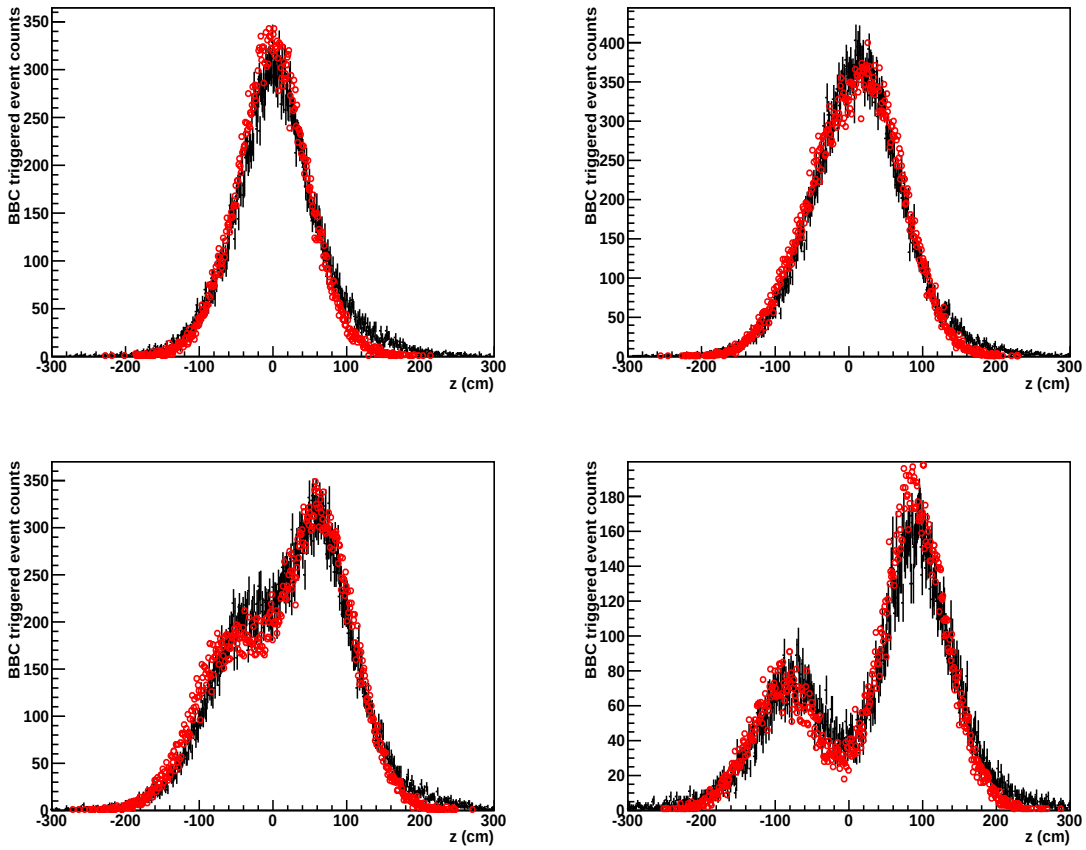

Figure 4.12: Comparison of the vertex profile in beam direction for increasing step sizes for one side of the vertical scans e.g. (1)top-left : step = 0, (2) top-right : step = 200 microns, (3) bottom-left : step = 350 microns, (4) bottom-right : step = 500 microns. In the simulation, $\beta^* = 70$ cm and $\theta = 0.06$ mrad. (Color online) Black points with error bars represent data and open red circles represent simulation.

4.0.2 Acceptance of Detectors and Efficiency of Selection Cuts

To estimate the combined efficiency of the selection criteria and geometrical acceptance of the detector system, single particle Monte Carlo simulations are performed and passed through the GEANT3 based detector configuration. It's essential to look at $C_{\rm eff}^{\rm acc}$ for each separate particle species in the charged hadron mix as it can be affected by the mass of each particle species and also the interactions and different decay processes of each species. A Million of each of the charged hadron species (π, K, p) and their antiparticles were generated, distributed uniformly in 2π azimuth, and

± 0.5 of rapidity (y) range with a uniform distribution in transverse momentum range of $0 \leq p_T \leq 7.0$ GeV/c. Particles were produced with a realistic vertex distribution (typically Gaussian with an r.m.s of 50 cm truncated at ± 30 cm) similar to that in the data. The simulations take into account dead-maps for several detectors from the period of time when the data was taken and were finally verified by comparing the live and most efficient detector areas in both Monte Carlo and data.

Matching variables ('PC3dϕ', 'PC3dz') of the positive and negative pions were used for the calibrations for all species before we imposed the selection window as pions were the bulk of the hadron mix and also because the variations for different species were not significant for the purpose. Matching variable distributions in each of the p_T bins were fitted with the combination of a narrow Gaussian for the signal (hadron tracks generated at the vertex) and a second wider Gaussian for the background. The widths and means of the signal Gaussians were parameterized as a function ($Ae^{Bp_T} + C$) of p_T. In order to select hadrons from simulated events, a 2σ cut was imposed on the variables normalized using the mean and the width from the functional forms.

The ratio of particles generated in a certain p_T bin, detected within the complete range $0 \leq p_T \leq 7$ GeV/c and passing all our hadron selection cuts to the initial number of particles generated in that p_T bin were calculated. These ratios $E_{\rm eff}^{\rm acc}$ for different hadron species are shown in Figures 4.15 and 4.16. The smearing of the momentum of the detected charged tracks were decoupled and corrected for separately (described in Sect. 4.0.3). The requirement that the particles are detected within the complete range of generated p_T effectively ignores the possible smearing of the track momentum in the detection process.

The small efficiency for the kaons is due to decays of kaons (into pions mostly) in flight. The large decrease in the $E_{\rm eff}^{\rm acc}$ at low p_T is due to the fact that the fixed pseudo-rapidity acceptance of the detector corresponds to a narrow range in rapidity

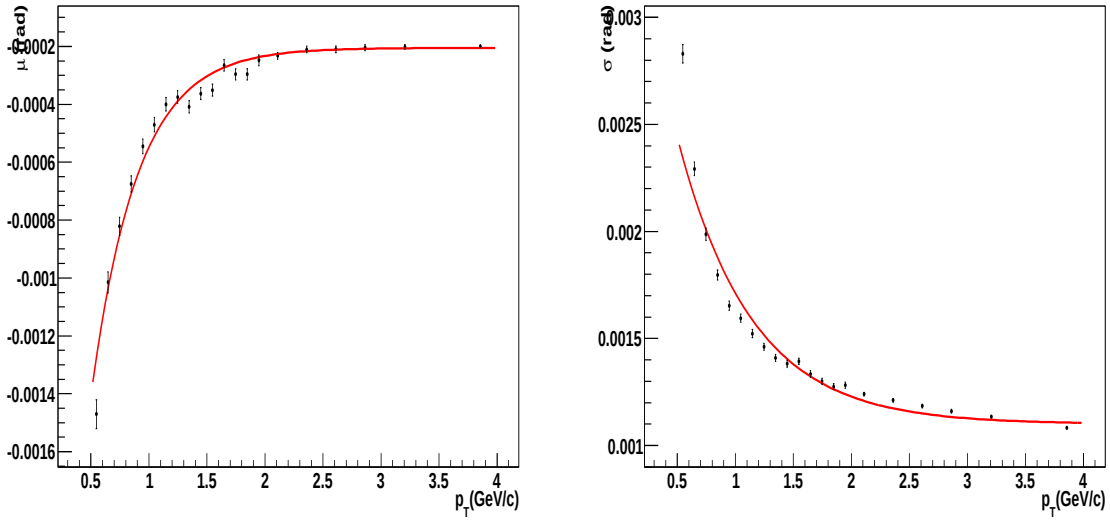

(a) Mean ($\mu_{pc3d\phi}$)

(b) Width ($\sigma_{pc3d\phi}$)

Figure 4.13: Means and widths of Gaussian fits to 'pc3dϕ' of positive pions as function of p_T.

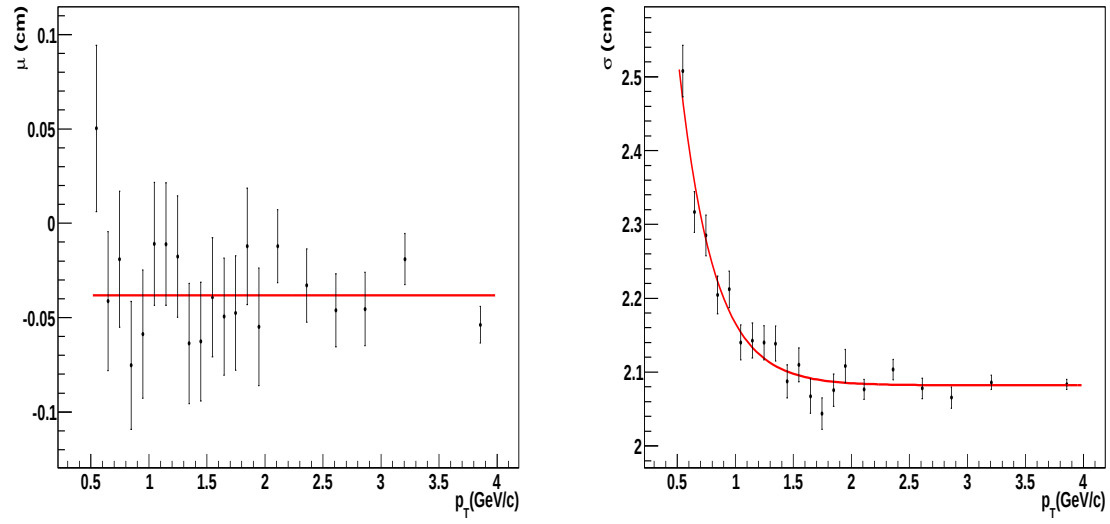

(a) Mean (μ_{pc3dz})

(b) Width (μ_{pc3dz})

Figure 4.14: Means and widths of Gaussian fits to 'pc3dz' of positive pions as function of p_T.

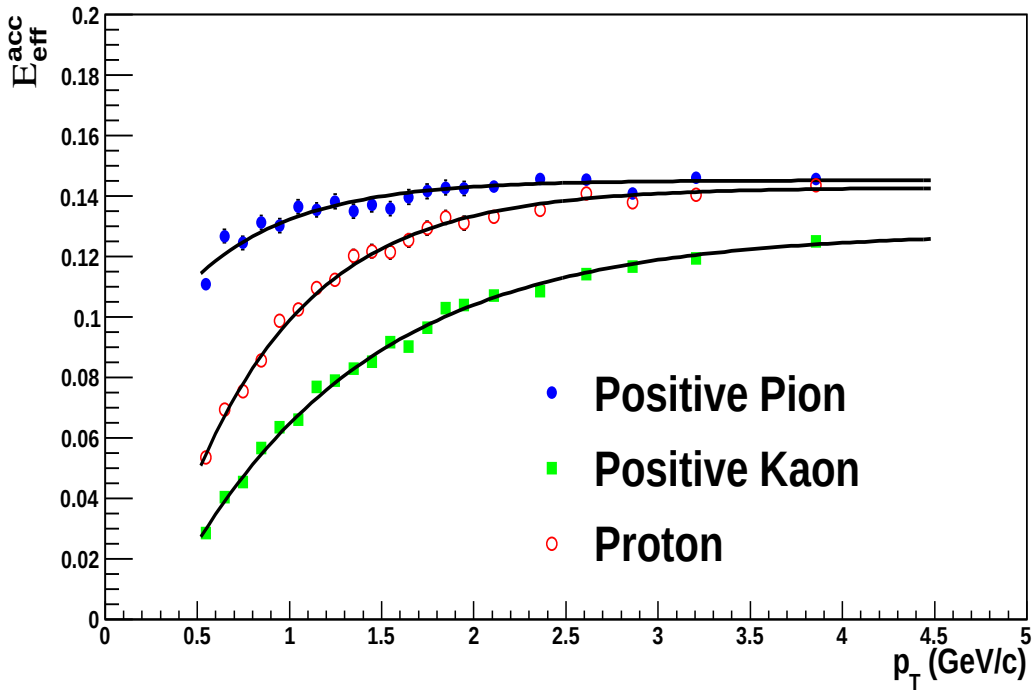

Figure 4.15: Efficiency (includes geometrical acceptance, efficiency of detectors and efficiency of cuts), for positive hadrons.

for smaller p_T/m. The efficiencies were parameterized ($Ae^{Bp_T} + C$) as a function of p_T (Table 4.1) and fit values were used for the calculation of cross sections.

As mentioned above, for the purpose of the verifying the MC simulation with data, three of the largest and most efficient areas of the detector were chosen for each of the quadrants (two sides of the nominal interaction center for each of the two arms of detector systems). The ratio of the fractions of counts in the three selected regions for each quadrant from data and simulation were calculated and the weighted average (using the total count in each quadrant as the weights) was used to scale the efficiencies from the simulation. The standard deviation was assigned as the uncertainty of the ratio. The individual scale factors in each quadrant are listed below (Table. 4.2) for positive and negative hadrons.

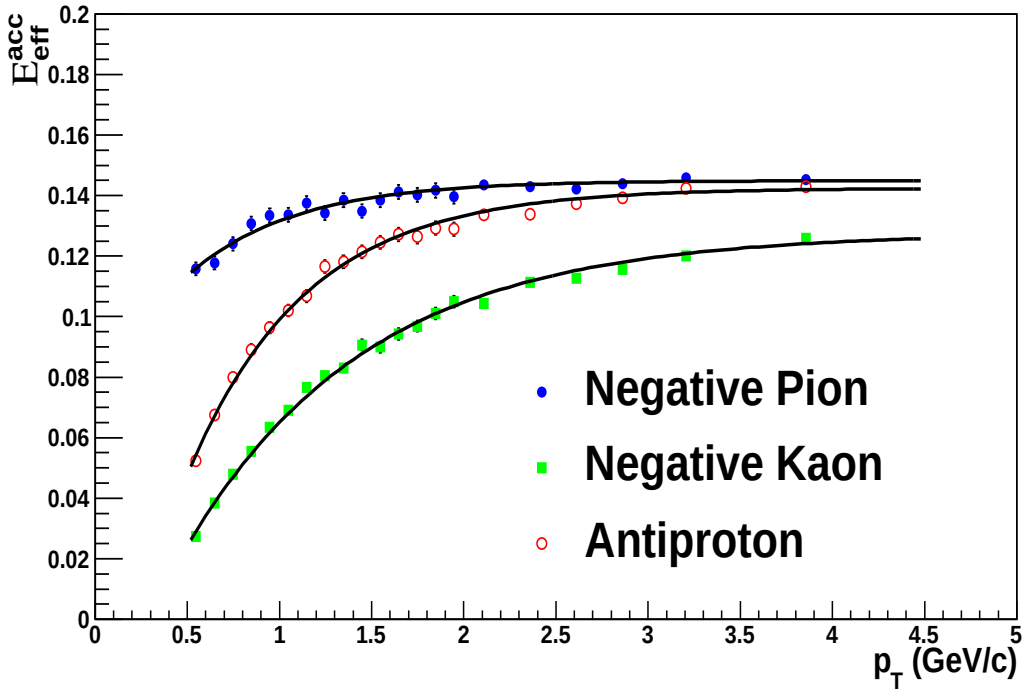

Figure 4.16: Efficiency (includes geometrical acceptance, efficiency of detectors and efficiency of cuts), for negative hadrons.

Positive:

4.0.2.1 Applying The Correction

The correction factor $C_{\rm eff}^{\rm acc}$ was applied according the relative fraction of each of the species in the detected hadron mix. As described in detail in Sect. 3.3, the production ratios of the hadron species are calculated fitting the identified hadron data. Combined with these fractions f_i for a species i, the relation between detected yield Y_{det} and the corrected yield Y_{cor} becomes :

$$Y_{cor} \times \sum_i f_i (E_{\rm eff}^{\rm acc})_i = Y_{det} \quad (4.5)$$

$$Y_{cor} = \frac{Y_{det}}{\sum_i f_i (E_{\rm eff}^{\rm acc})_i}. \quad (4.6)$$

hadron	A	B	C
π^+	-0.08	-1.8	1.453
K^+	-0.17	-0.97	1.280
p	-0.21	-1.54	1.428
π^-	-0.07	-1.7	1.449
K^-	-0.17	-1.01	1.276
p^-	-0.21	-1.56	1.424

Table 4.1: Fit function parameters for the efficiency curves for different hadron species. See text in Sect. 4.0.2 for details.

hadrons	East-North	East-South	West-North	West-South
h^+	1.08 ± 0.13	1.08 ± 0.03	1.02 ± 0.07	1.10 ± 0.06
h^-	1.05 ± 0.09	1.04 ± 0.02	1.08 ± 0.04	1.16 ± 0.06

Table 4.2: Scale factors applied to Monte Carlo simulation to account for live detector area in each quadrant of the detector for positive and negative hadrons.

The correction factor for acceptance and efficiency $C_{eff}^{acc} = 1/\sum_i f_i(E_{\rm eff}^{\rm acc})_i$ for the charged hadrons are shown in Figures 4.17 and 4.18.

4.0.3 Momentum Smearing and Correction

As mentioned in Sect. 4.0.2, the corrections due to effects of detectors were decoupled into two separate parts : (1) a correction term based on the combined detector efficiency, geometrical acceptance and efficiency of our selection cuts and (2) a separate correction term that accounts for the uncertainty of the reconstructed hadron tracks owing to the finite resolution arising from the angular resolution of DC and multiple scattering of the tracks inside DC (more prominent for low p_T tracks). Angular resolution in DC can be well approximated by a Gaussian distribution of width ~ 0.9 mrad [22].

For the later correction, we started with a known spectrum of yield using ISR [40] identified pion cross section. Pion spectra are fitted with a parameterization $A(1 + \frac{p_T}{B})^2$. Cross sections are converted in produced particle counts in p_T bins and species

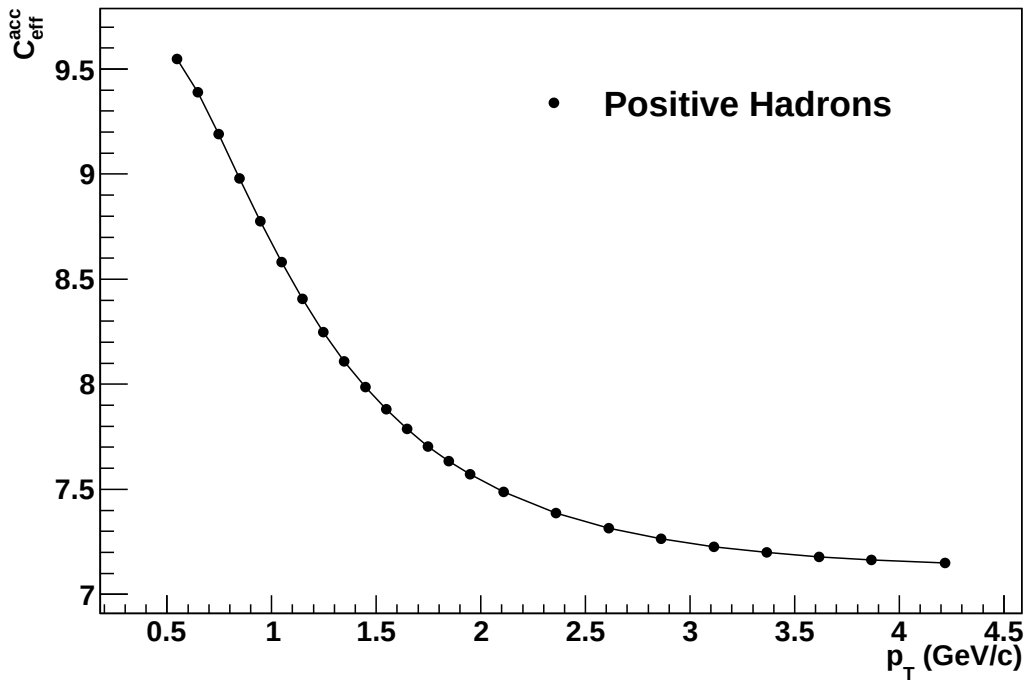

Figure 4.17: Combined correction factor for the geometrical acceptance of the detector and the efficiency of the selection criteria for positive hadrons.

fraction f_i and efficiencies E_{eff}^{acc} are applied to get detected counts or 'yields' in each bin. As a next step, all yields in the p_T bins are converted in terms on α bins, where bending angle $\alpha = K_1/p$, where $K_1 = 101$ mrad GeV/c. Yield in each of the alpha bins are distributed (smeared) according to a Gaussian around the mean alpha of the bin with a width equal to the α-resolution $\delta\alpha$. The value used for the total angular resolution is :

$$\delta\alpha = 0.9 + 0.007\alpha, \tag{4.7}$$

where the first term comes from angular resolution of Drift Chamber and the second α-dependent term incorporates the effects of the multiple scattering which is more prominent at low p_T or high α. The values used are the same as used in previous PHENIX results [12], the $\delta p/p$ being converted to $\delta\alpha$ in this case.

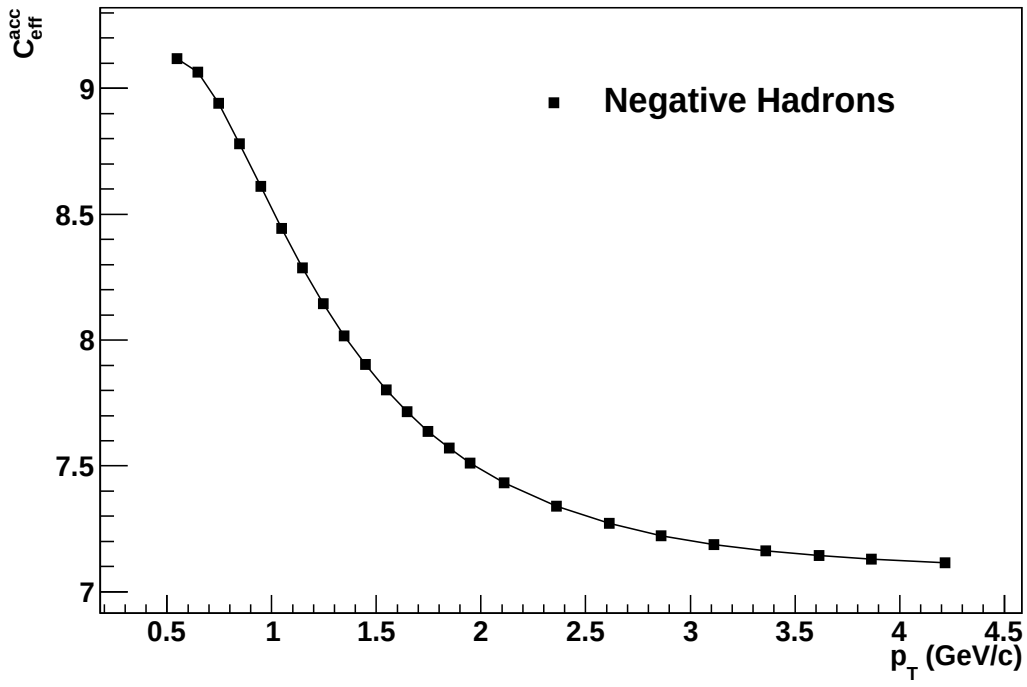

Figure 4.18: Combined correction factor for the geometrical acceptance of the detector and the efficiency of the selection criteria for negative hadrons.

After the smearing of the contents, each alpha-bin may get contributions from all other bins. Finally the ratio of initial ('true') spectrum and the final ('smeared') spectrum is calculated. The ratios are parameterized by two separate third-order polynomials (in mutually exclusive range of p_T) for the complete range of interest $0.5 \leq p_T \leq 4.5$ GeV/c. The parameters for the fit are tabulated below 4.3. The systematic uncertainty is introduced by the angular resolution.

We also use a separate value of angular resolution [11], $\delta\alpha = 1.0 + 0.007\alpha$ to estimate the smearing correction and the difference between correction factors starting from two different resolution values is used as the systematic uncertainly. The difference is p_T dependent and is a maximum of 2% at highest p_T bin. Smearing correction is applied to the background subtracted yield. This brings the spectrum of yields

'true' p_T bins instead of smeared p_T. All the other corections are obtained in terms of 'true' p_T, so they are applied subsequently.

parameter (range 1)	positive ($p_T < 2.5\text{GeV}/c$)	negative ($p_T < 2.5\text{GeV}/c$)
p_0	1.00100	1.00050
p_1	-0.00292	-0.00195
p_2	0.00207	0.00192
p_3	-0.00095	-0.00095
parameter (range 2)	positive ($p_T > 2.5\text{GeV}/c$)	negative ($p_T > 2.5\text{GeV}/c$)
p_0	0.99520	0.99650
p_1	0.00789	0.00646
p_2	-0.00388	-0.00329
p_3	0.00009	0.00009

Table 4.3: Parameter values for smearing correction factor.

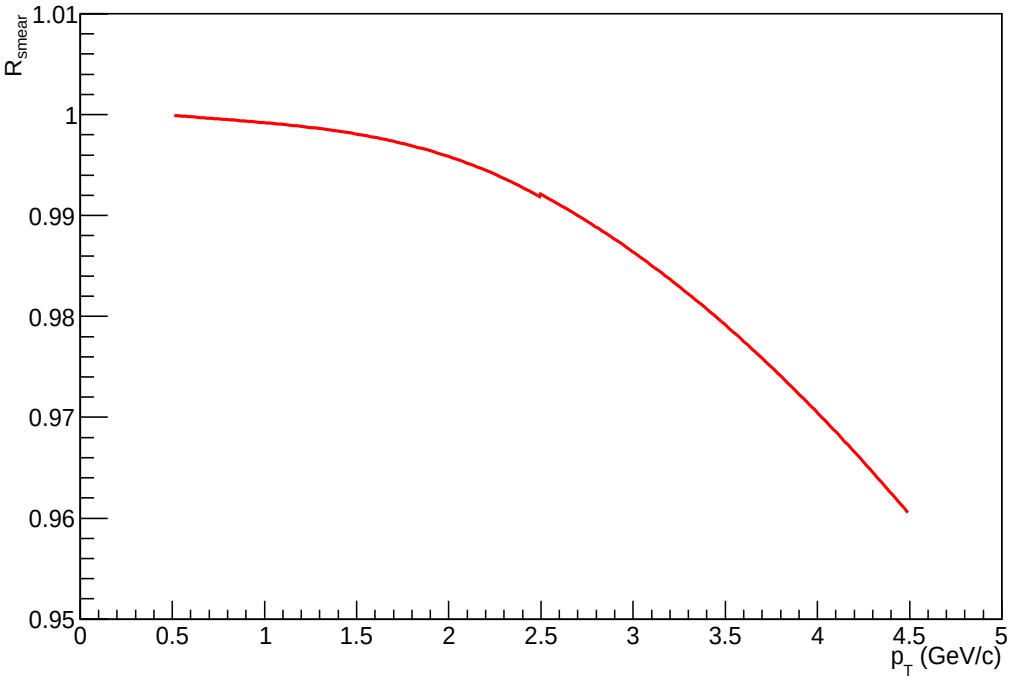

Figure 4.19: Correction factor for the momentum smearing of reconstructed tracks in the detector. Figure shows fit to the ratio of the positive charged hadron spectrum in 'true' p_T vs. that in the 'smeared' p_T.

4.0.4 Trigger Bias Correction

As mentioned previously (Sect. 3.1), analyzed events were triggered by requiring coincidence of BBC hits on both sides of the collision center (minimum bias trigger). The trigger bias was calculated by taking the ratio of the number of reconstructed π^0 in the high p_T photon triggered (EM calorimeter and RICH trigger) data with and without requiring the coincidence of the minimum bias trigger [15]. The calculated trigger bias is parameterized as a second order polynomial function of p_T and the parameterized values are used for the calculation of the cross sections. The trigger bias as depicted in Fig. 4.20 shows a decrease towards the higher end of p_T. This effect is understood in terms of a deficit of the energy available to the forward (in pseudo-rapidity) particles while producing high p_T tracks in the mid-rapidity.

The trigger bias is parameterized as a non-linear function of p_T as shown below. The functional values are used to calculate cross section at various p_T bins.

$$\mathcal{E}_{trigger} = \frac{1}{C_{\rm trig}} = a_0 + a_1 p_T + a_2 {p_T}^2,$$

where $a0 = 0.4027 \pm 0.0154$,

$a1 = 0.01966 \pm 0.0109$,

$a2 = -0.00647 \pm 0.0018$.

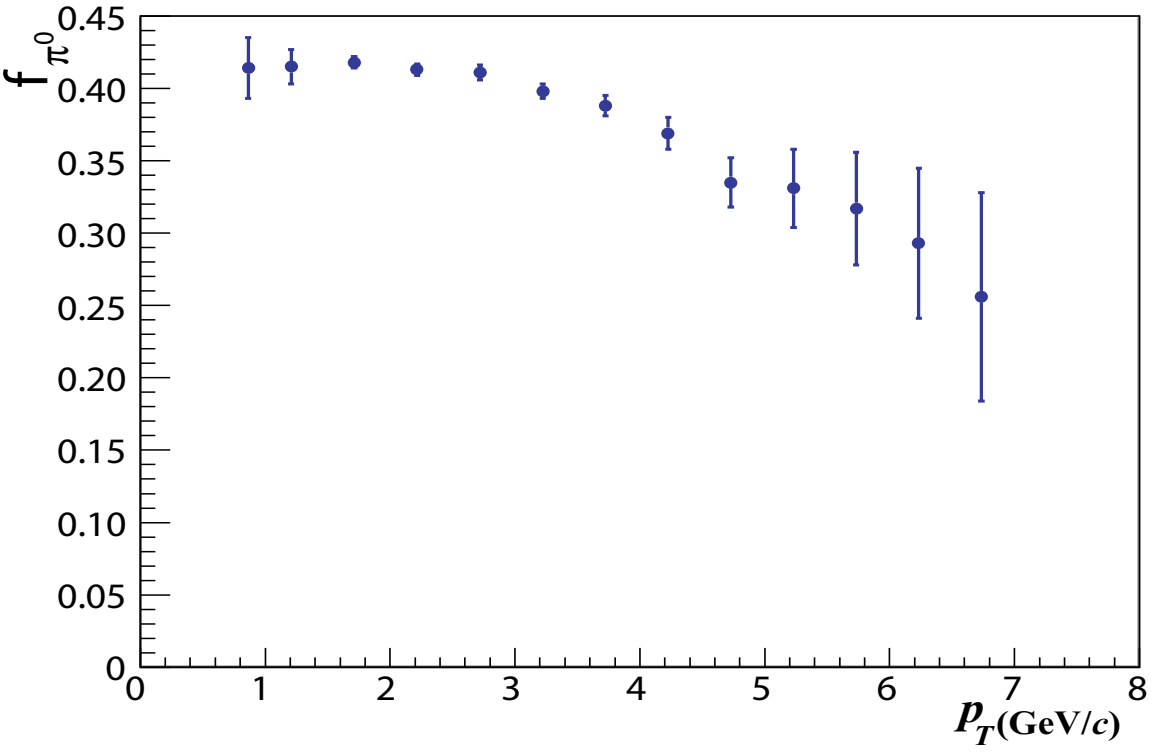

Figure 4.20: Parameterized efficiency of Minimum Bias trigger.

4.0.5 Cross Section Results

The cross sections of inclusive charged hadron production in unpolarized $p + p$ collisions at center of mass energy of 62.4 GeV were calculated and compared to the theoretical calculations of next-to-leading order accuracy using perturbative QCD. The measured cross sections results are presented in Figures 5.1 and 5.2. The upper panel compares our measurement with the NLO calculation with and without the logarithmic corrections at scale $\mu = p_T$. As we will discuss, the next-to-leading logarithmic corrections have been predicted [62] to be significant for lower energy systems and previous measurements [15] have indicated that it might be true for low energy collisions at RHIC. The lower panels show the dependence of the theoretical calculations on the choice of factorization and renormalization scales for both NLO and NLL calculations.

4.0.6 Uncertainties on Cross Sections

The largest contribution ($11 - 24\%$) to the p_T dependent systematic uncertainty comes from the correction for the detector acceptance and efficiencies. The uncertainty on the cross section due to this correction factor is determined by varying the selection parameters (selection window in matching variables) in the MC simulations. Another prominent contribution to the systematic uncertainties comes from the luminosity normalization factor σ_{BBC} which is determined with an 11% systematic uncertainty. The trigger bias introduces a 2.5% uncertainty. Determination of the background fraction and the production fraction of separate hadron species each introduces $1 - 5\%$ p_T-dependent systematic uncertainty. Uncertainties from other sources (e.g. correction for momentum resolution, correction for active area of detector in experiment and Monte Carlo) are $\sim 1 - 2\%$.

Source	Systematic Uncertainty
σ_{BBC}	11%
Trigger bias	2.5%
Acceptance & efficiency correction	11-24%
MonteCarlo/data scale factor	2%
PID fraction	1-5%
Background fraction	1-5%
Momentum smearing correction	1-2%

Table 4.4: Systematic uncertainties of cross section measurements from various sources.

Tables for cross sections and asymmetries are presented below as a function of the transverse momentum of the produced final state hadrons.

Mean p_T (GeV/c)	Positive Hadron (h^+) mb GeV^{-2}c^2
0.548	$(780 \pm 0.12 \pm 110) \times 10^{-2}$
0.647	$(478 \pm 0.0087 \pm 59) \times 10^{-2}$
0.747	$(287 \pm 0.0063 \pm 35) \times 10^{-2}$
0.847	$(173 \pm 0.0046 \pm 21) \times 10^{-2}$
0.947	$(106 \pm 0.0034 \pm 13) \times 10^{-2}$
1.047	$(65.5 \pm 0.025 \pm 8.2) \times 10^{-2}$
1.147	$(41.8 \pm 0.019 \pm 5.2) \times 10^{-2}$
1.247	$(26.7 \pm 0.015 \pm 3.4) \times 10^{-2}$
1.347	$(17.3 \pm 0.012 \pm 2.2) \times 10^{-2}$
1.447	$(11.4 \pm 0.009 \pm 1.4) \times 10^{-2}$
1.547	$(77.3 \pm 0.072 \pm 9.3) \times 10^{-3}$
1.647	$(52.5 \pm 0.057 \pm 6.4) \times 10^{-3}$
1.747	$(35.9 \pm 0.046 \pm 4.4) \times 10^{-3}$
1.848	$(24.6 \pm 0.037 \pm 3.1) \times 10^{-3}$
1.948	$(17.4 \pm 0.030 \pm 2.0) \times 10^{-3}$
2.110	$(9.61 \pm 0.014 \pm 1.1) \times 10^{-3}$
2.359	$(41.9 \pm 0.085 \pm 5.0) \times 10^{-4}$
2.612	$(18.9 \pm 0.055 \pm 2.4) \times 10^{-4}$
2.861	$(8.80 \pm 0.036 \pm 1.2) \times 10^{-4}$
3.113	$(43.3 \pm 0.24 \pm 5.4) \times 10^{-5}$
3.365	$(22.0 \pm 0.16 \pm 2.9) \times 10^{-5}$
3.616	$(10.9 \pm 0.11 \pm 1.7) \times 10^{-5}$
3.866	$(60.3 \pm 0.81 \pm 9.0) \times 10^{-6}$
4.218	$(24.6 \pm 0.35 \pm 6.0) \times 10^{-6}$

Table 4.5: The cross sections of mid-rapidity charged hadron production from $p + p$ at $\sqrt{s} = 62.4$ GeV as a function of p_T are tabulated along with the corresponding statistical (second column) and systematic (third column) uncertainties. Cross sections and errors for positive hadrons with the feed-down correction for protons and antiprotons applied (normalization uncertainty of 11.2% not included).

Mean p_T (GeV/c)	Negative Hadron (h^-) mb GeV^{-2}c^2
0.548	$(687 \pm 0.11 \pm 9.3) \times 10^{-2}$
0.647	$(410 \pm 0.080 \pm 5.0) \times 10^{-2}$
0.747	$(245 \pm 0.057 \pm 2.9) \times 10^{-2}$
0.847	$(146 \pm 0.042 \pm 1.7) \times 10^{-2}$
0.947	$(8.83 \pm 0.031 \pm 1.1) \times 10^{-2}$
1.047	$(54.3 \pm 0.023 \pm 6.6) \times 10^{-2}$
1.147	$(34.0 \pm 0.017 \pm 4.1) \times 10^{-2}$
1.247	$(21.6 \pm 0.013 \pm 2.6) \times 10^{-2}$
1.347	$(14.1 \pm 0.010 \pm 1.6) \times 10^{-2}$
1.447	$(9.21 \pm 0.080 \pm 1.1) \times 10^{-2}$
1.547	$(61.1 \pm 0.063 \pm 7.2) \times 10^{-3}$
1.647	$(41.1 \pm 0.050 \pm 4.7) \times 10^{-3}$
1.747	$(27.9 \pm 0.040 \pm 3.3) \times 10^{-3}$
1.848	$(19.0 \pm 0.032 \pm 2.2) \times 10^{-3}$
1.948	$(13.1 \pm 0.026 \pm 1.5) \times 10^{-3}$
2.110	$(73.2 \pm 0.12 \pm 8.3) \times 10^{-4}$
2.359	$(31.4 \pm 0.073 \pm 3.5) \times 10^{-4}$
2.612	$(13.8 \pm 0.046 \pm 1.6) \times 10^{-4}$
2.861	$(63.6 \pm 0.30 \pm 7.5) \times 10^{-5}$
3.113	$(31.2 \pm 0.20 \pm 3.8) \times 10^{-5}$
3.365	$(16.7 \pm 0.14 \pm 2.5) \times 10^{-5}$
3.616	$(7.41 \pm 0.091 \pm 1.1) \times 10^{-5}$
3.866	$(40.2 \pm 0.64 \pm 5.5) \times 10^{-6}$
4.218	$(18.8 \pm 0.29 \pm 5.3) \times 10^{-6}$

Table 4.6: The cross sections of mid-rapidity charged hadron production from $(p + p$ at $\sqrt{s} = 62.4$ GeV as a function of p_T are tabulated along with the corresponding statistical (second column) and systematic (third column) uncertainties. Cross sections and errors for negative hadrons with the feed-down correction for protons and antiprotons applied (normalization uncertainty of 11.2% not included).

CHAPTER 5

DISCUSSION OF CROSS SECTION RESULTS

In the overlapping p_T range, the cross section results were found to be consistent with the species-combined cross sections from identified results [15] at PHENIX as well as identified cross sections at ISR [40] from data at collision energy of $\sqrt{s} = 63$ GeV. On the upper panels of Figs. 5.1 and 5.2 the cross sections are compared to the NLO and NLL calculations at a factorization, renormalization and fragmentation scale of $\mu = p_T$ [63]. The calculations were performed using MRST2002 unpolarized PDFs [81] and DSS fragmentation functions [57].

The NLO predictions have been shown to describe cross section results for neutral pions [24, 13] and charged hadrons [25] at $\sqrt{s} = 200$ GeV within $\sim 20\%$ for a scale choice of $\mu = p_T$. For the present results at $\sqrt{s} = 62.4$ GeV, however, the NLO calculations underpredict the data by as much as ~ 80 % in the case of positive hadrons and $\sim 60\%$ in the case of negative hadrons for a scale choice of p_T. Resummation of higher order logarithmic terms tend to imrove the pQCD results although these calculations over predict the data. The lower two panels in the plots show the dependence of the theoretical calculations on the choice of factorization, renormalization and fragmentation scale (μ) for three different values (p_T, $\frac{p_T}{2}$, $2p_T$). The inclusion of higher order terms in the NLL calculations leads to a considerably smaller scale dependence.

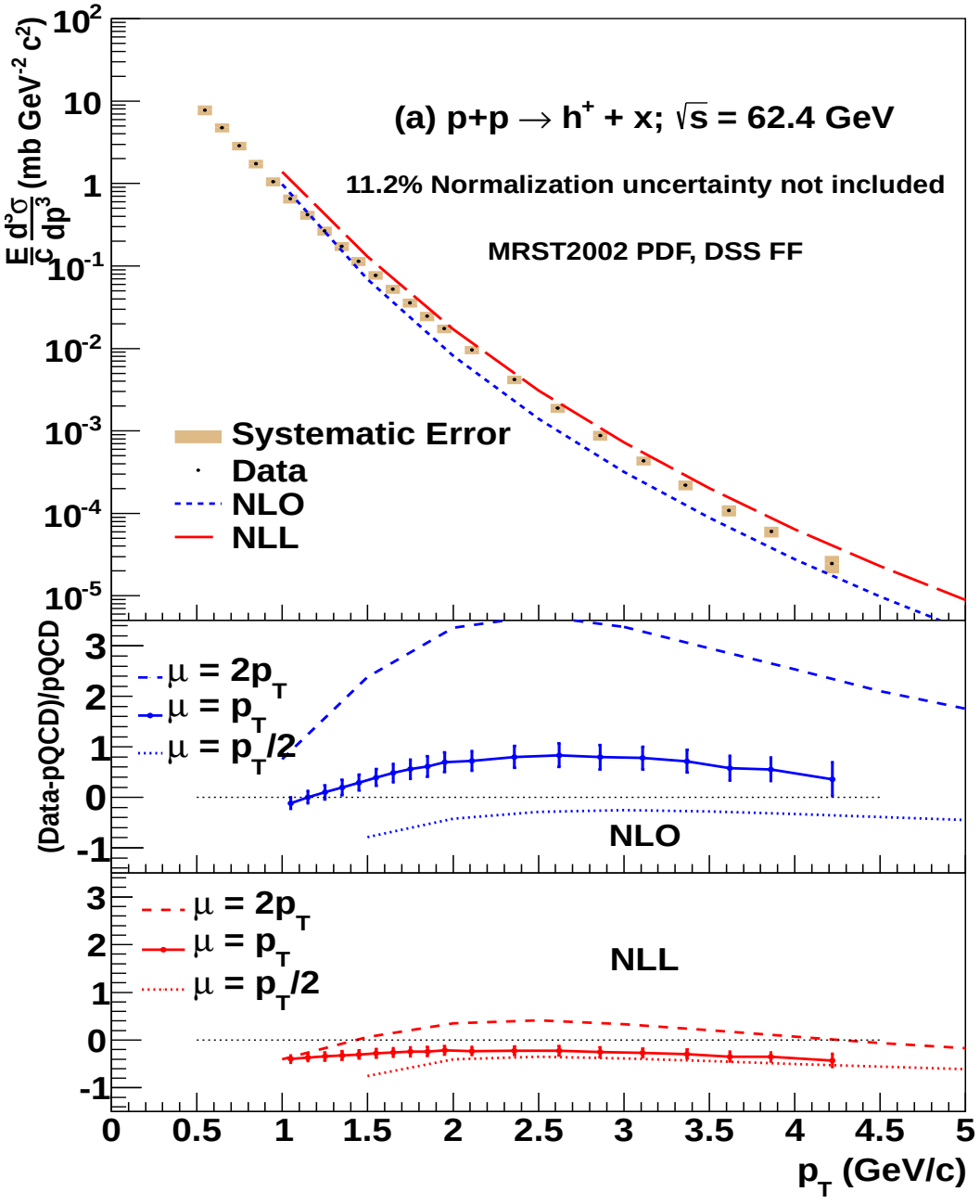

Figure 5.1: Cross section of mid-rapidity production of inclusive positive hadrons in $p+p$ at 62.4 GeV. NLO and NLL theoretical predictions at factorization, renormalization and fragmentation scale $\mu = p_T$ are shown on plots. Lower panels show the scale dependence of the NLO and NLL results respectively.

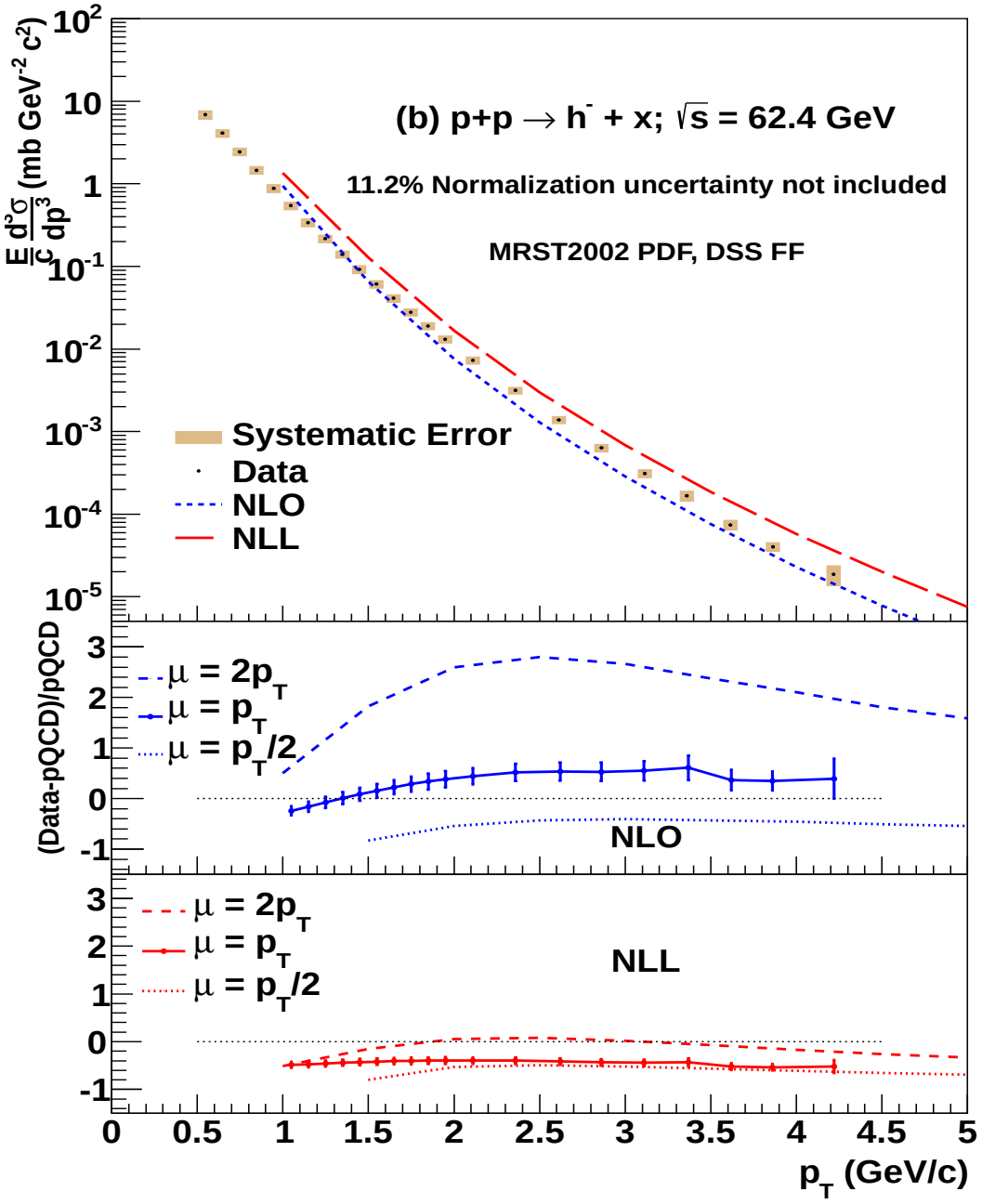

Figure 5.2: Cross section of mid-rapidity production of inclusive negative hadrons in $p+p$ at 62.4 GeV. NLO and NLL theoretical predictions at factorization, renormalization and fragmentation scale $\mu = p_T$ are shown on plots. Lower panels show the scale dependence of the NLO and NLL results respectively.

These new data at an energy intermediate to typical fixed-target and collider energies are timely, as the details of how to work with resummation techniques in different kinematic regimes are currently being explored by the theoretical community (see for example [62, 61, 39]). Comparison of the present results to the calculations at NLO with and without NLL terms included indicates that in the measured kinematic range, NLL terms make relevant contributions to the cross section. However, the tendency of the NLL calculations to over predict the data, as much as $\sim 40\%$ in the case of positive hadrons and $\sim 50\%$ in the case of negative hadrons for a scale choice of p_T, may indicate that there are terms in the full NNLO expansion that are of comparable magnitude and opposite sign to those in the NLL calculation. Possible inclusion of higer order terms in any future pQCD calculation might describe the data more closely.

These measurements corroborate similar indications from the neutral pion cross section results [15] and identified hadron cross section results [20] at PHENIX measured from data at the same energy. The present measurements can also be useful in a future determination of inclusive charged hadron fragmentation functions, as progress in pQCD has allowed inclusion of $p+p$ cross section measurements and semi-inclusive deep-inelastic lepton-nucleon scattering data in FF parameterizations along with the traditionally used e^+e^- data since 2007 [58, 57, 30].

CHAPTER 6

DOUBLE HELICITY ASYMMETRY MEASUREMENT

Hadron production in $p+p$ scattering at $\sqrt{s} = 62.4$ GeV with transverse momentum p_T below 5 GeV/c is mostly dominated by quark-gluon scattering at leading order in perturbative QCD (pQCD), providing sensitivity to the gluon helicity distribution in the proton. In the rapidity range ($-0.35 < \eta < 0.35$) covered by the PHENIX central arm detectors [21], scattering of quarks and gluons with momentum fractions $0.05 \lesssim x_{gluon} \lesssim 0.2$ are probed. The double helicity asymmetry A_{LL} is a quantity that contains information of the parton distributions in the colliding protons. Our present measurement of A_{LL} of inclusive hadron production in polarized $p + p$ collisions is sensitive to gluon distribution in leading order.

6.0.7 Double Helicity Asymmetry and Uncertainty

The measured A_{LL} here is defined as the relative difference between the production cross sections from collisions of same and opposite helicity protons :

$$A_{LL} = \frac{\sigma^{++} - \sigma^{+-}}{\sigma^{++} + \sigma^{+-}} \tag{6.1}$$

where $\sigma^{++}(\sigma^{+-})$ is the production cross section of the species from collisions of same (opposite) helicity protons. In practice, the polarization of colliding proton beams

are not 100%. So, the calculation are normalized by the product of the beam polarizations. In terms of measurable quantities, the double helicity asymmetry is :

$$A_{LL} = \frac{1}{P_1 P_2}\left(\frac{N^{++}/L^{++} - N^{+-}/L^{+-}}{N^{++}/L^{++} + N^{+-}/L^{+-}}\right) \quad (6.2)$$

$$= \frac{1}{P_1 P_2}\left(\frac{N^{++} - RN^{+-}}{N^{++} + RN^{+-}}\right) \quad (6.3)$$

where P_1, P_2 are the polarizations of two colliding beams, $N^{++}(N^{+-})$ are hadron track counts (yields) for same (opposite) helicity configuration of colliding proton bunches and $R = L^{++}/L^{+-}$ is the relative luminosity of the colliding beams.

PHENIX uses two different luminosity monitors, BBC and ZDC. For luminosity measurements to be used in the asymmetry measurements, the detector needs to have high statistics with fairly low backgrounds and it needs to cover the offline vertex range $|z_{vtx}| \leq 30$ cm used for the asymmetry measurements. The vertex restriction is imposed for essentially two reasons. Firstly, the vertex distribution of the event rate is almost unchanged within 30 cm region as the complete distribution is fairly Gaussian with ~ 60 cm width. Secondly, the iron yoke of the PHENIX central magnet starts at $z = \pm 40$ cm and blocks the particles reaching central arm detectors outside the selected range. Triggered events at BBC is ~ 40 times higher than those trigged by ZDC (a coincidence of hits on both sides of the detector triggers an event). The spatial resolution of BBC (~ 5 cm) is much better than that of the ZDC (~ 30 cm). So the vertex requirements is more precise while using the BBC as the luminosity monitor. BBC is therefore used as the luminosity counter for the asymmetry measurements as it has (a) small background, (b) higher statistical precision and (c) more precise measurement of z-vertex range.

BBC triggered ('BBCLL1' or 'BBC local level 1') event counts are recorded for each bunch crossing and are called 'scalers'. The relative luminosity R is calculated fill by fill by adding the scalers corresponding to the same and the opposite helicity

bunch crossing separately and taking a ratio of the luminosity for the same to that of the opposite helicity crossings. Due to the limitation of the bandwidths for the data acquisition systems and the physics requirements of taking data for several different trigger settings, only fractions of the triggered events are recorded at PHENIX (typical in similar collider experiments, a marked difference from the statistically starved experiments, e.g. neutrino experiments). While calculating relative luminosities for each fill, the luminosity counts from the BBC scalers were weighted by the pre-scale factor for the corresponding trigger in each of the runs. Luminosities of BBC and ZDC triggered events (combined triggers as well as mutually exclusive) were compared to determine the systematic uncertainty of the relative luminosity measurements. The method is well described in [48]. The systematic uncertainty of the relative luminosity measurement was found to be $\delta A_{LL} = 1.4 \times 10^{-3}$.

The polarization of the two colliding proton beams were obtained from fill by fill measurements of pC polarimeter results, normalized by the H-jet results [2]. For the entire data set with the longitudinal beam polarizations, the values for the two colliding beams (termed 'Blue' and 'yellow') were $\langle P_B \rangle = 0.481 \pm 0.009$ (stat) $\pm$ 0.032 (sysB) $\pm$ 0.014 (sysG) and $\langle P_Y \rangle = 0.479 \pm 0.0059$ (stat) $\pm$ 0.03 (sysB) $\pm$ 0.04 (sysG). Final systematic uncertainty on the product of the polarizations $\langle P_B P_Y \rangle$ was found to be $\pm$13.9%.

Since the double helicity asymmetry is a ratio of the cross sections, most of the systematic uncertainties cancel, rendering the statistical uncertainties of the measurements the relevant ones. The statistical uncertainties of the asymmetries can be estimated as:

$$\delta A_{LL} = \frac{1}{P_B P_Y} \frac{2RN^{++}N^{+-}}{(N^{++}+N^{+-})^2} \sqrt{(\frac{\Delta N^{++}}{N^{++}})^2 + (\frac{\Delta N^{+-}}{N^{+-}})^2}, \tag{6.4}$$

where ΔNs are the statistical uncertainty in measuring the number of final products of our interest. For a completely Poissonian distribution(each event contributing

maximum of 1 track per bin), $\Delta N = \sqrt{N}$. However, it is also probable that some collision events produce more than 1 tracks. So we correct for the 'enhancement factor' coming from the multiplicity distribution to estimate the correct statistical uncertainties ΔN^{++} and ΔN^{+-}.

6.0.8 Multiplicity Correction

We look into the multiplicity distribution of positive and negative particle tracks separately for each of our p_T bins Fig. 6.1. With the correction of the enhancement factor, the uncertainty is estimated as $\Delta N = \sqrt{\frac{\overline{k^2}}{\overline{k}} N}$, where $\overline{k}$ is the average multiplicity. Enhancement factors for different p_T bins are listed in the table (6.1).

p_T bin(GeV/c)	k-factor for (+)ve Hadron	k-factor for (-)ve Hadron
0.5-1.0	1.022	1.018
1.0-2.0	1.007	1.006
2.0-3.0	1.001	1.001
3.0-4.5	1.0	1.0

Table 6.1: Enhancement factors from multiplicity correction

We measured $N^{++}(N^{+-})$ from collision data. We measured relative luminosity using event counts from luminosity monitor BBC. Polarizations were measured by pC and H-jet polarimeters. For 62.4 GeV data from 2006 run at RHIC, polarization of each beam was $\sim 58\%$. All these information were combined to calculate A_{LL} for each 'Fill' at RHIC and then combined statistically to extract the final double helicity asymmetry result. The background subtracted asymmetry and statistical uncertainty were calculated as :

$$A_{LL} = \frac{A_{LL}^{Sig+BG} - r \times A_{LL}^{BG}}{1-r} \tag{6.5}$$

$$\delta A_{LL}^{Sig} = \frac{\sqrt{(\delta A_{LL}^{Sig+BG})^2 + r^2 (A_{LL}^{BG})^2}}{1-r} \tag{6.6}$$

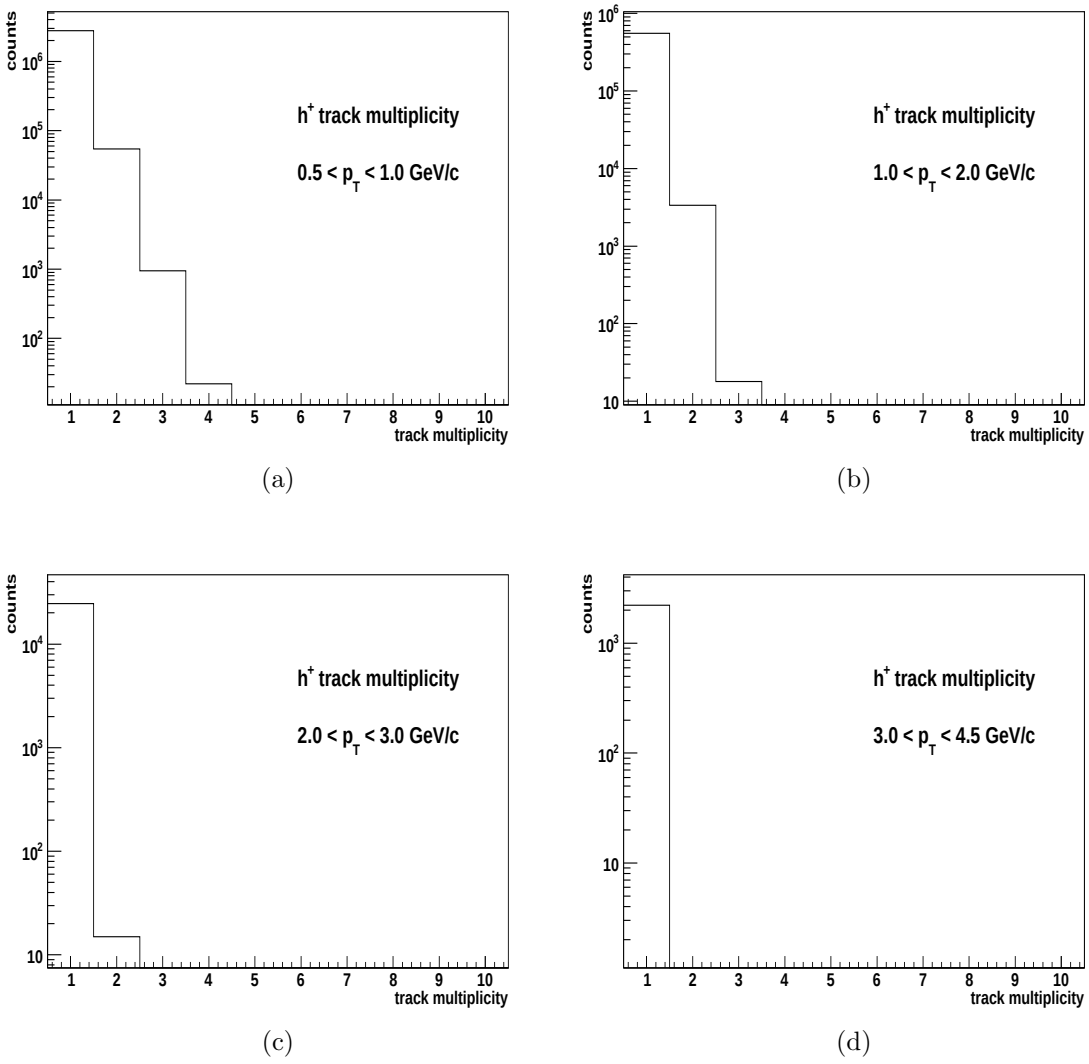

Figure 6.1: Multiplicity distributions of positive hadrons in the transverse momentum bins.

6.0.9 Asymmetry Results

The double helicity asymmetry A_{LL} of the mid-rapidity production of inclusive hadrons for both charges are presented in the Table. 6.2. The results are plotted along with pQCD calculations using several different parameterizations of the polarized PDFs later in Sect. 7 and significance of the results are discussed in detail. However, several cross checks are also performed to ensure that certain systematics do not

contribute as false asymmetries. Two important cross checks (a) measurements of longitudinal single spin asymmetry (A_L) and (b) bunch shuffled measurements of A_{LL} are discussed respectively in the following Sect. 6.0.10 and Sect. 6.0.11.

p_T(GeV/c)	$A_{LL} \pm \delta A_{LL}$ (h^+)	feed-down fraction f_{h^+}	$A_{LL} \pm \delta A_{LL}$ (h^-)	feed-down fraction f_{h^-}
0.68	0.0023 ± 0.0022	0.022	-0.0065 ± 0.0024	0.021
1.26	-0.01096 ± 0.0048	0.016	-0.0096 ± 0.0052	0.025
2.29	0.0132 ± 0.0204	0.012	0.0208 ± 0.0236	0.021
3.40	-0.0299 ± 0.0517	0.011	-0.0761 ± 0.0578	0.018

Table 6.2: The double helicity asymmetries and the statistical uncertainties are presented as a function of p_T for positive and negative non-identified charged hadrons. The fractional contribution to the yields from weak-decay feed-down to protons and antiprotons is shown; no correction to the asymmetries has been made for these contributions.

6.0.10 Single Spin Asymmetries

As we know, the strong force is a parity conserving force. Therefore, parity violating asymmetry are not expected to be observed. For processed involving hard scattering (QCD interactions), we do not expect to observe the parity violating longitudinal single spin asymmetry, defined by :

$$A_L = \frac{\sigma_+ - \sigma_-}{\sigma_+ + \sigma_-} \tag{6.7}$$

$$= -\frac{1}{P}\left(\frac{N^+ - RN^-}{N^+ + RN^-}\right), \tag{6.8}$$

where σ_+, σ_- are the cross sections of positive and negative helicity bunches for a chosen beam (summed over the polarizations of the other beam), N^+, N^- are the particle yields for the positive and negative helicity of the chosen beam and P is the polarization of the said beam. Under parity operator, the momentum vector changes changes sign, whereas the spin does not, resulting in a change of sign in helicity (which is the dot product of the spin and the momentum). After parity

operation, the longitudinal single spin asymmetry A_L as defined above changes sign too, rendering it to have the only possible zero value.

We measured single spin asymmetries for the 'blue' and 'yellow' beam separately for each of the charges and the results were found to be consistent with zero taking into consideration the statistical uncertainties on the asymmetry measurements. Figures 6.2 and 6.3 show the results below.

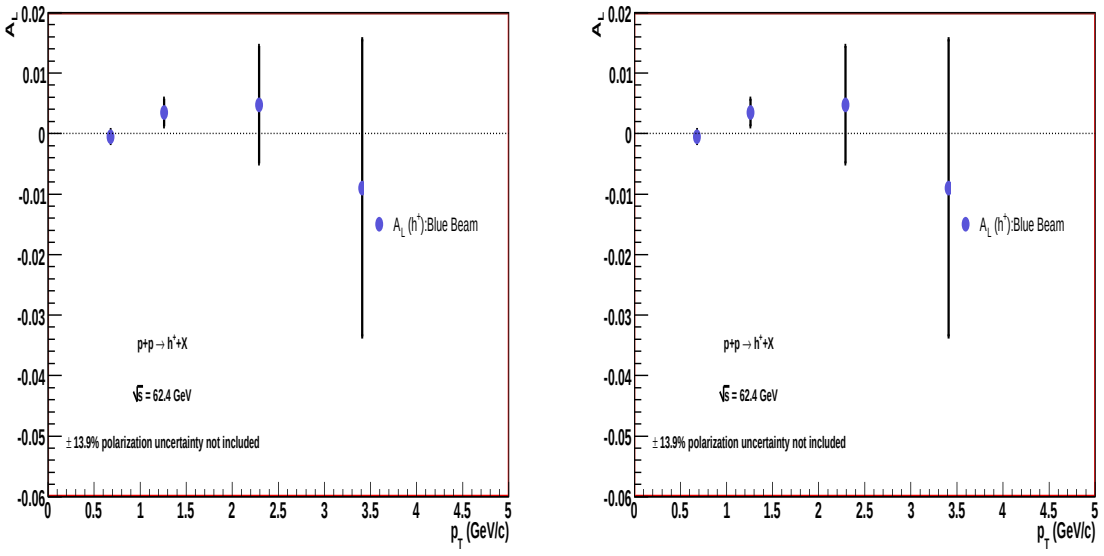

(a) h^+ (b) h^-

Figure 6.2: Single spin asymmetries for the 'blue' beam for a) positive and b) negative hadrons.

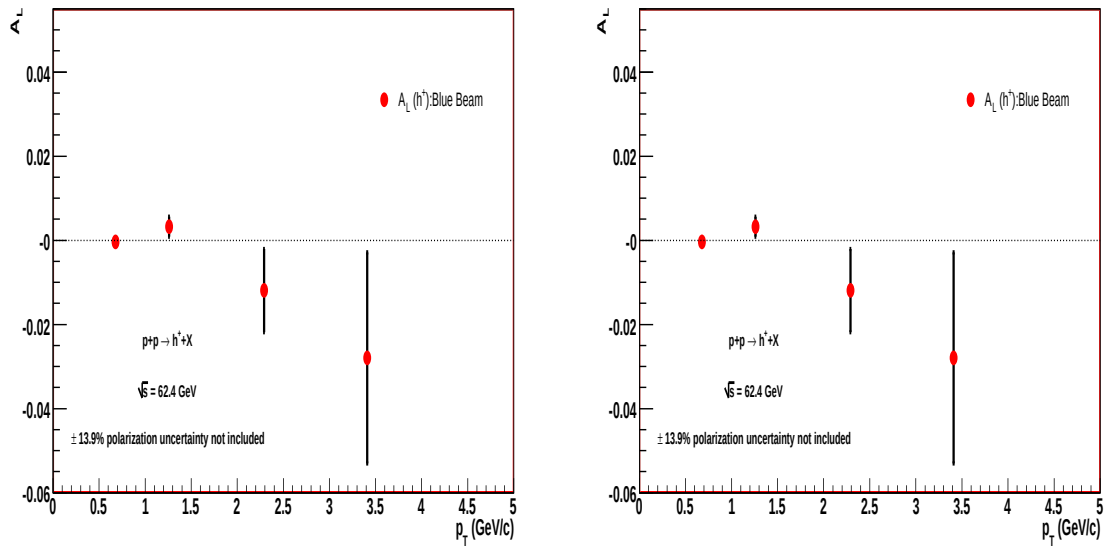

(a) h^+ (b) h^-

Figure 6.3: Single spin asymmetries for the 'yellow' beam for a) positive and b) negative hadrons.

6.0.11 Bunch Shuffling

'Bunch shuffling' is a technique used to ensure that uncorrelated bunch to bunch and/or fill to fill systematics are smaller than the statistical uncertainties of the asymmetry measurements. In this method, the spin direction of each of the bunch crossing is assigned randomly and the double helicity asymmetries from the collision data with the fake spin configurations are measured. The process is repeated a number of times (ten thousand for this analysis).

Given the random assignment of spins of the colliding bunches, in the absence of any systematic bunch to bunch and/or fill to fill errors, one can expect a zero double asymmetry measurement. To be precise, a Gaussian distribution of the measured double helicity asymmetries with zero mean is expected. Without the presence of any systematic error, the rms width of this distribution should match the calculated statistical uncertainty of the properly measured asymmetries. If the bunch shuffled

distribution shows larger width than the measured statistical uncertainties, it will indicate the presence of bunch to bunch systematic effects. A detailed study of the bunch shuffling technique can be found in [31].

Results of the bunched shuffled asymmetry distributions for the positive hadrons in four p_T bins are shown below in Fig. 6.4. The widths of the distributions are in good agreement with the measured statistical uncertainties of the double helicity asymmetries as can be seen in the Table. 6.3. The comparison indicates that the A_{LL} measurements are not affected by bunch to bunch uncorrelated systematic effects.

p_T bin (GeV/c)	$\delta A_{LL}^{h^+}$ (S+Bkg)	RMS of shuffled $A_{LL}^{h^+}$	$\delta A_{LL}^{h^-}$ (S+Bkg)	RMS of shuffled $A_{LL}^{h^-}$
0.5 - 1.0	0.0022	0.0022	0.0023	0.0025
1.0 - 2.0	0.0046	0.0046	0.0051	0.0049
2.0 - 3.0	0.020	0.018	0.023	0.022
3.0 - 4.5	0.047	0.046	0.051	0.051

Table 6.3: Table for the comparison of statistical uncertainties of double helicity asymmetry measurements and the rms width of the distribution of bunch shuffled fake asymmetries.

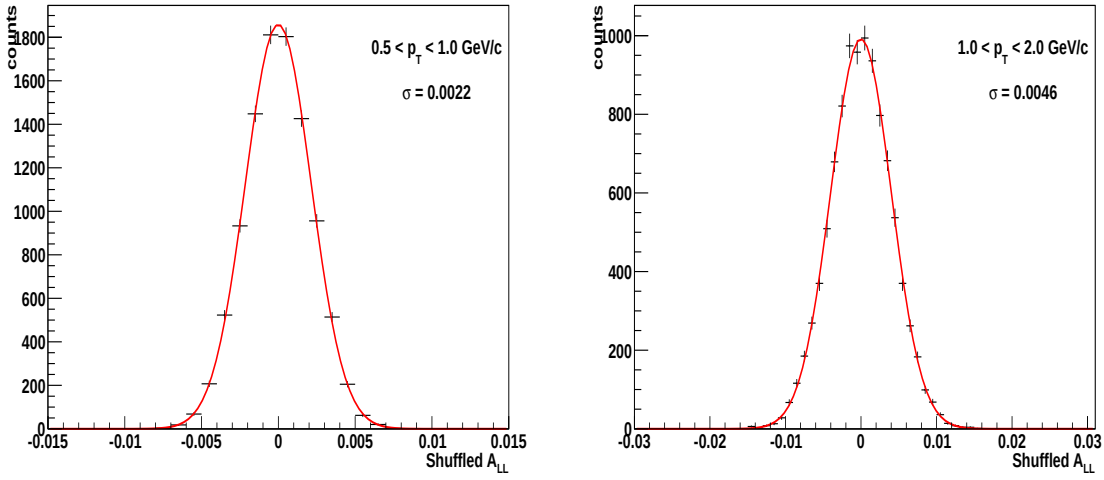

Figure 6.4: Distribution of bunch shuffled asymmetries for positive hadrons in the four p_T bins. The rms widths are, respectively,

CHAPTER 7

DISCUSSION OF ASYMMETRY RESULTS

The measured double helicity asymmetries for inclusive charged hadron production at mid-rapidity in polarized $p+p$ collisions at $\sqrt{s} = 62.4$ GeV are presented as a function of transverse momentum p_T in Fig. 7.1 (positive) and Fig. 7.2 (negative). The asymmetries (Table. 6.2) are compared to NLO pQCD predictions [94] based on several different parameterizations of polarized PDFs at scale $\mu = p_T$.

In the figures the curves labelled "DSSV" refer to deFlorian-Sassot-Stratmann-Vogelsang (DSSV) parameterizations of the helicity PDFs [59]. Similarly "GRSV" refer to Glück-Reya-Stratmann-Vogelsang parameterizations of helicity PDFs [70] and "BB" refer to Blümlein-Böttcher (BB) parameterizations of the helicity PDFs [47]. DSS fragmentation functions [58] were used for all the calculations. For the calculation of GRSV and BB curves coordinated-theoretical-experimental-project-on-QCD-6 [86] unpolarized PDFs were used and MRST2002 [81] unpolarized PDFs were used for the calculation of DSSV curves. The choice of a different set of unpolarized PDFs was inspired by the fact that the DSSV polarized PDF sets are based on it and variation of the calculated quantities due to choice of different unpolarized PDFs were found to be within current uncertainties.

Polarized DIS data [70, 47, 59] are used to extract parameters of the functional forms of the PDFs. Figures 7.1 and 7.2 show two instances of GRSV parameterizations based on the input $\Delta G(x, Q^2)$ value at an initial scale of $Q^2 = 0.4$ GeV^2 : (1) 'Standard' scenario with the best fit value $\Delta G = 0.24$ and (2) 'maximally saturated' scenario with $\Delta G(x) = G(x)$. DSSV [59] parameterizations use RHIC data along

with the available pDIS data to constrain parameters of the functional forms of the polarized PDFs. The asymmetries are also compared to the NLL estimations with the DSSV PDFs [63].

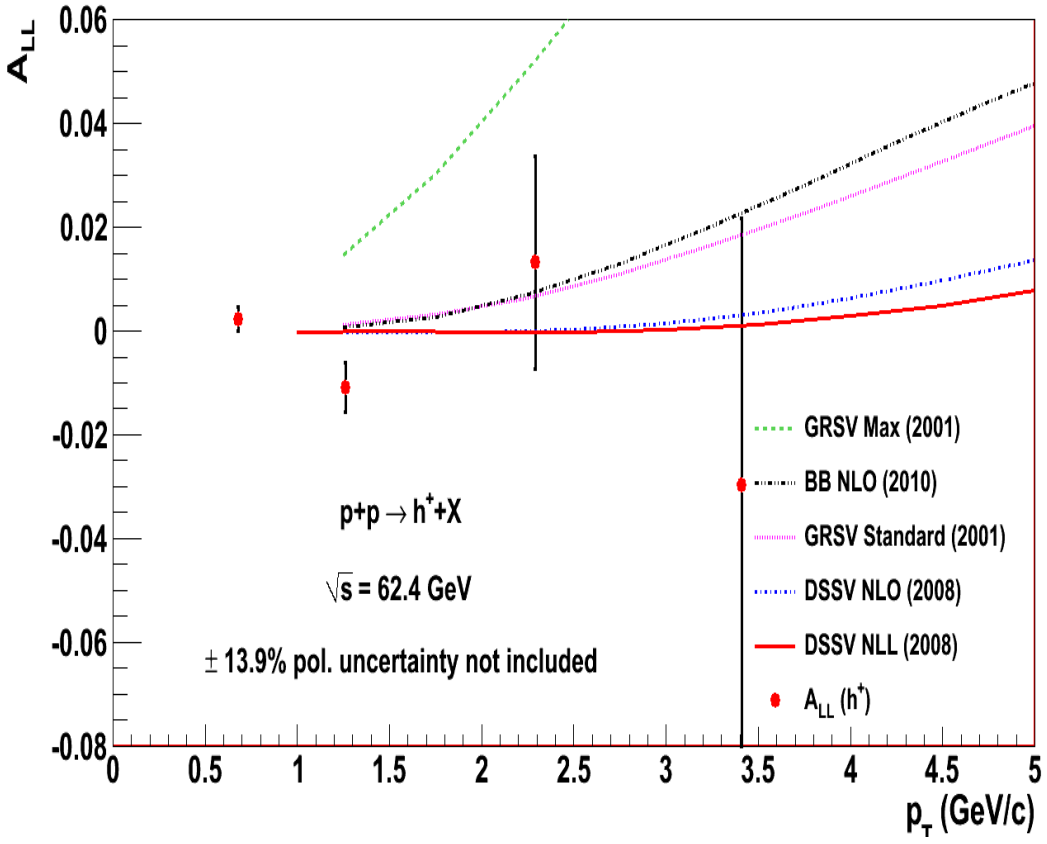

Figure 7.1: A_{LL} of mid-rapidity inclusive positive hadron production in proton-proton collisions at $\sqrt{s} = 62.4$ GeV with next-to-leading order calculations.

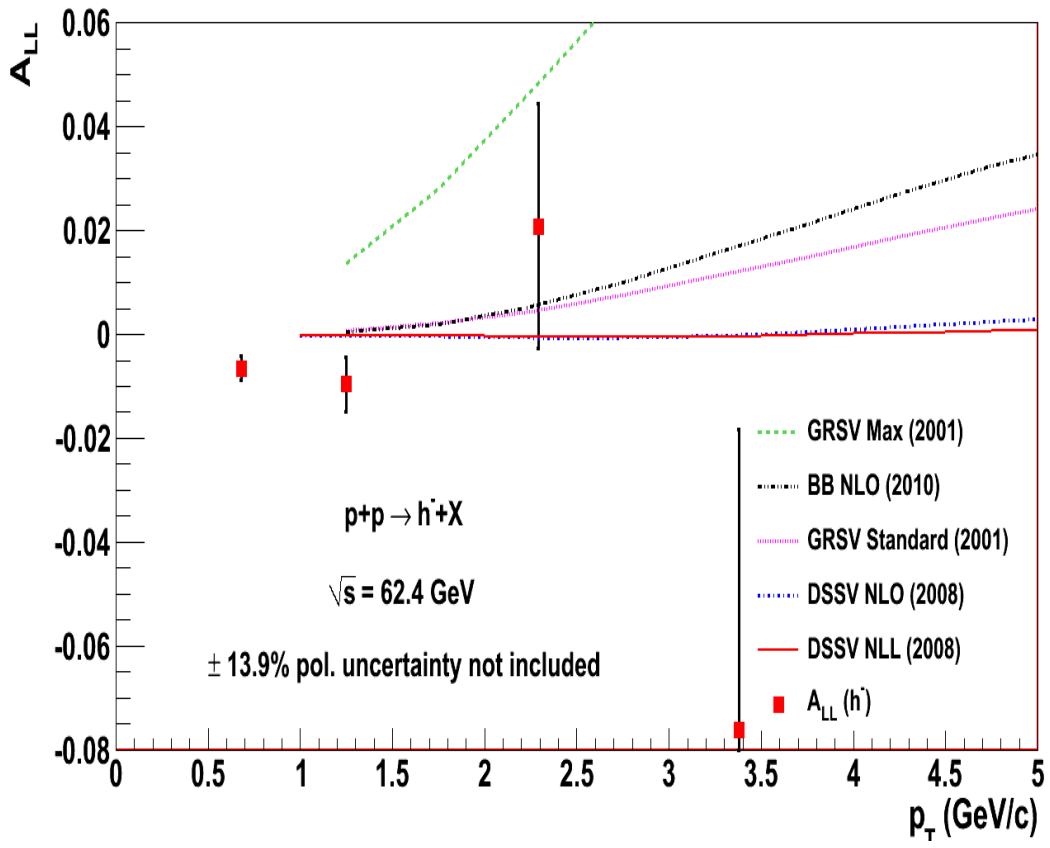

Figure 7.2: A_{LL} of mid-rapidity inclusive negative hadron production in proton-proton collisions at $\sqrt{s} = 62.4$ GeV with next-to-leading order calculations.

For the purpose of comparison with the experimental results, pQCD calculations were obtained for separate hadron species (pions, kaons and (anti)protons). Since our detector does not have uniform efficiency for all species, the species-separated calculations were combined using the particle fraction in the hadron mixture (Figures 3.5, 3.6) and corresponding detector efficiency (Fig. 4.15 and Fig. 4.16). The measured asymmetries are small and consistent with zero and they probe a range of approximately $0.05 \leq x_{gluon} \leq 0.2$ [62] of the interacting gluons. Since our double helicity measurements are mostly sensitive to the gluon polarization in leading order these results indicate that within the probed x-range, gluon helicity distribution $\Delta g(x)$ is small. The results are also consistent with the predictions from the several

of the recent parameterizations within statistical limitations. The analysis was based on comparatively small data set (7 days worth of data at RHIC) and therefore has fairly large statistical limitations. Even with limited statistics there results clearly corroborate previous PHENIX measurements [15, 14] that disfavor very large gluon polarization such as GRSV(max) from 2001. Double helicity asymmetry results presented here can be used to further constrain $\Delta g(x)$ distribution in the probed x-range. It's important to state that the measurements with different center-of-mass energies and over a variety of p_T range is required to probe gluon helicity distribution $\Delta g(x)$ over a wide range of x. Especially data from high $\sqrt{s}$ collisions can probe $\Delta g(x)$ at lower x values which is essential in understanding the gluon spin contribution to the spin of the proton as the parameterizations are poorly constrained resulting in large uncertainties in this x region.

The charged hadron asymmetries can also be useful in determining the sign of ΔG. Polarized up quark distribution is large and positive whereas polarized down-quark distribution is negative and smaller numerically. Combined with the fact that up quarks preferentially fragment into positive pions and down quarks preferentially fragment into negative pions, polarized pp collisions can generate $A_{LL}^{\Pi^+} \geq A_{LL}^{\Pi^0} \geq A_{LL}^{\Pi^-}$ for a positive ΔG and an opposite order for negative ΔG. Since charged pions are the largest contributor in the measured charged hadron composition and quark-gluon scattering are the dominant partonic subprocess in the production of most of the final state particle p_T range we measured, present measurements are sensitive to similar ordering.

CHAPTER 8

CONCLUSIONS AND OUTLOOK

8.0.12 Cross Sections and pQCD

Cross sections at high energy help us to test our understanding of pQCD. Measurements of neutral pion cross sections at PHENIX at various collision energies ($62.4, 200, 500$ GeV) and the comparisons of the results (shown in Fig. 8.1) to the pQCD calculations have demonstrated that next-to-leading order pQCD provides a very good description of the physics process. As mentioned in the Sect. 1.5, the fixed-target experiments with $\sqrt{s}$ of tens of GeV indicated that NLO pQCD is inadequate in the description of the data. Cross section of charged hadrons discussed in this thesis along with the π^0 cross section measurements at PHENIX at the energy of $\sqrt{s} = 62.4$ GeV have indicated that resummation of next-to-leading logarithmic terms may be relevant in describing the data at this energy. These measurements are important contributions towards testing the validity of such techniques and determination of the range of applicability.

8.0.13 Longitudinal Spin Program

The understanding of nucleon helicity structure thus fas have mostly been limited by the availability of high energy data from polarized scattering experiments. Polarization distributions of quarks and gluons as a function of the momentum fraction are poorly known at both high and very low momentum fraction and the range of Q^2 explored is much narrower than the unpolarized case since the polarized DIS experiments have been mostly fixed-target. However, the polarized lepton-hadron

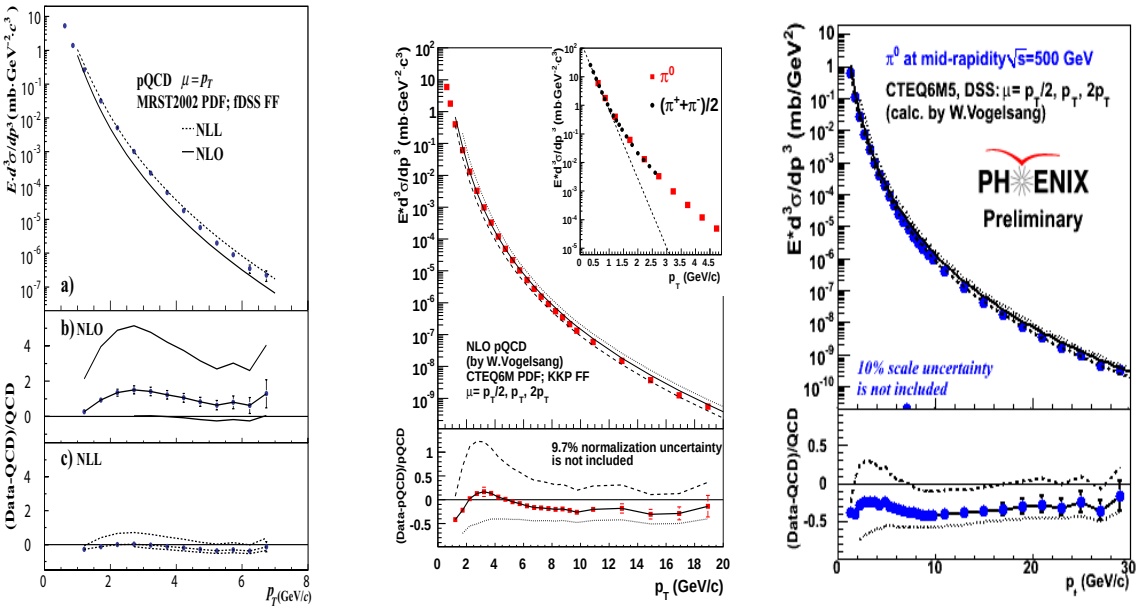

(a) 62.4 GeV (b) 200 GeV (c) 500 GeV

Figure 8.1: Cross sections of mid-rapidity π^0 production in proton-proton collisions (a) at $\sqrt{s} = 62.4$ GeV [15], (b) at $\sqrt{s} = 200$ GeV [13] and (c) at $\sqrt{s} = 500$ GeV (PHENIX preliminary) are compared to next-to-leading order pQCD calculations.

scattering experiments have made it clear that the spins of quarks and anti-quarks contribute only about $25 - 30\%$ to the nucleon spin. The gluons that carry about 50% of the total momentum distribution of the nucleon, might have been expected to carry a significant part of the nucleon spin as well, but the knowledge of the gluon spin distribution have been poor as it can be probed only via scaling violations in inclusive polarized DIS over limited range of Q^2. The spin program at PHENIX and STAR experiments provided direct access to gluon distributions inside polarized protons through the polarized $p + p$ collisions. The results have since constrained the polarized gluon distribution to be small in the probed x range and showed that it is smaller than various predictions (of $\Delta G \sim 1.0$ or larger) in the 1990s (Fig. 8.2).

PHENIX experiment has recorded 25 pb^{-1} of longitudinally polarized $p+p$ data at $\sqrt{s} = 200$ GeV over 2005,2006 and 2009 runs at RHIC. The double helicity asymmetry of neutral pions (Fig. 8.3) have been the flagship measurement for PHENIX over the

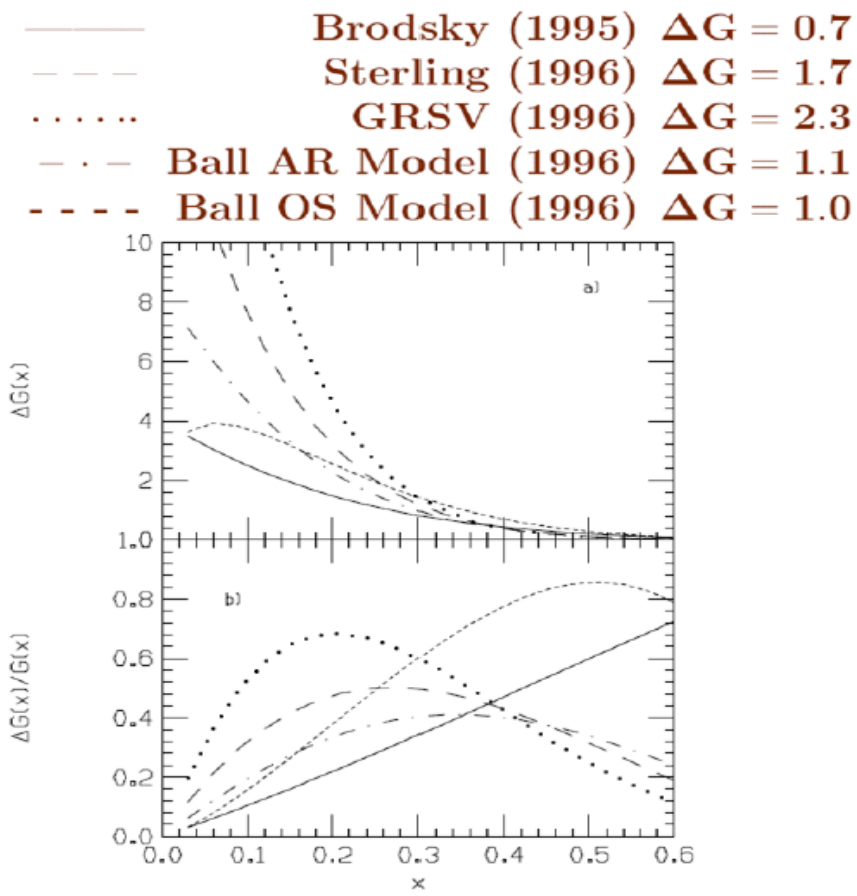

Figure 8.2: Several predictions for ΔG in the pre-RHIC period![1].

years in order to probe $\delta g(x)$ as a result of the abundance of neutral pions and the ability of PHENIX experiment to use high-energy triggers for the events where pi^0 decay into two photons. Double helicity asymmetry of π^0 production at a lower collision energy ($\sqrt{s} = 62.4$ GeV) was measured from 2006 data (Fig. 8.4a).

With increasing luminosity over the years, other probes at PHENIX became viable. Double helicity asymmetry measurements of η (Fig. 8.5a), direct photon (Fig. 8.5b) and charged pions (Fig. 8.4b) are shown below. Charged pions, although as abundant as the neutral pions, are statistically limited due to the lack of a suitable trigger. As mentioned before in Sect. 1.5, the charged pion asymmetries are particularly interesting as the ordering of the asymmetries of the three pion species is

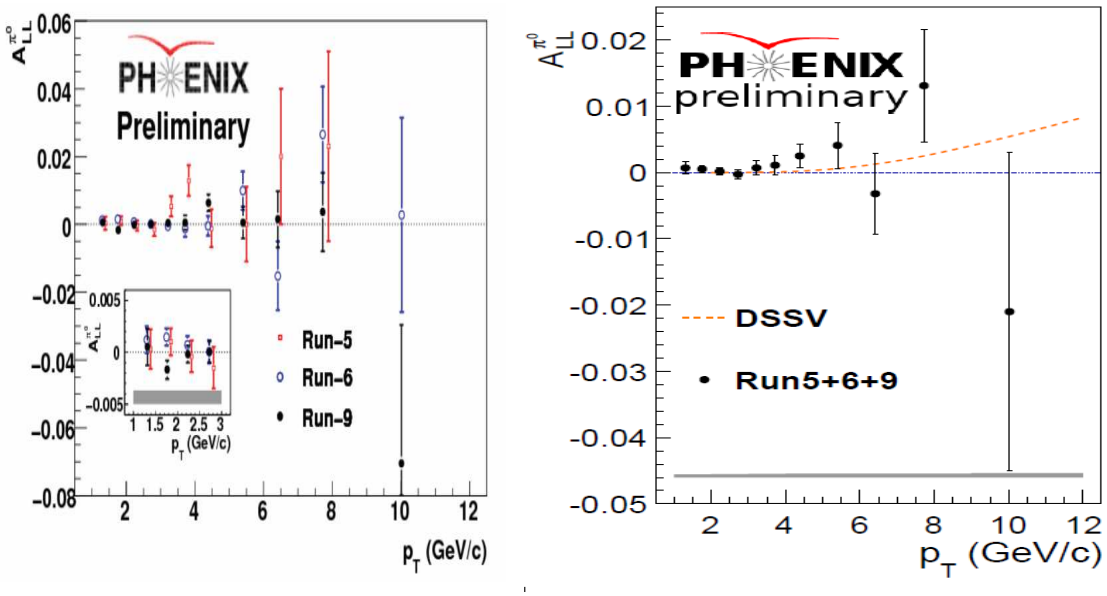

(a) separate years

(b) combined

Figure 8.3: Neutral pion double helicity asymmetry measurements from $p+p$ at $\sqrt{s} = 200$ GeV at PHENIX over the years (a) shown separately [1] and (b) combined (PHENIX preliminary) [1] and compared to calculated asymmetries using DSSV polarized PDFs.

sensitive to the sign of the ΔG. Direct photon is considered as a clean channel as the fragmentation is not involved in the process. Eta asymmetry measurement was made possible using the recent parameterization of η fragmentation with η cross sections measured at PHENIX along with world e^+e^- data.

Several different groups of physicists have worked with the existing experimental data and performed the 'global analysis' to extract $\Delta g(x)$. The methods and accuracies have improved with time as more and more measurements from different channels and/or probing different Bjorken x-ranges have been made available. As an example, we show (Fig. 8.6) the NLO estimation of $\Delta g(x)$ in 2002 (Stoesslein) and DSSV [59] result in 2008 which includes RHIC data from both STAR and PHENIX experiments along with the available polarized DIS data. A quick look at the y-axis promptly tells the tale of the order of magnitude improvement in narrowing down the uncer-

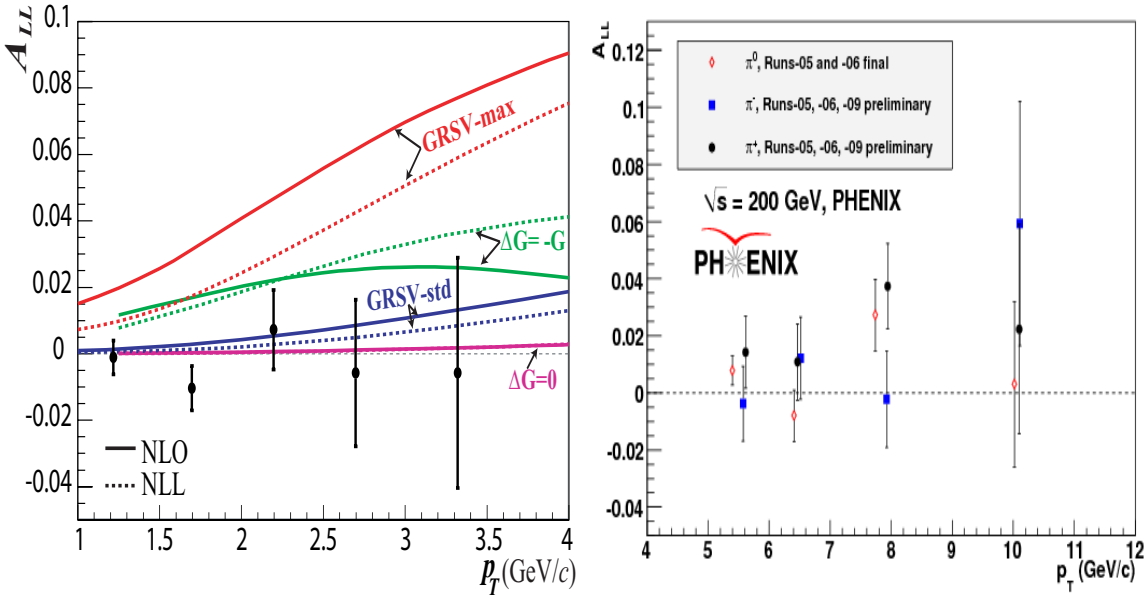

(a) π^0 (b) $\pi^{\pm}$

Figure 8.4: Double helicity asymmetry measurements from $p+p$ at PHENIX for (a) π^0 production at $\sqrt{s} = 62.4$ GeV [15] and (b) charged pion production at $\sqrt{s} = 200$ GeV (PHENIX preliminary) [1].

tainty on such estimations. RHIC data have helped constrain the polarized gluon distribution $\delta g(x)$ in the range $0.02 \leq x \leq 0.3$ and estimated ΔG to be small [59]. However, the uncertainties of the distribution beyond the range is still quite large. Data from recent years at higher energy of $\sqrt{s} = 500$ GeV at PHENIX will help to probe lower x-range and put constraints on $\delta g(x)$. On the other side of the picture, asymmetry measurements at the lower energy of 62.4 GeV e.g. charged hadron double helicity asymmetry discussed in this thesis, will be useful in constraining the $\delta g(x)$ distribution in the higher end of x.

At the highest $p+p$ collisions energy of $\sqrt{s} = 500$ GeV at RHIC, measurements of cross section and single spin asymmetry of W boson production in the central arms have been performed. Due to the nature of the weak force, particular charge of the W boson (mediator of weak force) corresponds to a particular helicity state only.

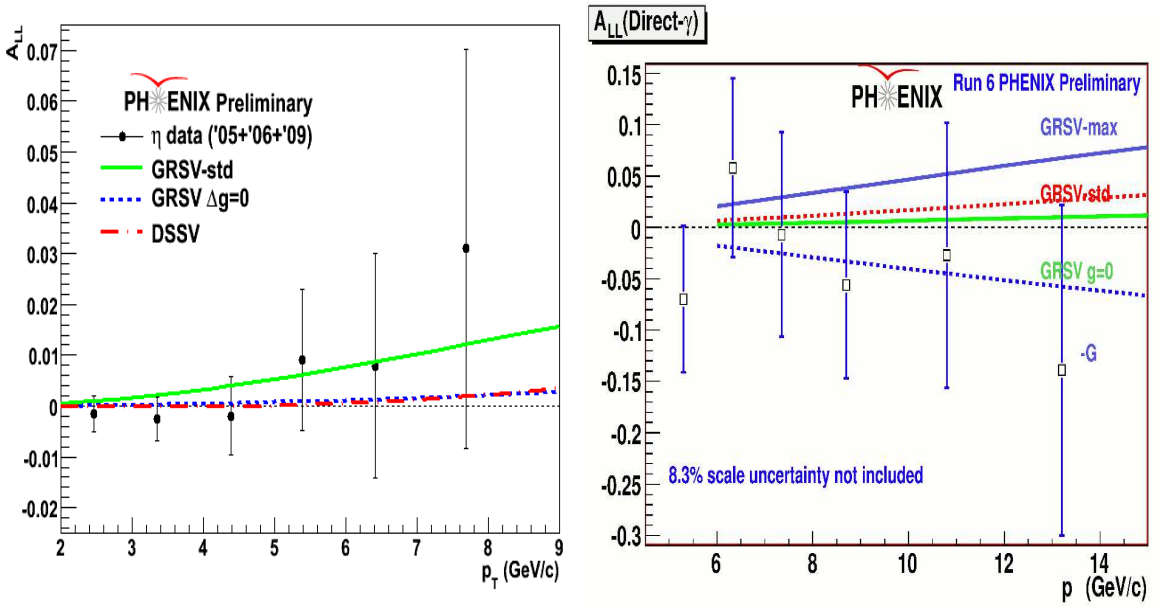

(a) η (b) Direct γ

Figure 8.5: Double helicity asymmetry measurements from $p+p$ at $\sqrt{s} = 200$ GeV at PHENIX for (a) η production [17] and (b) direct photon production (PHENIX preliminary) [1].

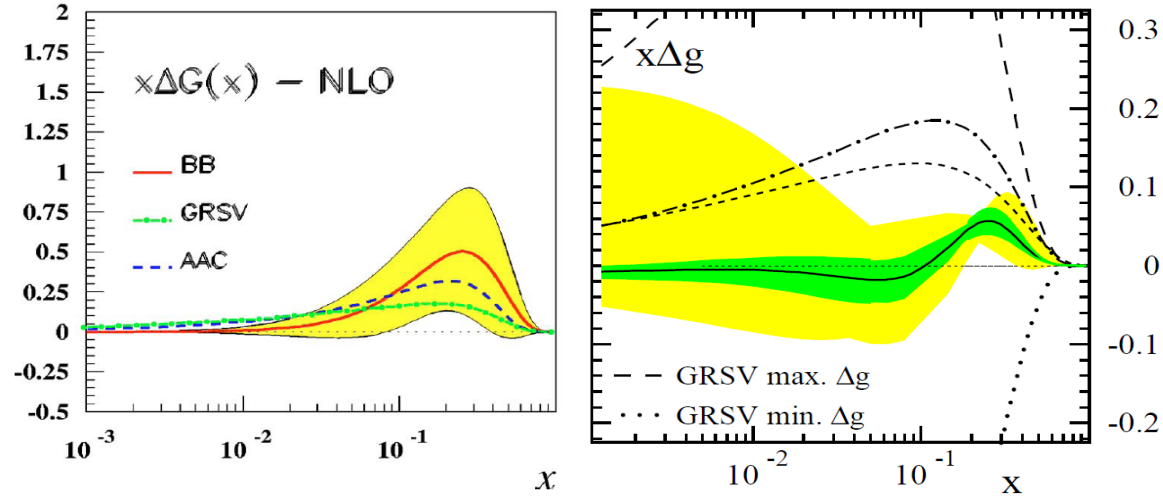

(a) (b)

Figure 8.6: Next-to-leading order estimation of $\Delta g(x)$ at $Q^2 = 4\text{GeV}^2$ in (a) 2002 [**?**] and at $Q^2 = 10\text{GeV}^2$ in (b) 2008 [59].

This provides a means for probing helicity distributions of flavor separated quarks and anti-quarks (besides semi-inclusive DIS measurements).

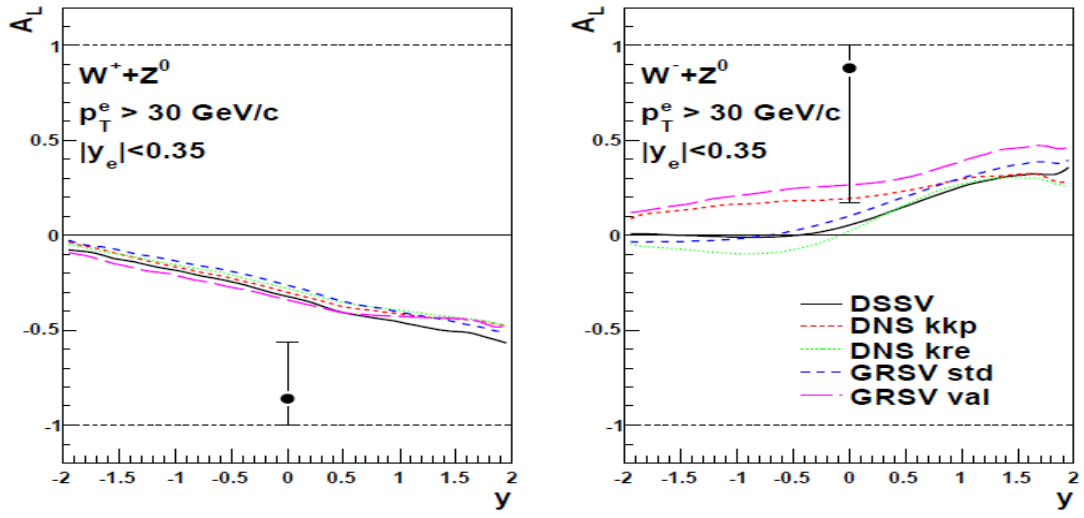

Figure 8.7: Single helicity asymmetry A_L of W boson for two different charges [18].

Given the indications (from global analyses using the latest experimental data) that gluon might carry a small fraction of the spin of the proton, the remaining portion must be carried by the orbital angular momentum of the quarks (and antiquarks) and the gluons. However, the spin decomposition of the proton is not uniquely defined. One such decomposition scheme, in the infinite momentum frame of the proton, is given by Jaffe and Manohar [73] and there ΔG is a gauge-invariant quantity and is interpreted as the contribution to the spin of the proton from the gluon spin. In the rest frame of the proton, a different version of the spin sum rule is given by Ji[74]. In this interpretation, only total angular momentum of the gluons is a gauge-invariant quantity, but this quantity cannot be further split in a gauge-invariant way to interpret gluon spin and orbital angular momentum separately. Other methods of decomposition nucleon spin have been proposed by Chen *et al.* [52] and recent works have tried to reconcile ([96], [78]) different approaches. It is hoped that with the difficulties in the definitions resolved, it might be possible to probe orbital angular

momentum of quarks and/or gluons to further the understanding of the nucleon helicity structure.

8.0.14 Transverse Spin Program

Since early observations of left-right asymmetry A_N in high-energy proton scattering [76], it was indicated that transverse effects play an important role in such scattering experiments. Measurements since then in various other experiments ([9, 8, 36]) have found similar results spurring the interest in the field as all the forward asymmetries were quite large in contrast to the early expectations based on pQCD. One possible origin of such large asymmetries could be the transversity distribution describing the correlation of transversely polarized quarks within a transversely polarized proton analogous to helicity PDF of quarks in longitudinally polarized protons. This however, is different in a couple of aspects. Firstly, gluons do not have transversity distributions and secondly, it can cannot be probed in QCD processes which are chiral-even.

The large transverse spin effects observed in semi-inclusive DIS and hadronic collisions have initiated the studies of transverse-momentum-dependent distributions (TMDs) which are functions of momentum fraction x and Q^2 as well as parton transverse momentum k_T. The Sivers function [91] is a TMD distribution that describes the correlation between the intrinsic transverse momentum of the partons within a transversely polarized nucleon and the direction of the nucleon spin and it can produce large transverse single spin asymmetries. Measurement of transverse single-spin asymmetry at PHENIX [26] have been used to put constraints on the gluon sivers function [80]. Recent measurements at PHENIX [16] of transverse single spin asymmetry of J/ψ production suggests nonzero tri-gluon correlation functions in transversely polarized protons. In future, single spin asymmetries of charmonium and

open heavy flavor production at PHENIX may play important role in understanding gluon dynamics in the nucleon.

There are also two fragmentation functions that are sensitive to the transversity, (a) interference fragmentation function [75], which is the collinear FF of two hadrons from the same scattered parton and (b) the Collins FF [56], which is the correlation between the transverse spin of a fragmenting quark and its transverse momentum. Collins FF is therefore transverse-momentum-dependent rather than collinear.

BIBLIOGRAPHY

[1] http://www.phenix.bnl.gov/phenix/WWW/docs/decadal/2010/phenix_decadal10_full_refs.pdf.

[2] http://www4.rcf.bnl.gov/~cnipol/pubdocs/Run06Offline/NOTE_2006_Polarizations_RHIC.txt.

[3] Aaron, F.D., et al. Combined Measurement and QCD Analysis of the Inclusive e+- p Scattering Cross Sections at HERA. *JHEP 1001* (2010), 109.

[4] Abe, K., et al. Precision determination of the neutron spin structure fuction g_1^n. *Phys. Rev. Lett.* (July 1997), 26–30.

[5] Abe, K., et al. Measurements of the proton and deuteron spin structure functions g_1 and g_2. *Phys. Rev. D* (October 1998).

[6] Abelev, B. I., et al. Longitudinal double-spin asymmetry and cross section for inclusive jet production in polarized proton collisions at $\sqrt{s} = 200$ gev. *Phys. Rev. Lett. 97* (2006).

[7] Abelev, B. I., et al. Longitudinal double-spin asymmetry and cross section for inclusive neutral pion production in polarized proton collisions at $\sqrt{s} = 200$ gev. *Phys. Rev. D 80* (2009).

[8] Adams, D. L., et al. Analyzing power in inclusive pi+ and pi- production at high x(f) with a 200-gev polarized proton beam. *Phys. Lett. B264* (1991), 462–466.

[9] Adams, D. L., et al. Comparison of spin asymmetries and cross-sections in pi0 production by 200-gev polarized anti-protons and protons. *Phys. Lett. B261* (1991), 201–206.

[10] Adams, J., et al. Cross sections and transverse single-spin asymmetries in forward neutral-pion production from proton collisions at $\sqrt{s} = 200$ gev. *Phys. Rev. Lett. 92* (2004).

[11] Adare, A., et al. High-p_T charged hadron suppression in Au + Au collisions at $\sqrt{s_{NN}} = 200$ GeV. *Phys. Rev. C 69* (2004), 034910.

[12] Adare, A., et al. Measurement of high-p_T single electrons from heavy-flavor decays in $p + p$ collisions at $\sqrt{s} = 200$ GeV. *Phys. Rev. Lett. 97* (Dec 2006), 252002.

[13] Adare, A., et al. Inclusive cross section and double helicity asymmetry for π^0 production in $p+p$ collisions at $\sqrt{(s)} = 200$ gev: Implications for the polarized gluon distribution in the proton. *Phys. Rev. D. 76* (2007), 051106(R).

[14] Adare, A., et al. Gluon-spin contribution to the proton spin from the double-helicity asymmetry in inclusive π^0 production in polarized $p+p$ collisions at $\sqrt{s_{NN}} = 200$ gev. *Phys. Rev. Lett. 103* (2009), 082002.

[15] Adare, A., et al. Inclusive cross section and double helicity asymmetry for π^0 production in $p+p$ collisions at $\sqrt{s} = 62.4$ gev. *Phys. Rev. D 79* (2009), 012003.

[16] Adare, A., et al. Measurement of transverse single-spin asymmetries for j/ψ production in polarized $p+p$ collisions at $\sqrt{s} = 200$ GeV. *Phys. Rev. D 82* (Dec 2010), 112008.

[17] Adare, A., et al. Cross section and double helicity asymmetry for η mesons and their comparison to π^0 production in $p+p$ collisions at $\sqrt{s} = 200$ GeV. *Phys. Rev. D 83* (2011), 032001.

[18] Adare, A., et al. Cross section and parity-violating spin asymmetries of $W^{\pm}$ boson production in polarized $p+p$ collisions at $\sqrt{s} = 500$ GeV. *Phys. Rev. Lett. 106* (Feb 2011), 062001.

[19] Adare, A., et al. Event structure and double helicity asymmetry in jet production from polarized $p+p$ collisions at $\sqrt{s} = 200$ GeV. *Phys. Rev. D 84* (Jul 2011), 012006.

[20] Adare, A., et al. Identified charged hadron spectra in $p+p$ collisions at $\sqrt{s}$=200 and 62.4 gev. *Phys. Rev. C 83* (2011), 064903.

[21] Adcox, K., et al. Phenix central arm tracking detectors. *Nucl. Instr. and Meth. A 499* (March 2003), 489–507.

[22] Adcox, K., et al. Phenix detector overview. *Nucl. Instr. and Meth. A 499* (March 2003), 469–479.

[23] Adler, S., et al. High-p_T charged hadron suppression in Au + Au collisions at $\sqrt{s_{NN}} = 200$ GeV. *Phys. Rev. C 69* (Mar 2004), 034910.

[24] Adler, S. S., et al. Absence of suppression in particle production at large transverse momentum in $\sqrt{s} = 200$ gev $d + au$ collisions. *Phys. Rev. Lett. 91* (2003), 072303.

[25] Adler, S. S., et al. Measurement of transverse single-spin asymmetries for midrapidity production of neutral pions and charged hadrons in polarized $p+p$ collisions at $\sqrt{s} = 200$ gev. *Phys. Rev. Lett. 95* (2005).

[26] Adler, S. S., et al. Measurement of transverse single-spin asymmetries for midrapidity production of neutral pions and charged hadrons in polarized $p+p$ collisions at $\sqrt{s} = 200$ GeV. *Phys. Rev. Lett. 95* (Nov 2005), 202001.

[27] Adler, S. S., et al. Measurement of direct photon production in p+p collisions at $\sqrt{s} = 200$ gev. *Phys. Rev. Lett. 98* (2007), 012002.

[28] Adler, S. S., et al. Modifications to di-jet hadron pair correlations in $au + au$ collisions at $\sqrt{(}s_{NN}) = 200$ gev. *Phys. Rev. Lett. 97* (2007), 052301.

[29] Adler, S. S., et al. Centrality dependence of charged hadron in deuteron+gold and nucleon+gold collisions at $\sqrt{s_{NN}}$=200 gev. *Phys. Rev. C 77* (2008), 014905.

[30] Aidala, Christine A., Ellinghaus, Frank, Sassot, Rodolfo, Seele, Joseph P., and Stratmann, Marco. Global analysis of fragmentation functions for eta mesons. *Phys. Rev. D 83* (2011), 034002.

[31] Aidala, Christine Angela. *Meaurement of the Transverse Single-Spin Asymmetry for Mid-rapidity Production of Neutral Pions in Polarized p+p Collisions at 200 GeV Center-of-Mass Energy.* PhD thesis, Columbia University, 2006.

[32] Airapetian, A., et al. Precise determination of the spin structure function g_1 of the proton, deuteron and neutron. *Phys. Rev. D 75* (2007), 012007.

[33] Aizawa, M., et al. Phenix central arm particle id detectors. *Nucl. Instr. and Meth. A 499* (2003), 508–520.

[34] Alekseev, I., et al. Polarized proton collider at rhic. *Nucl. Instrum. Methods A 499* (2003), 392–414.

[35] Alekseev, I. G., et al. Analyzing power in CNI-region at AGS (experiment E950). *AIP Conf. Proc. 549* (2000), 670–673.

[36] Alekseev, M., et al. Measurement of the collins and sivers asymmetries on transversely polarised protons. *Phys. Lett. B692* (2010), 240–246.

[37] Alguard, M. J., et al. Deep inelastic scattering of polarized electrons by polarized protons. *Phys. Rev. Lett. 37* (Nov 1976), 1261–1265.

[38] Allen, M., et al. Phenix inner detectors. *Nucl. Instr. and Meth. A 499* (2003), 549–559.

[39] Almeida, Leandro G., Sterman, George F., and Vogelsang, Werner. Threshold resummation for di-hadron production in hadronic collisions. *Phys. Rev. D 80* (2009), 074016.

[40] Alper, B., et al. The production of charged particles with high transverse momentum in proton-proton collisions at the cern isr. *Nucl. Phys. B 87* (1975).

[41] Altarelli, Guido, and Parisi, G. Asymptotic Freedom in Parton Language. *Nucl. Phys. B126* (1977), 298.

[42] Aphecetche, L., et al. Phenix calorimeter. *Nucl. Instr. and Meth. A 499* (2003), 521–536.

[43] Aronson, S.H., et al. *Nucl. Instrum. Methods A 499* (2003), 480.

[44] Ashman, J., et al. A measurement of the spin asymmetry and determination of the structure function g1 in deep inelastic muon-proton scattering. *Phys. Lett. B* (May 1988), 364–370.

[45] Bass, Steven D. The spin structure of the proton. *Rev. Mod. Phys. 77* (November 2005), 1257.

[46] Baum, G., et al. New measurement of deep-inelastic $e - p$ asymmetries. *Phys. Rev. Lett. 51* (Sep 1983), 1135–1138.

[47] Blümlein, Johannes, and Böttcher, Helmut. Qcd analysis of polarized deep inelastic scattering data. *Nucl. Phys. B 841* (2010), 205–230.

[48] Boyle, Kieran Peter. *Measurements of the Double Helicity Asymmetry in Pion Production in Proton Collisions at* $\sqrt{s}$ *= 200 GeV and the Resulting Constraints on the Polarized Gluon Distribution in the Proton.* PhD thesis, Stony Brook University, 2008.

[49] Breidenbach, M., Friedman, J. I., Kendall, H. W., Bloom, E. D., Coward, D. H., DeStaebler, H., Drees, J., Mo, L. W., and Taylor, R. E. Observed behavior of highly inelastic electron-proton scattering. *Phys. Rev. Lett. 23* (Oct 1969), 935–939.

[50] Bunce, G., Saito, N., Soffer, J., and Vogelsang, W. *Ann. Rev. Nucl. Part. Sci. 50* (2000), 525–575.

[51] CERN Program Library. *GEANT 3.2.1*, 1993. http://wwwasdoc.web.cern.ch/wwwasdoc/pdfdir/geant.pdf.

[52] Chen, Xiang-Song, Lü, Xiao-Fu, Sun, Wei-Min, Wang, Fan, and Goldman, T. Spin and orbital angular momentum in gauge theories: Nucleon spin structure and multipole radiation revisited. *Phys. Rev. Lett. 100* (2008), 232002.

[53] Chodos, A., Jaffe, R. L., JOhnson, K., and Thorn, C. B. Baryon structure in the bag theory. *Phys. Rev. D 9* (1974).

[54] Christy, E. M., et al. Measurements of electron-proton elastic cross sections for $0.4 < Q^2 < 5.5$ $(\mathrm{GeV}c)^2$. *Phys. Rev. C 70* (Jul 2004), 015206.

[55] Collins, J. C., Soper, D. E., and Sterman, G. Soft gluons and factorization. *Nucl. Phys. B 308* (1988), 833.

[56] Collins, John C. Leading twist single transverse-spin asymmetries: Drell-yan and deep inelastic scattering. *Phys. Lett. B536* (2002), 43–48.

[57] de Florian, D., Sassot, Rodolfo, and Stratmann, Marco. Global analysis of fragmentation functions for pions and charged hadrons. *Phyis. Rev. D 76* (2007).

[58] de Florian, D., Sassot, Rodolfo, and Stratmann, Marco. Global analysis of fragmentation functions for pions and kaons and their uncertainties. *Phys. Rev. D 75* (2009), 114010.

[59] de Florian, D., Sassot, Rodolfo, Stratmann, Marco, and Vogelsang, W. Global analysis of helicity parton densities and their uncertainties. *Phys. Rev. Lett. 101* (2008), 072001.

[60] de Florian, D., Sassot, Rodolfo, Stratmann, Marco, and Vogelsang, W. Extraction of spin-dependent parton densities and their uncertainties. *Phys. Rev. D 80* (2009), 034030.

[61] de Florian, D., and Vogelsang, W. Threshold resummation for the inclusive-hadron cross section in *pp* collisions. *Phys. Rev. D. 71* (2005), 114004.

[62] de Florian, D., Vogelsang, W., and Wagner, F. Single-inclusive hadron production in polarized *pp* scattering at next-to-leading logarithmic accuracy. *Phys. Rev. D. 76* (2007), 094021.

[63] de Florian, D., and Wagner, F. private communication, 2010.

[64] Drijard, D., et al. NEUTRAL STRANGE PARTICLE PRODUCTION IN PROTON PROTON COLLISIONS AT $\sqrt{s} = 63$-GeV. *Zeit. Phys. C12* (1982), 217.

[65] Ellis, John, and Jaffe, Robert. Sum rule for deep-inelastic electroproduction from polarized protons. *Phys. Rev. D 9*, 5 (1974), 1444–1446.

[66] Ellis, R. K., Georgi, H., Machacek, M., Politzer, H. D., and Ross, G. G. Factorization and the parton model in qcd. *Phys. Lett. B 78* (1978), 281.

[67] Esterman, I., and Stern, O. Über die magnetische Ablenkung von Wasserstoffmolekülen und das magnetische Moment des Protons. II. *Zeitschrift fur Physik 85* (Jan. 1933), 17–24.

[68] Feynman, Richard P. Very high-energy collisions of hadrons. *Phys. Rev. Lett. 23* (1969), 1415–1417.

[69] Frisch, R., and Stern, O. Über die magnetische Ablenkung von Wasserstoffmolekülen und das magnetische Moment des Protons. I. *Zeitschrift fur Physik 85* (Jan. 1933), 4–16.

[70] Glück, M., Reya, E., Stratmann, M., and Vogelsang, W. Models for the polarized parton distributions of the nucleon. *Phys. Rev. D. 63* (2001), 094005.

[71] Graudenz, D., Hampel, M., Vogt, A., and Berger, Christoph. The Mellin transform technique for the extraction of the gluon density. *Z. Phys. C70* (1996), 77–82.

[72] Hughes, E. W., and Voss, R. Spin structure functions. *Annu. Rev. Nucl. Part. Sci.* (1999), 303–339.

[73] Jaffe, Robert L., and Manohar, Aneesh. The g_1 problem : Deep inelastic electron scattering of the proton. *Nucl. Phys. B 337* (1990), 509–546.

[74] Ji, Xiangdong. Lorentz symmetry and the internal structure of the nucleon. *Phys. Rev. D 58* (Jul 1998), 056003.

[75] John C. Collins, Steve F. Heppelmann, and Ladinsky, Glenn A. Measuring transversity densities in singly polarized hadron-hadron and lepton-hadron collisions. *Nucl. Phys. B420* (1994), 565–582.

[76] Klem, R., et al. Measurement of Asymmetries of Inclusive Pion Production in Proton Proton Interactions at 6 GeV/c and 11.8 GeV/c. *Phys. Rev. Lett.* (1976), 929–931.

[77] Kosower, David A. Extracting parton densities from collider data. *Nucl.Phys. B520* (1998), 263–278.

[78] Leader, Elliot. On the controversy concerning the definition of quark and gluon sangular momentum. *Phys. Rev. D 83* (2011), 096012.

[79] Leader, Elliot, Sidorov, Aleksander, and Stamenov, Dimiter. Determination of polarized parton densities from a QCD analysis of inclusive and semi-inclusive deep inelastic scattering data. *Phys. Rev. D 82* (2010), 114018.

[80] M. Anselmino, U. D'Alesio, S. Melis, and Murgia, F. Constraints on the gluon sivers distribution via transverse single spin asymmetries at mid-rapidity in $p^{\uparrow}p \to \pi^0 x$ processes at rhic. *Phys. Rev. D 74* (2006), 094011.

[81] Martin, A.D., Roberts, R.G., Stirling, W.J., and Thorne, R.S. Uncertainties of predictions from parton distributions. 1: Experimental errors. *Eur.Phys.J. C28* (2003), 455–473.

[82] Martin, A.D., Stirling, W.J., Thorne, R.S., and Watt, G. Parton distributions for the LHC. *Eur.Phys.J. C63* (2009), 189–285.

[83] McAllister, R. W., and Hofstadter, R. Elastic scattering of 188-mev electrons from the proton and the alpha particle. *Phys. Rev. 102* (May 1956), 851–856.

[84] Nakagawa, I., et al. Polarization measurements of rhic-pp run05 using cni pc-polarimeter. *AIP Conf. Proc. 915* (June 2007), 912–915.

[85] Okada, H., et al. Measurement of the analyzing power a_n in pp elastic scattering in the cni region with a polarized atomic hydrogen gas jet target. *Phys. Lett. B 638* (2006), 450.

[86] Pumplin, J., Stump, D.R., Huston, J., Lai, H.L., Nadolsky, Pavel M., et al. New generation of parton distributions with uncertainties from global QCD analysis. *JHEP 0207* (2002), 012.

[87] Punjabi, V., et al. Proton elastic form factor ratios to $Q^2 = 3.5$-GeV^2 by polarization transfer. *Phys. Rev. C71* (2005), 055202.

[88] Qattan, I. A., et al. Precision rosenbluth measurement of the proton elastic form factors. *Phys. Rev. Lett. 94* (2005), 142301.

[89] Rosenbluth, M. N. High energy elastic scattering of electrons on protons. *Phys. Rev. 79* (Aug 1950), 615–619.

[90] Roser, T. Acceleration of polarized beams using multiple strong partial snakes. *Proceedings of the 16th International Spin SPhysics Symposium (SPIN2004)* (2005), 687.

[91] Sivers, Dennis. Single-spin production asymmetries from the hard scattering of pointlike constituents. *Phys. Rev. D 41* (Jan 1990), 83–90.

[92] Stosslein, U. Status and perspectives of spin physics. *Acta Phys. Polon. B33* (2002), 2813–2834.

[93] Stratmann, Marco, and Vogelsang, Werner. Towards a global analysis of polarized parton distributions. *Phys.Rev. D64* (2001), 114007.

[94] Taneja, S. private communication, 2010.

[95] Vogelsang, W. private communication, 2008.

[96] Wakamatsu, M. Gauge and frame-independent decomposition of nucleon spin. *Phys.Rev. D 83* (2011), 014012.

[97] Walker, R. C., et al. Measurements of the proton elastic form factors for $1 < q^2 < 3$ gev^2 at slac. *Phys. Rev. D 49* (Jun 1994), 5671–5689.

[98] Zhan, X., Allada, K., Armstrong, D.S., Arrington, J., Bertozzi, W., et al. High Precision Measurement of the Proton Elastic Form Factor Ratio $\mu_p G_E/G_M$ at low Q^2. *Phys.Lett. B705* (2011), 59–64.